DEVICES: COMMERCIAL USE OF SPACE

Semi-Annual Report

to

ronautics and Space Administration
angley Research Center
ampton, VA 23665-5225

July 3, 1992 - March 31, 1993

Haertling

ne Furman

hiung Hsi
g Li

March 31, 199

Department of Ceramic
College of Engineering

SUPERCONDUCTIVITY DEVICES: COMMERCIAL USE OF SPACE

Semi-Annual Report

to

National Aeronautics and Space Administration
Langley Research Center
Hampton, VA 23665-5225

Period: July 3, 1992 - March 31, 1993

Principal Investigator:
Gene Haertling

Co-Investigator: Eugene Furman

Supporting Investigators:
Chi-Shiung Hsi
Guang Li

Contract No. NAG-1-1301

March 31, 1993

CLEMSON
UNIVERSITY

Department of Ceramic Engineering
College of Engineering

I. Introduction

The high Tc (>95K) superconducting ceramic materials, initially developed in 1987, are now being extensively investigated for a variety of engineering applications. These applications include such devices as conducting links, rotating and linear bearings, sensors, filters, switches, high Q cavities, magnets and motors. Some of these devices take advantage of the material's ability to lose all electrical resistance at a critical temperature (Tc) while others make use of the repulsion forces generated between the magnetic field of a permanent magnet and a superconductor which is cooled below its Tc; i.e., the Meissner effect.

A device involving the first of these effects; i.e., the loss of resistance at the onset of superconductivity, has been under development at Clemson University under the sponsorship of NASA Langley for the last three years. Known as a low thermal conductivity superconducting grounding link for the SAFIRE program, this device has undergone a full year of real time testing and has shown promise of meeting some of the design specifications.

A companion device to the grounding link in the SAFIRE application is the data link between the detectors and the preamps. In contrast to the former device which is a single conductor, the data link consists of a large number of electrically isolated leads of very small cross section which are designed to carry an electrical signal yet keep the thermal losses to a bare minimum. This application is obviously more demanding from a technical standpoint than the grounding link because the technologies involved in processing and fabricating small, multiple-leaded devices is considerably more complicated. Much of the work reported in this annual work involves (1) screen printing of both 2223 BSCCO and 123 YBCO materials on substrates, (2) evaluation of the resulting superconducting properties and (3) the use of these materials as possible electrode materials for ferroelectrics at 77K.

In addition to this device, work is also being carried out on the development of solid-state electromechanical actuators which can be used in a number of applications in space such as cryopump motors, anti-vibration active structures and telescope mirror correctors. Considering any of these applications, the key to the successful development of a device is the successful development of a ceramic material which can produce maximum displacement per volt input. This is especially true of the cryocooler pump application where size, efficiency and reliability are of prime consideration. This report describes the work accomplished toward this goal in the first 18 months; i.e., (1) a review of the present state of the art in actuator technology, (2) the fabrication and processing of high strain PBZT electrostrictive materials and (3) the testing and evaluation of these electrostrictive materials.

A new development effort has also been initiated in the actuator area. It consists of a new processing technology for preparing piezoelectric and electrostrictive ceramic materials. It involves a high temperature chemical reduction process which leads to an internal pre-stressing of the oxide wafer, thus the name **RAINBOW**, standing for **R**educed **A**nd **IN**ternally **B**iased **O**xide **W**afer. Ceramics fabricated by this method produce bending-mode actuator devices which possess a factor of ten more displacement and load bearing capacity than present-day benders (unimorphs, bimorphs). This report summarizes the results from initial studies of the RAINBOWS.

The report is divided into four parts with Part I dealing with the processing and screen printing of the superconducting BSCCO and 123 YBCO materials on substrates and PLZT ferroelectrics, Part II reporting on the electromechanical actuator compositional work, Part III dealing with the characterization of the RAINBOW devices and Part IV treating general subject areas of RAINBOWS.

Part I.

Semi-Annual Report

SUPERCONDUCTIVITY DEVICES: COMMERCIAL USE OF SPACE

Screen Printed Y and Bi-Based Superconductors and the YBCO and BSCCO Electrodes to Ferroelectric Materials

to

National Aeronautics and Space Administration

Langley Research Center

Hampton, VA 23656-5225

Principal Investigator:

Gene H. Haertling -Clemson University

Supporting Investigator:

Chi-Shiung Hsi -Clemson University

Contract No: NAG-1-1301

March, 1993

Abstract

A YBCO thick film containing 20% Ag_2O with a T_c of 86.8K and a J_c of 108A/cm^2 was obtained. The film was fabricated by a two-step firing process, i. e. firing the film at 1000°C for 10 minutes and annealing at 970°C for 30 minutes. The two-step firing process, however, was not suitable for the multiple-lead YBCO sample due to the formation of the 211 green phase at 1000°C in the multiple-lead YBCO sample. A BSCCO thick film printed on a MgO coated MSZ substrate and fired at 845°C for 2 hours exhibited a superconducting behavior at 89K. Because of its porous microstructure, the critical current density of the BSCCO thick film was limited.

This report also includes the results of the YBCO and BSCCO materials used as oxide electrodes for ferroelectric materials. The YBCO electroded PLZT showed higher remanent polarization and coercive field than the sample electroded with silver paste. A higher Curie temperature for the PLZT was obtained from the YBCO electroded sample. The BSCCO electroded sample, however, exhibited the same Curie temperature as that of a silver electroded sample. Dissipation factors of the ferroelectric samples increased when the oxide electrode was applied.

I. Introduction.

The results of two research subjects are included in this report; these are:

1. Screen Printed Y and Bi-Based Superconductors, and
2. A Novel Electroding Process for Ferroelectric Materials- YBCO and BSCCO Oxide Electrodes.

Those results are reported and discussed according to their subject.

II. Screen Printed Y and Bi-Based Superconductors.

II.1 Introduction.

In the previous report[1], $YBa_2Cu_3O_{7-x}$ superconductor thick films had been made on the YSZ substrates with T_c at 86.4K and J_c of 50A/cm^2. Improvement in the electrical properties of the YBCO thick films are reported here. The YBCO thick films were printed on MSZ (Magnesium Stabilized Zirconia) substrates in order to eliminate cracks in the films. The fabrication conditions of the multiple-lead YBCO thick films were investigated in accordance with to the results of the single film process.

$(Bi_{1.6}Pb_{0.4})Sr_{1.9}Ca_{2.05}Cu_{3.05}O_x$ superconductor thick films were printed on different kinds of substrates, i.e. YSZ, BSCCO coated YSZ, MSZ, and MgO coated MSZ. The BSCCO thick films were sintered in air and a low oxygen atmosphere (6% O_2) since a low oxygen atmosphere was found to be the best condition to maintain the BSCCO 2223 high temperature phase during sintering[2].

II.2 Experimental Procedure.

The YBCO superconductor powder was prepared by the conventional mixed oxides process[3]. The BSCCO superconductor powder was prepared by a chemical coprecipitation process. Lead, strontium, and calcium acetates were dissolved in acetic acid and water solution before they were mixed with bismuth and copper acetates. In order to dissolve the acetates, acetic acid and ammonium hydroxide were used to adjust the pH value of the mixed solution. The mixed solution became a clear blue solution after the acetates were completely dissolved. The coprecipitated powder was prepared by

pouring the acetate solution into an agitating oxalic acid solution. After coprecipitated, the slurry was dried in a vacuum dryer for 8 hours. A brown oxide powder was obtained after the dried oxalate powder was decomposed at 600°C for 4 hours. The oxide powder was calcined at 830°C for 24 hours and then calcined at 845°C for 30 hours for two additional times. After final calcination, the BSCCO superconductor powder was completed.

Superconductor pastes were prepared by mixing the YBCO and BSCCO superconductor powder with α-terpineol in a 6:1 ratio. In order to increase adhesion of the green film, 10 wt% of binder (Metoramic Science Inc., B73305) was added to the YBCO paste and 5 wt% of binder was added to the BSCCO paste.

In the previous report[1], YBCO thick films with 20 wt% Ag_2O printed on the 8% YSZ (Yttrium Stabilized Zirconia) substrates showed higher T_c and J_c values than the films printed on the 211 (Y_2BaCuO_5) and SNT ($Sr_{0.875}(Ti_{0.75}Nb_{0.25})O_3$) substrates. However, the cracks in the film limited the T_c and J_c value of the films. In the present work, MSZ (Magnesium Stabilized Zirconia) and 16% YSZ substrates ,which had higher thermal expansion coefficients than the 8% YSZ substrate, were used as substrate materials. In addition, a YBCO thick film with 30% Ag_2O was also prepared in order to increase the bounding between the YBCO grains.

Zirconia-based material, which has a lower thermal conductivity, are preferred in the SAFIRE application. The zirconia-based substrates with different amounts of Y_2O_3 or MgO additives were used as substrate materials in the process. The substrates were made by a tape casting method and fired at 1600°C for 5 hours. Since BSCCO thick films printed on MgO substrates show better electrical properties than when they are printed on the other kinds of substrates[8,9], some of the ZrO_2-based substrates used for the BSCCO thick films were coated with MgO. The dip coating process was used to coat the MgO on the ZrO_2 substrate. Magnesium acetate dissolved in methanol was used as the coating solution. After the MgO was deposited on the substrates, they were fired at

1550°C for 30 minutes. A BSCCO coated ZrO_2 substrate was also used as a substrate material. This kind of substrate was prepared by melting a thin layer of BSCCO film on the top of the ZrO_2 substrate at 890°C for 20 minutes.

The superconductor thick films were deposited on the substrates by printing the pastes through a 200 mesh stainless steel screen. Two kinds of patterns, single and multiple-lead, were printed on the substrates. The single sample size was 1 cm wide and 4 cm long. The multiple-lead sample had 15 lines. The size of each line was 20 mils width and 1500 mils long. The space between each lines was 20 mils.

The YBCO thick films were sintered at 960 to 990°C for 5 minutes to 1 hour, in an oxygen atmosphere. After sintering, the samples were cooled to room temperature at a 2° C/min rate. A two step firing process was also used to fire the YBCO thick film. The firing conditions of the two step firing process were 1000°C for 10 minutes and 970°C for 30 minutes. The BSCCO films were fired at temperature from 830° to 855°C for 10 minutes to 4 hours in air or 8% oxygen atmosphere. After the YBCO films were fired, electrodes (as determined in a previous contract No. NAG-1-820), were applied to the YBCO thick films. Silver electrodes were fired onto the BSCCO thick films at 845°C for 12 minutes.

Critical temperatures of the samples showing zero resistance, T_c, were measured by the four-point method. The J_cs of the films were measured at 1μV/cm level at 77K.

II.3 Results and Discussion.

II.3.1 YBCO thick films printed on zirconia-based substrates.

A YBCO thick film with 30 wt% Ag_2O was printed on 8% YSZ substrate and fired at 990°C for 10 minutes. The film had lower resistivity than the films with 10 or 20 wt% Ag_2O, at room temperature. During critical temperature measurement, the resistance of the film decreased with decreasing measuring temperature. The film showed

an onset behavior at 96K, as indicated by the curve a in Figure 1. However, the film was not in the superconducting state at liquid nitrogen temperature.

The YBCO thick film with 20 wt% Ag_2O printed on the MSZ substrate and fired at 980°C for 10 minutes had a lower resistivity than the film printed on the YSZ substrate. From the sample's x-ray diffraction result, partial preferred orientation in YBCO (001) direction was observed, as shown in Figure 2. A metallic behavior was observed during critical temperature measurement, as presented by the curve b in the Figure 1. The YBCO film on the MSZ substrate, however, was not in the superconducting state at liquid nitrogen temperature. There was no onset temperature observed from the T_c measurement of this sample.

When the YBCO thick film printed on the 16% YSZ substrate, a Y_2BaCuO_5 green phase was observed after the film was fired at 980°C for 30 minutes. A YBCO thick film printed on a 8% YSZ substrate and fired at the same conditions as the previous sample had a T_c at 84.4K. Serious interaction between the YBCO thick film and the 16% YSZ substrate occurred at 980°C. Increasing the Y_2O_3 content in the YSZ substrate resulted in an increased reaction rate between YBCO and YSZ substrate. Therefore, the MSZ and 16% YSZ substrate would not be appropriate substrate materials for the YBCO superconductor thick films.

II.3.2 Two steps firing process.

Figure 3 presents the T_c curve of a sample heat-treated by a two step firing process. The YBCO film was melted at 1000°C in the first step and, then, was annealed at 970°C for 30 minutes in the second step. The film crystallized and possessed partial preferred orientation during second step annealing, as shown in Figure 4. This film had a T_c of 86.8K at a 1mA measuring current. The J_c of the film was 108 A/cm^2, which was about two times the J_c value obtained by the single step firing. The increase in T_c and J_c might be caused by the elimination of cracks, since the resistivity of the film, at room temperature, was lower than the film made by the single step process.

II.3.3 YBCO multi-lead sample.

Multiple-lead YBCO thick films with 10 or 20wt% Ag_2O were printed on the 8% YSZ substrates. The multiple-lead films were sintered by a one- or two-step process. When the films were sintered by the two-step process, i. e. firing at 1000°C for 10 minutes and annealing at 970°C for 30 minutes, a 211 (Y_2BaCuO_5) green phase appeared on the film surface. The 211 green phase was still observed in the film, when the firing conditions were changed to 1000°C for 5 minutes and annealing at 960°C for 30 minutes. At firing temperatures higher than 990°C, the YBCO 211 green phase formed in the multiple-lead YBCO sample. The two-step firing process, which had a firing temperature at 1000°C in the first firing step, was not an appropriate fabrication process for the multiple-lead YBCO sample.

The YBCO 211 green phase was not observed in the multiple-lead thick films when the firing temperature was lower than 990°C. Figure 5 shows the T_c curve of a multiple-lead YBCO thick film printed on 8% YSZ substrate and fired at 985°C for 12 minutes. The film had a T_c of 86.3K at 20μA measuring current. When the measuring current increased to 50μA, the critical temperature of the sample decreased to 82.3K. Table 1 lists the critical temperatures of the YBCO multiple-lead thick films fired at different conditions. Relatively high critical temperature samples were obtained when the samples were fired at 980°C for 12 minutes. The highest J_c of the multiple-lead thick films were obtained from the films with 10wt% Ag_2O and fired at 980°C for 12 minutes; i.e., 0.9 A/cm^2.

II.3.4 BSCCO thick film printed on YSZ substrate.

Although there was no second phase found from the x-ray diffraction pattern of the films, the BSCCO thick films printed on the YSZ substrates were not in the superconducting state at liquid nitrogen temperature after they were sintered at 830 to 850°C for 1 to four hours. When the film was fired at temperature higher than 860°C, the BSCCO 2212 phase was observed. The films also exhibited semiconducting behavior in

the critical temperature measurement. Serious interaction was observed between the BSCCO thick film and YSZ substrate. In order to eliminate the interaction between the BSCCO thick films and YSZ substrates, MgO coatings were applied to the YSZ substrates. The YSZ substrates became brittle after being coated with 10 layer of MgO. Deformation of the coated substrate was also observed after it was fired at 1550°C for 30 minutes. They were easily broken during the printing process.

A thin layer of BSCCO was coated on the YSZ substrate by a dip coating process and fired at 880°C for 10 minutes. The thin BSCCO film showed a preferred orientation in the (001) direction of the BSCCO 2212 phase, as shown in Figure 6. A BSCCO thick film deposited on the BSCCO coated YSZ substrate and fired at 845°C for 60 minutes possessed a critical temperature of 88.4K, as revealed by Figure 7. The BSCCO thin film coated on the YSZ substrate was found to be a high conductivity material, and thus, YSZ was not considered as an appropriate substrate material for the SAFIRE application.

II.3.5 BSCCO thick film on MSZ substrate.

The electrical properties of the BSCCO thick films were improved, when the films were fired in an 8% oxygen atmosphere. A BSCCO thick film printed on MSZ substrate and fired at 845°C for 2 hours had a T_c of 82K at 20μA measuring current. The BSCCO thick film printed on MSZ substrate did not show superconducting behavior at liquid nitrogen temperature when it was heat-treated at 845°C for 2 hours in air. The improvement in the electrical properties of the BSCCO thick films was also enhanced by applying a MgO buffer layer between the BSCCO superconductor and the MSZ substrate. Figure 8 shows the T_c curve of a BSCCO thick film printed on a MSZ substrate with 5 layers MgO coating. The film was fired at the same conditions as the former sample, which had no MgO buffer layer. The critical temperature of this film increased to 89K at 20μA measuring current, which was 7K higher than the sample without the MgO buffer layer. The film consisted of a BSCCO 2223 phase as shown by the x-ray diffraction pattern in Figure 9. The BSCCO superconductor thick films usually had relatively low

critical currents and critical temperatures when they were sintered at 845°C. It might be because of a porous microstructure in the film as seen in Figure 10. A more dense microstructure was obtained from the film fired at 860°C or higher, as shown in Figure 11. The crystal structure of the film sintered at 860°C, however, was a BSCCO 2212 phase, which has a lower critical temperature than the BSCCO 2223 phase. Therefore, the best firing conditions of the BSCCO thick films printed on YSZ substrates were at 845°C for 1 to 2 hours in low oxygen atmosphere. Applying the MgO buffer layer was also recommended.

II.4 Summary.

The following is the summary of the fabrication conditions for the YBCO and BSCCO thick films printed on the Zirconia-based substrates:

1. YBCO thick film.

   Substrate material : 8% YSZ.

   Film composition : $YBa_2Cu_3O_{7-x}$.

   Firing condition

   Heating rate : 3°C/min.

   Firing temperature : 990°C, 10 minutes.

   Cooling rate : 2°C/min.

2. BSCCO thick film.

   Substrate material : MSZ with MgO coating.

   Film composition : $(Bi_{1.6}Pb_{0.4})Sr_{1.9}Ca_{2.05}Cu_{3.05}O_x$.

   Firing condition

   Heating rate : 3°C/min.

   Firing temperature : 990°C, 10 minutes.

   Cooling rate : 2°C/min.

III. The use of YBCO and BSCCO Oxide Electrodes for Ferroelectric Devices.

III.1 Introduction.

Having a same structure as ferroelectric perovskites, $YBa_2Cu_3O_{7-x}$ (YBCO) and $(Bi_{1.6}Pb_{0.4})Sr_{1.9}Ca_{2.05}Cu_{3.05}O_x$ (BSCCO), which have relatively lower resistivity than ferroelectric materials, offer a possibility that they could be used as the electrode materials for ferroelectrical materials. Also because they have similar crystal parameters and chemistry , the YBCO and BSCCO show a strong structural compatibility with ferroelectric materials. The dielectric and ferroelectric properties of a PZT thin film were reported to be improved by applying the YBCO as the bottom electrode of a thin film[4,5]. Identical results were obtained from YBCO and gold electroded PZT substrates[6].

In this report, the preliminary results of the electrical properties, i. e. dielectric and ferroelectric properties, of the YBCO and BSCCO electroded ferroelectric materials are included.

III.2. Experimental Procedure.

Ferroelectric ceramics of compositions PLZT(9.5/65/35) and PBNZT (8/2/55/45) were used as substrate materials in this study. Electrode materials used were $YBa_2Cu_3O_{7-x}$, $(Bi_{1.6}Pb_{0.4})Sr_{1.9}Ca_{2.05}Cu_{3.05}O_x$, and silver paste(Du Pont). The YBCO and BSCCO powders were prepared by conventional mixing oxide processes[1,3]. The YBCO powder was also mixed with Ag_2O in ratios of 30%Ag_2O : 70%YBCO and 50%Ag_2O : 50%YBCO. The electrodes were applied to the ferroelectric materials by a painting process. Oxide pastes were prepared by mixing the YBCO or BSCCO with α-terpineol in a 3:1 ratio. According to the electrode materials applied and the type of the substrate used, the firing conditions of the electrodes were determined. The silver electrodes were fired at 550°C for 30 minutes. The YBCO electrodes were fired at a temperature from 920 to 940°C for 30 minutes to 2 hours. The BSCCO electrodes were

heat-treated at temperature from 840 to 870°C for 1 to 2 hours. Dielectric constant vs. temperature and dissipation factor vs. temperature of the samples were measured. The P-E loops of the samples were measured in the temperature range from room temperature to -100°C.

III.3 Results and Discussion.

III.3.1 Silver electrodes on PLZT (9.5/65/35).

In order to investigate the influence of the oxide electrodes on the ferroelectric material, the properties of the ferroelectric materials with silver electrodes were used as references for the properties of the oxide electroded samples. Figure 12 shows the P-E loops of a silver electroded sample at different temperatures. At room temperature, this sample was similar to a slim loop ferroelectric since it had only a small memory. When the measuring temperature was lowered to -80°C, the sample exhibited more ferroelectric behavior which was caused by a phase transformation in the material. The remanent polarization (P_R) and coercive field (E_c) of the sample at this temperature were 24.7 $\mu C/cm^2$ and 11.2 KV/cm, respectively. The domain switching kinetics, however, were retarded by lowering the measuring temperature. It took about 2 minutes to saturate the loop of the sample at -80°C compared to 10 seconds at room temperature and at 0°C. The dielectric constants of the sample at different temperatures were indicated in Figure 13. The sliver electroded sample had a Curie temperature at 50°C. Figure 13 also shows the dissipation factor of the sample as a function of temperature.

III.3.2 YBCO electrodes on PLZT (9.5/65/35).

Good interfacial adhesion between the YBCO electrodes and the PLZT substrate was observed when the sample was fired at 940°C for more than 1 hour. After firing, the YBCO electrode showed semiconducting behavior. The resistance of the YBCO film increased with decreasing the temperature.

At room temperature, a slim loop was obtained from the YBCO electroded PLZT sample which was fired at 940°C for 1 hour. The polarization of the sample at 10 KV/cm

(P_{10}) and 10 KV/cm (P_{20}) of this sample were 12.8 and 24.1 $\mu C/cm^2$, respectively. When the sample was cooled to -58°C, the sample possessed a ferroelectric behavior as indicated by the loop C in Figure 14. The retardation of the domain switching at low temperature, as seen in the silver electroded PLZT, was not observed from this sample at temperatures of -58°C and -88°C. These loops were plotted in about 10 seconds. When the YBCO electroded sample was cooled to -88°C, the E_c of the sample increased to 21.5 KV/cm, as listed in Table 2. It became more difficult to switch the domains of the PLZT material when the sample temperature decreased. The P_R of the sample also increased with decreasing the temperature.

Silver electrodes were painted on both sides of the YBCO electroded PLZT sample, after its electrical properties were measured. Since low contact resistance and ohmic contact interface were found in the high density silver paste (Cermalloy, C8710) and YBCO superconductor interface(7), this paste was applied onto the YBCO electroded sample and fired at 900°C for 12 minutes. The sample became a silver-YBCO-PLZT (SYP) one dimensional composite, after the silver electrodes were fired on the sample. Figure 15 shows the P-E loops of the SYP sample at different temperatures. As a slim P-E loop was observed with the YBCO electroded sample, a slim loop was also observed with the SYP sample at room temperature. The P_{10} of the loop was 12.0 $\mu C/cm^2$, and the P_{20} was 21.1$\mu C / cm^2$. When the temperature was decreased to -50°C or lower, the P-E loop of the SYP sample had about the same remanent polarization (P_R) value as the YBCO electroded sample. The coercive field (E_c) of the SYP electroded sample was higher than the YBCO electroded sample. More square loops were obtained from the SYP sample than those measured from YBCO electroded sample. The P_R values of the YBCO and SYP electroded samples became constant at temperatures between -80 and -100°C. In this temperature range, the E_c values of the YBCO and SYP electroded samples still increased with decreasing temperature. For this PLZT material, the difficulty of the domain switching increased with decreasing temperature. The different temperature

P-E loops of a 30% Ag_2O - YBCO (SY) electroded sample, which was fired at 930°C for 1 hour, are shown in Figure 16. At the same temperature as silver and YBCO electroded sample, the SY electroded sample had P_R and E_C values between the P_R and E_C values of those sample. Increasing the silver content in the electrodes decreased the P_R and E_C values of the PLZT material.

Figure 17 shows the dielectric constants of samples with various electrodes as a function of temperature. The Curie temperature of the YBCO-based electrode samples increase to 80°C or higher. This Curie temperature increasing mechanism is still not clear. The dissipation factors of the samples were also higher than those of the silver electroded sample at the same measuring temperature. The dielectric constant of the YBCO-based electroded samples, however, were lower than that of the silver electroded sample. The increase of the Curie temperature of the YBCO electroded sample might be caused by the formation of a interfacial layer between the PLZT and the electrodes. The dielectric constant of the interfacial phase should be temperature dependence to account for the Curie temperature shift. In order to understand the mechanism of the Curie temperature shift, the microstructural of the interface is currently under investigation.

III.3.3 BSCCO electrodes on PLZT (9.5/65/35).

A BSCCO electroded PLZT sample, which was fired at 845°C for 2 hours, possessed a slim P-E loop at room temperature as shown in Figure 18. The P_{10} and P_{20} values of the sample were 13.3 and 24.6 $\mu C/cm^2$, respectively. Figure 19 shows the dielectric constant and dissipation factor of the sample at different temperatures. The BSCCO electroded sample had a Curie temperature of 50°C which was the same as the Curie temperature of the silver electroded sample. The interface between the BSCCO electrode and the PLZT, therefore, had less influence on the PLZT properties than the YBCO-PLZT interface. The dissipation factor of the BSCCO electroded PLZT was higher than the silver electroded sample.

III.3.4 YBCO electrode on PBZNT

Figure 20 shows the room temperature P-E loops of the PBZNT substrates electroded with silver paste and YBCO. The same results were obtained from the silver electrode and YBCO electroded samples. The YBCO electrode was fired at 920°C for 1 hour. When the YBCO electrode on the PBNZT was fired at 930°C or higher, the electrode became green, which was due to formation of 211 (Y_2BaCuO_5) phase. Further investigating on the temperature dependence of the dielectric constant, dissipation factor, and ferroelectric behavior of the material are under way.

III.4 Summary.

The followings is a summary of the results obtained:

1. YBCO and BSCCO showed strong possibilities to be used as electrode materials for ferroelectric devices.
2. Reaction between the PLZT and YBCO electrode influenced the ferroelectric properties and dielectric constant of the PLZT (9.5/65/35).
3. Higher dissipation factor was obtained from the oxide electroded sample.

Reference:

1. C. S. Hsi and G. H. Haertling, NASA annual report, Contract No. NAG-1-1301, 1992.
2. W. Zhu and P. S. Nicholson, Appl. Phys. Lett. 61 [6], 717-719 (1992).
3. C. S. Hsi and G. H. Haertling, NASA annual report, Contract No. NAG-1-1127, 1992.
4. R. Ramesh, A.Inam, W. K. Chan, F. Tillerot, B. Wilkens, C. C. Chang, T. Sands, J. M. Tarascon, and V. G. Keramidas, Appl. Phys. Lett., 59 [27], 3542-3544 (1991).
5. R. Ramesh, W. K. Chan, B. Wilkens, A.Inam, F. Tillerot, T. Sands, J. M. Tarascon, and V. G. Keramidas, J. Electron. Mat., 21 [5], 513-518 (1992).
6. A. Srivastava, A. Bhalla, and L. E. Cross, Ferroelectrics, 122, 234-251 (1991).
7. C. S. Hsi, G. H. Haertling, and M. D. Sherrill, Rev. Sci. Intrum., 62 [5]. 1317-1320 (1991).
8. T. Hashimoto, T. Kosaka, Y. Yoshida, K. Fueki, and H. Koinuma, Jpn. J. Appl. Phys., 27, L384-L386 (1988).
9. K. Hosjino, H. Takahara, and M. Fukutomi, Jpn. J. Appl. Phys., 27, L1297-L1299 (1988).

Table 1: Critical temperature of multiple-lead YBCO thick films prepared at different temperatures.

Firing temperature(^{O}C)	Firing time(min)	Critical temperature(K)
970	10	80
970	60	80.7
980	12	83.3
985	12	86.3

Table 2: The remanent polarization (P_R) and coercive field (E_c) of the PLZT (9.5/65/35) with different electrodes. The samples were measured at different temperatures.

Electrode material	Firing conditions Temp.(°C)	Time(min)	Test Temperature(°C)	P_r(μC/cm^2)	E_c(KV/cm)
Silver paste	550	30	22	5	4.5
			0	7.8	6.5
			-80	24.7	11.2
YBCO	940	60	22	1.2	1
			0	3.6	2.5
			-58	22	17
			-88	26.5	21.5
SYP	900	12	22	1.5	1.5
			0	6.0	4.5
			-50	21	13.5
			-80	26.2	25
			-100	26.2	30.5
30% Ag_2O-YBCO	930	60	22	3	2
			-50	13	6.5
			-80	22	15
			-100	25.3	20.5

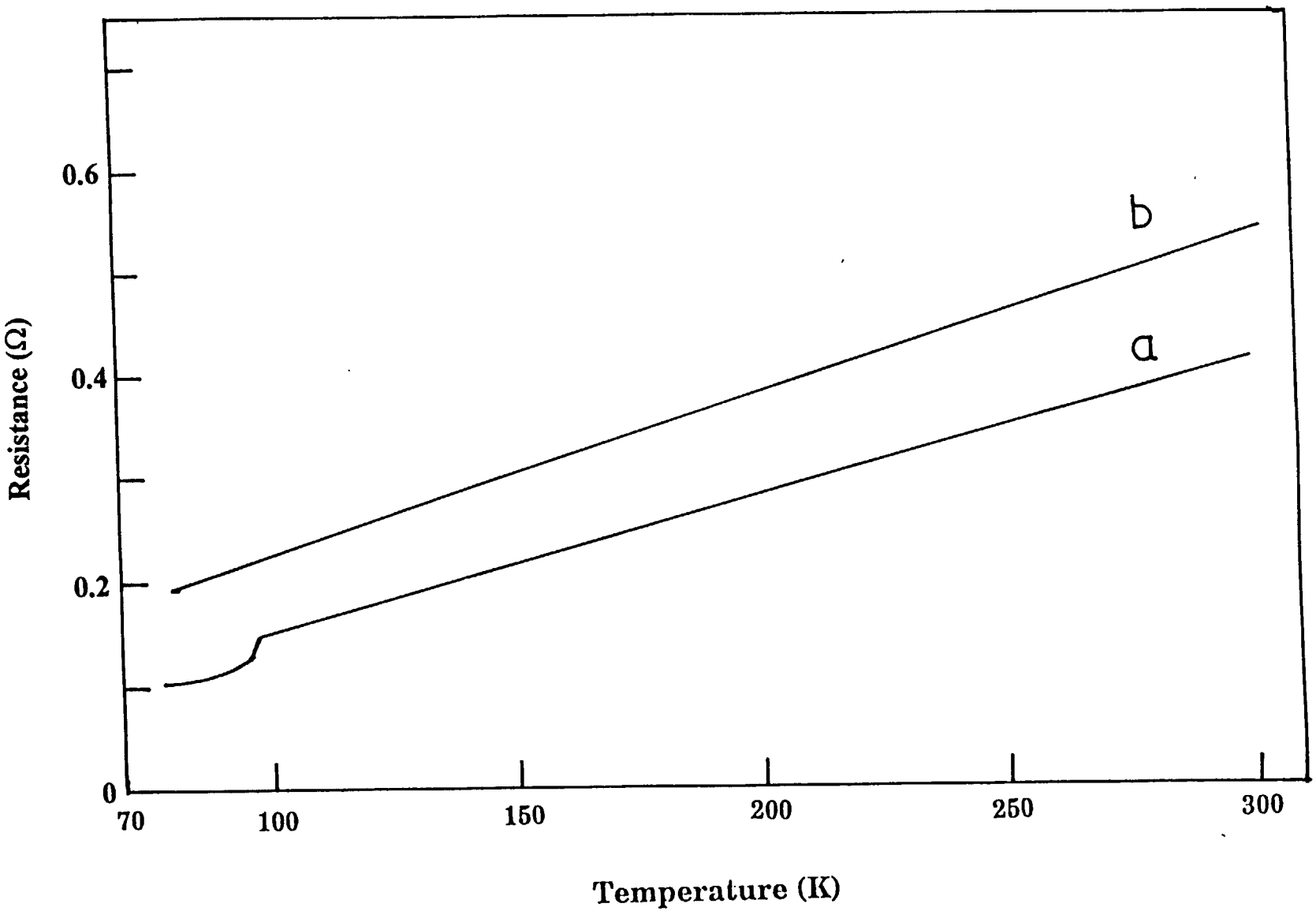

Figure 1: Resistance vs. temperature of (a) 30%Ag_2O-YBCO thick film printed on YSZ and (b) 20% Ag_2O-YBCO thick film printed on MSZ substrate.

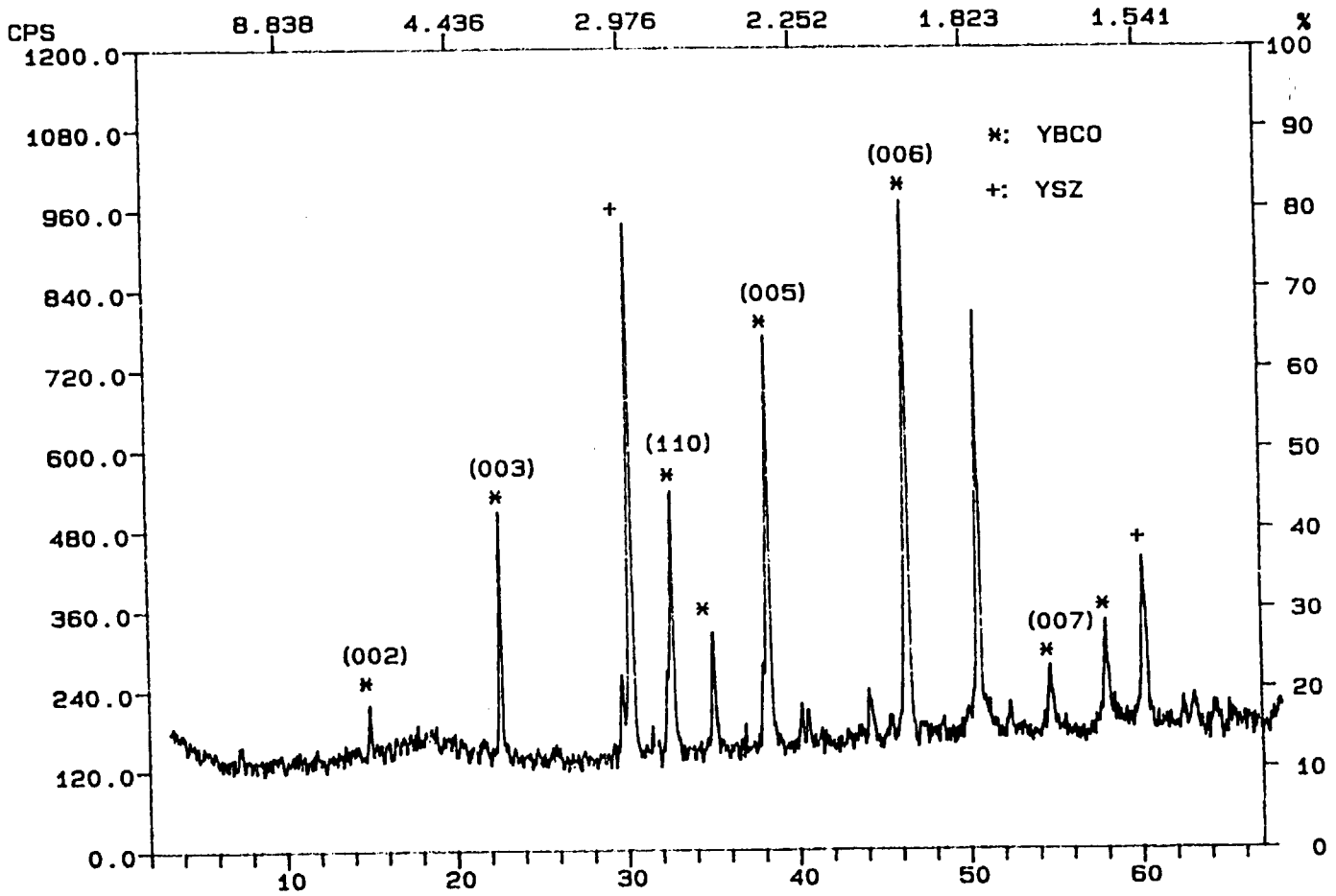

Figure 2: X-ray diffraction pattern of a 20%Ag_2O-YBCO thick film printed on MSZ substrate.

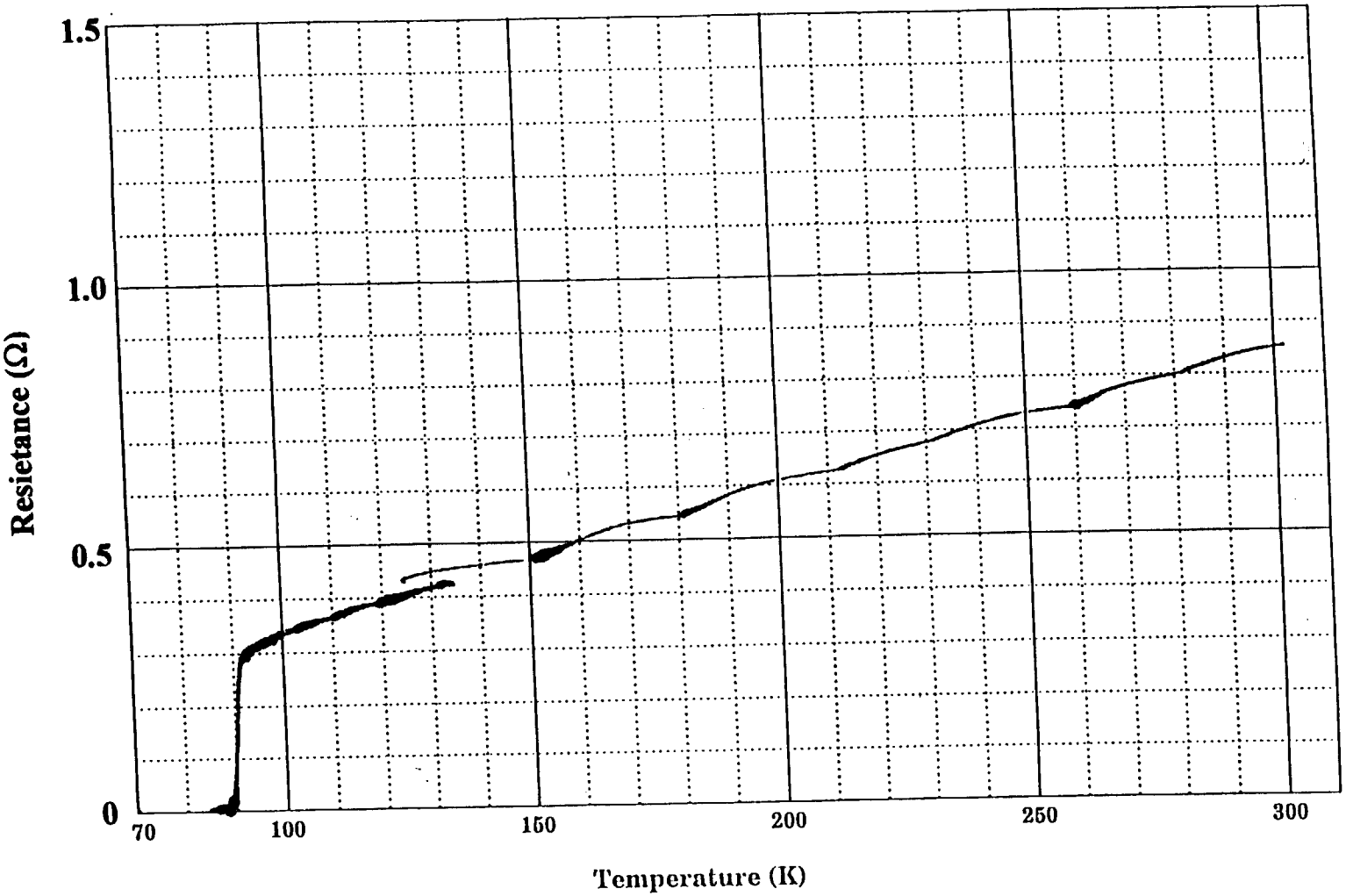

Figure 3: T_c curve of a YBCO thick film prepared by the two step firing process.

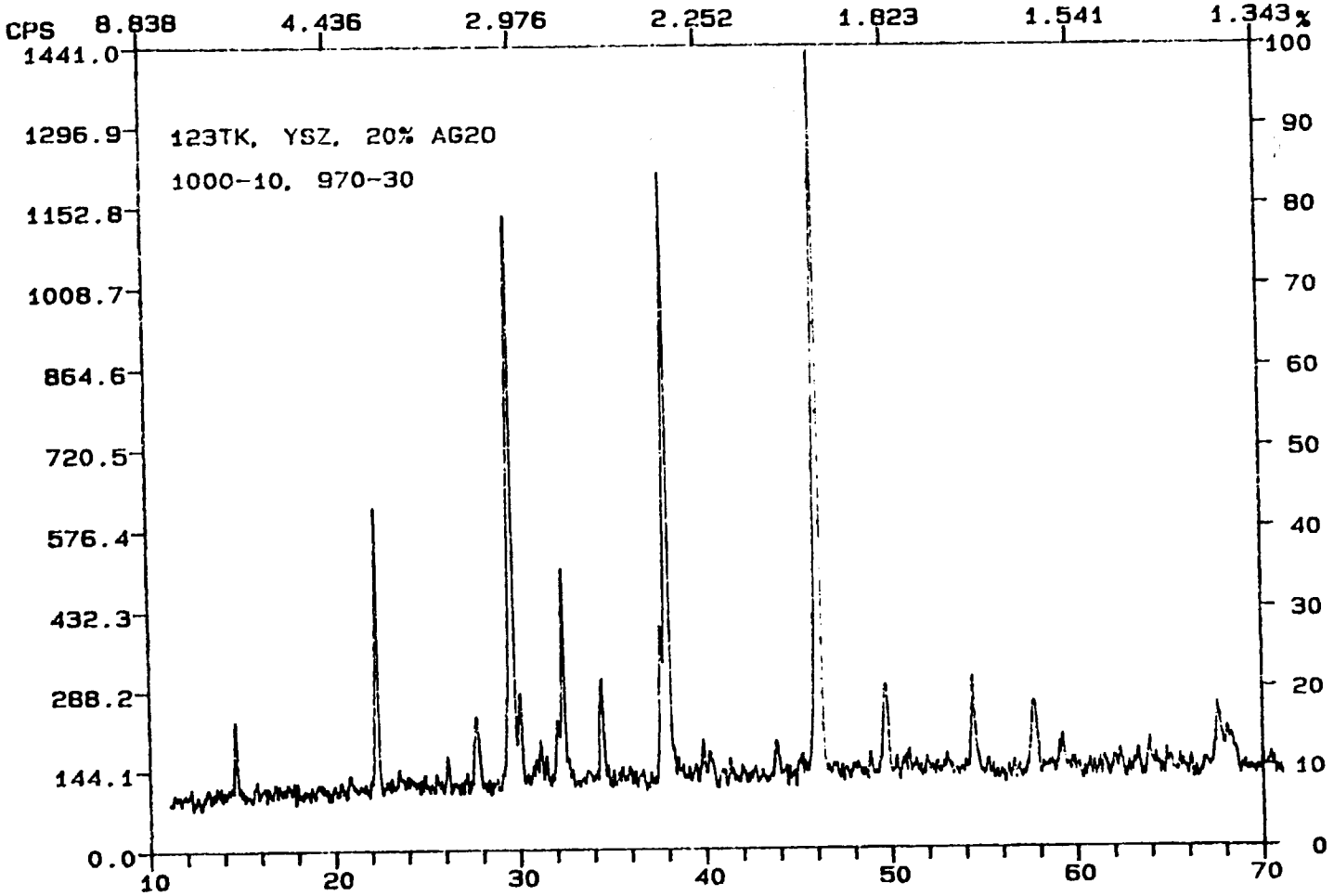

Figure 4: X-ray diffraction pattern of a YBCO thick film prepared by the two step firing process.

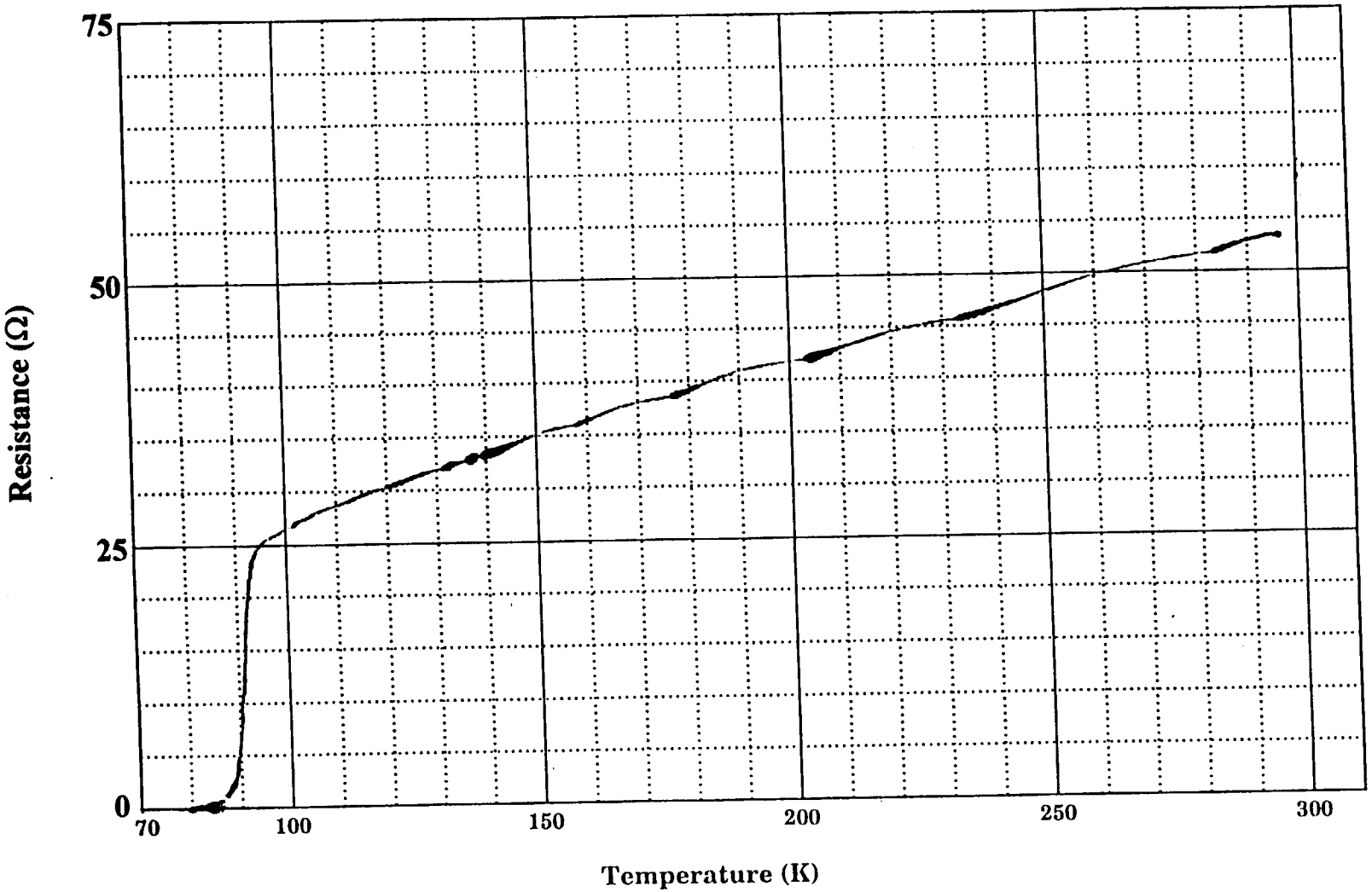

Figure 5: T_c curve of a multiple-lead YBCO thick film printed on YSZ and fired at 985°C for 12 minutes.

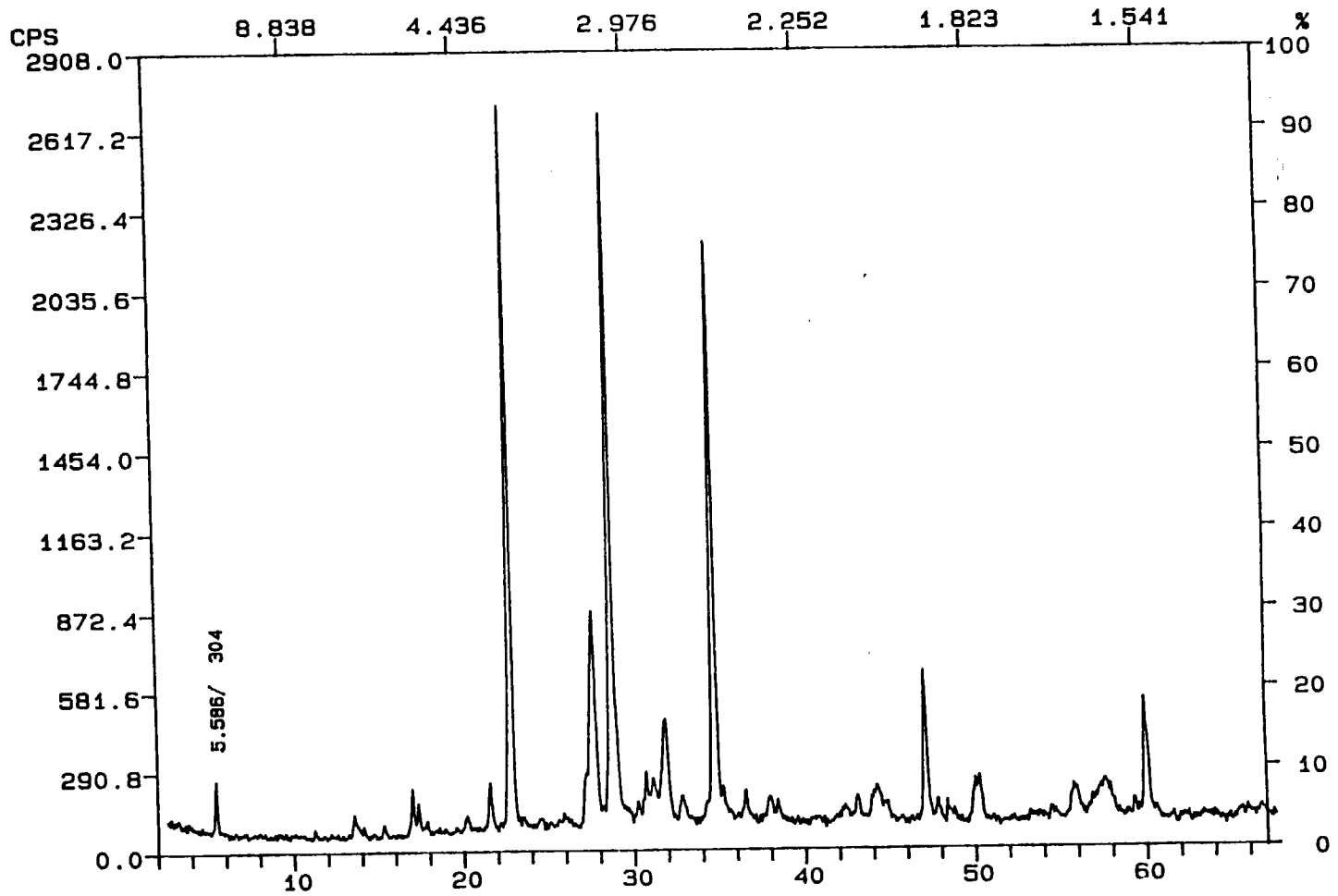

Figure 6: X-ray diffraction pattern of a BSCCO coated YSZ substrate.

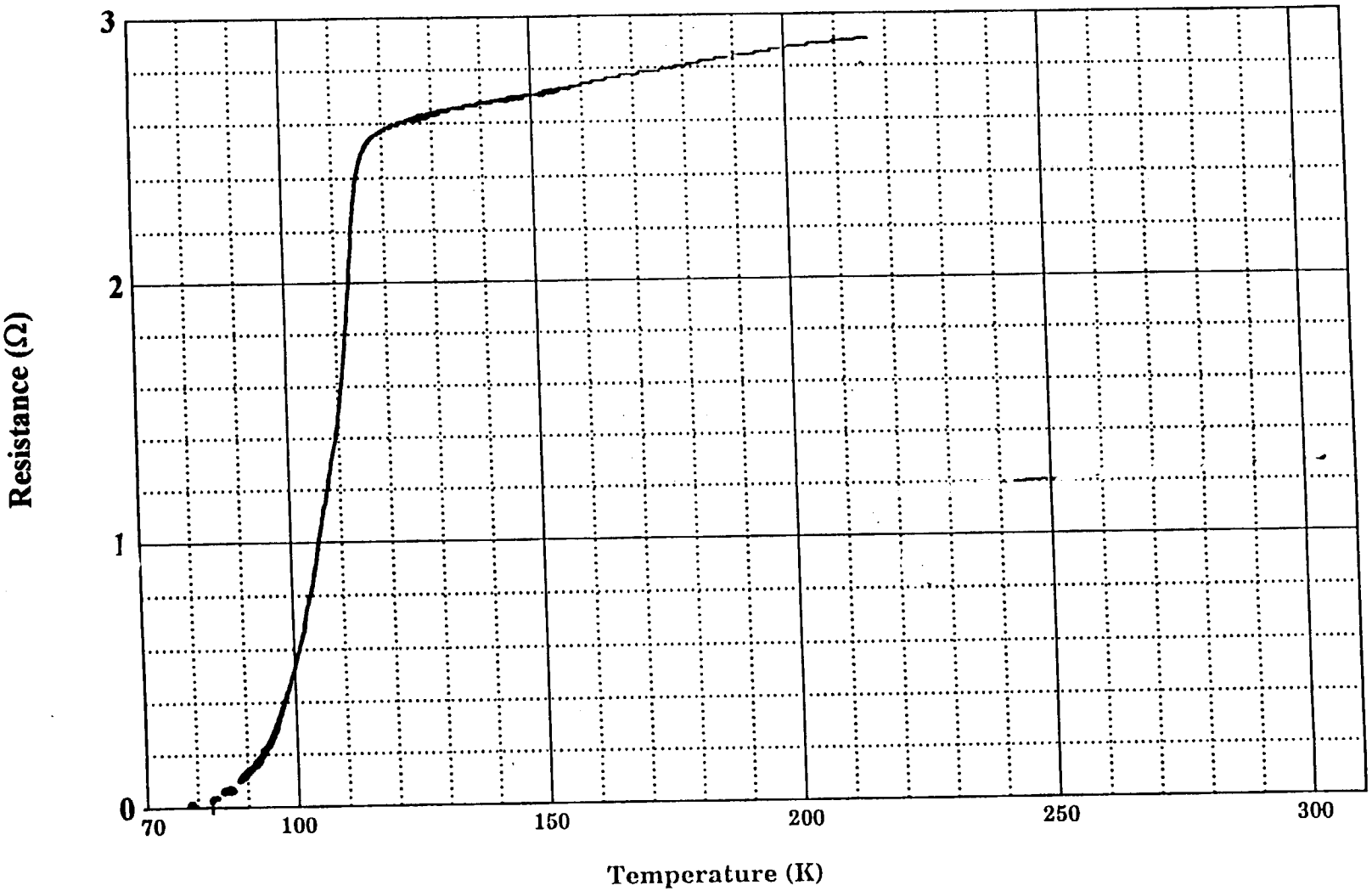

Figure 7: T_c curve of a BSCCO thick film deposited on the BSCCO coated YSZ substrate. The film was fired at 845°C for 2 hours.

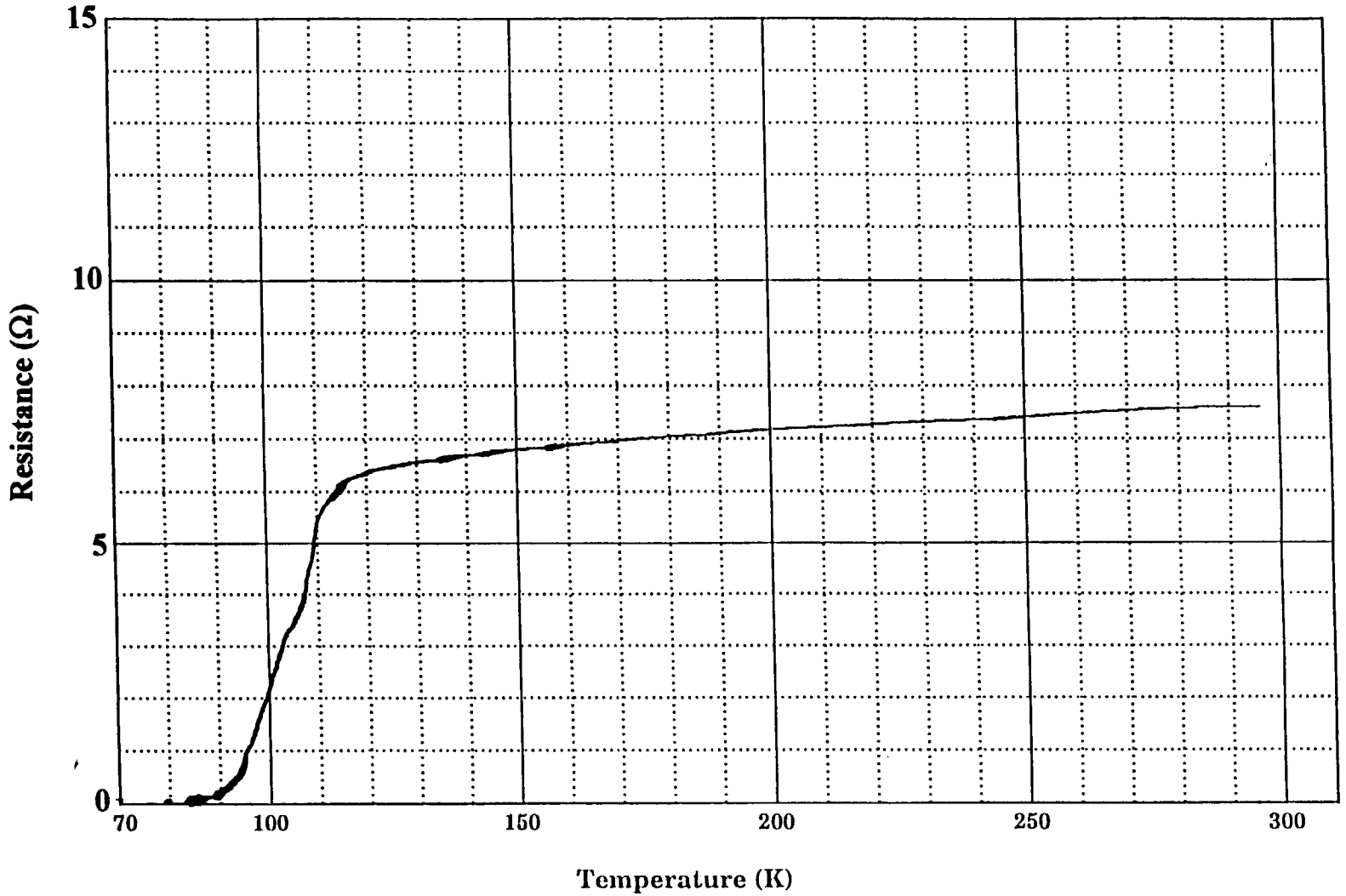

Figure 8: T_c curve of a BSCCO thick film printed on a MSZ substrate with 5 layers MgO coating. The film was fired at 845°C for 2 hours.

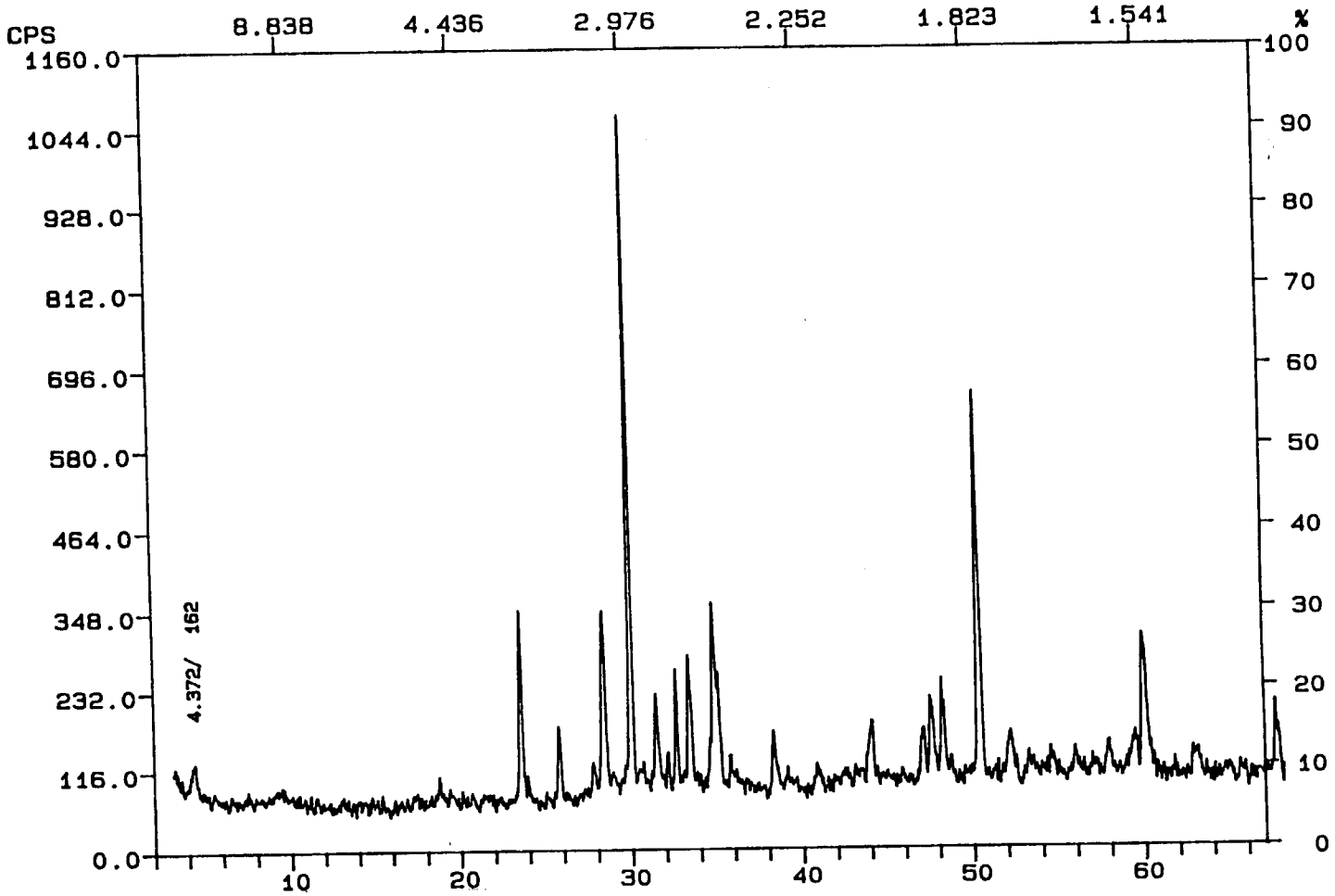

Figure 9: X-ray diffraction pattern of a BSCCO thick film printed on a MSZ substrate with 5 layers MgO coating. The film was fired at 845^{o}C for 2 hours.

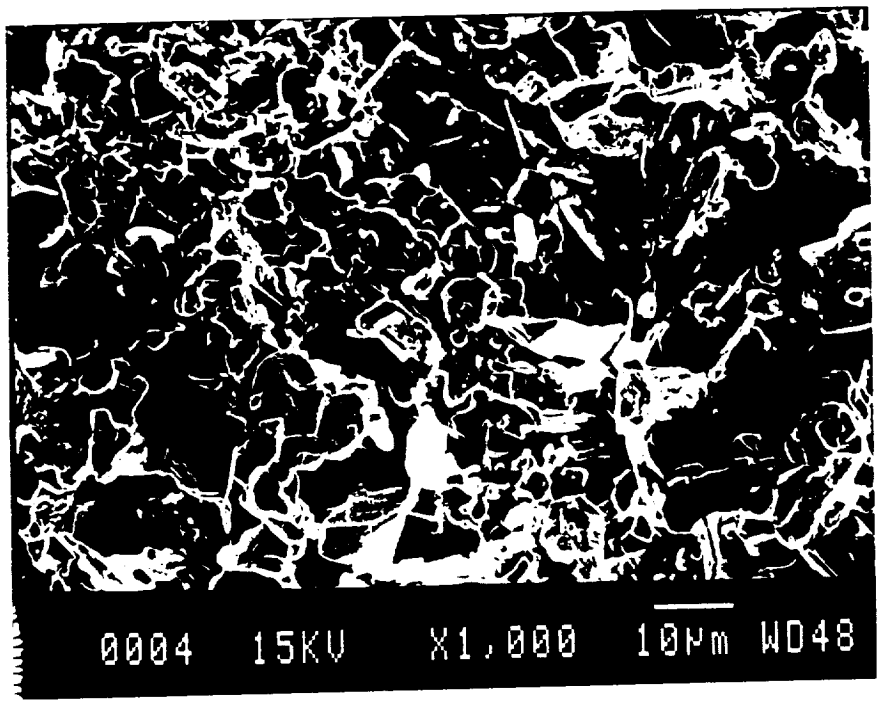

Figure 10: Microstructure of a BSCCO thick film printed on a MSZ substrate with 5 layers MgO coating. The film was fired at 845°C for 2 hours.

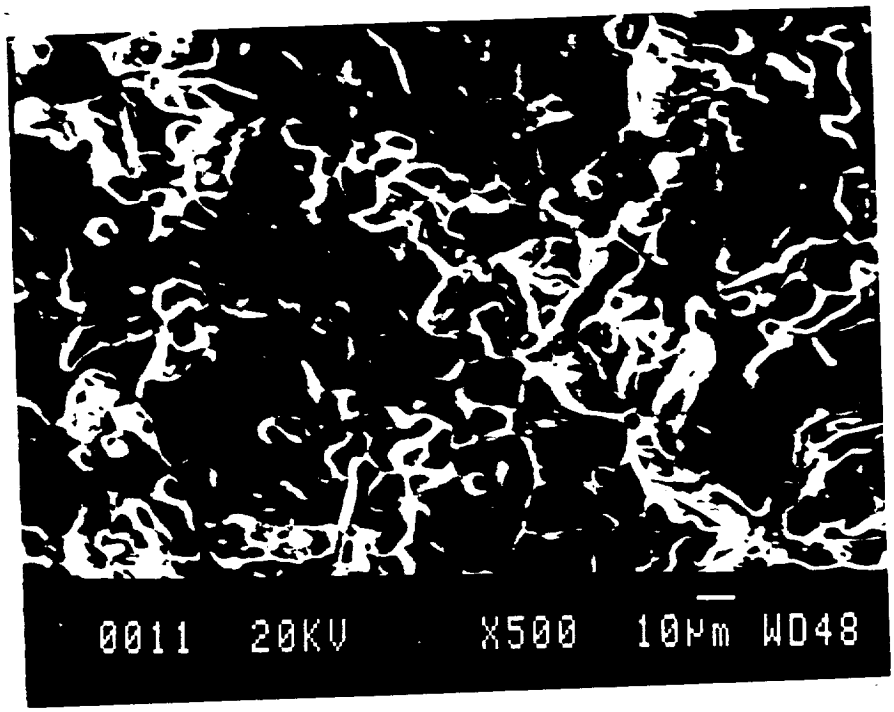

Figure 11:Microstructure of a BSCCO thick film printed on a MSZ substrate. The film was fired at 870°C for 30 minutes.

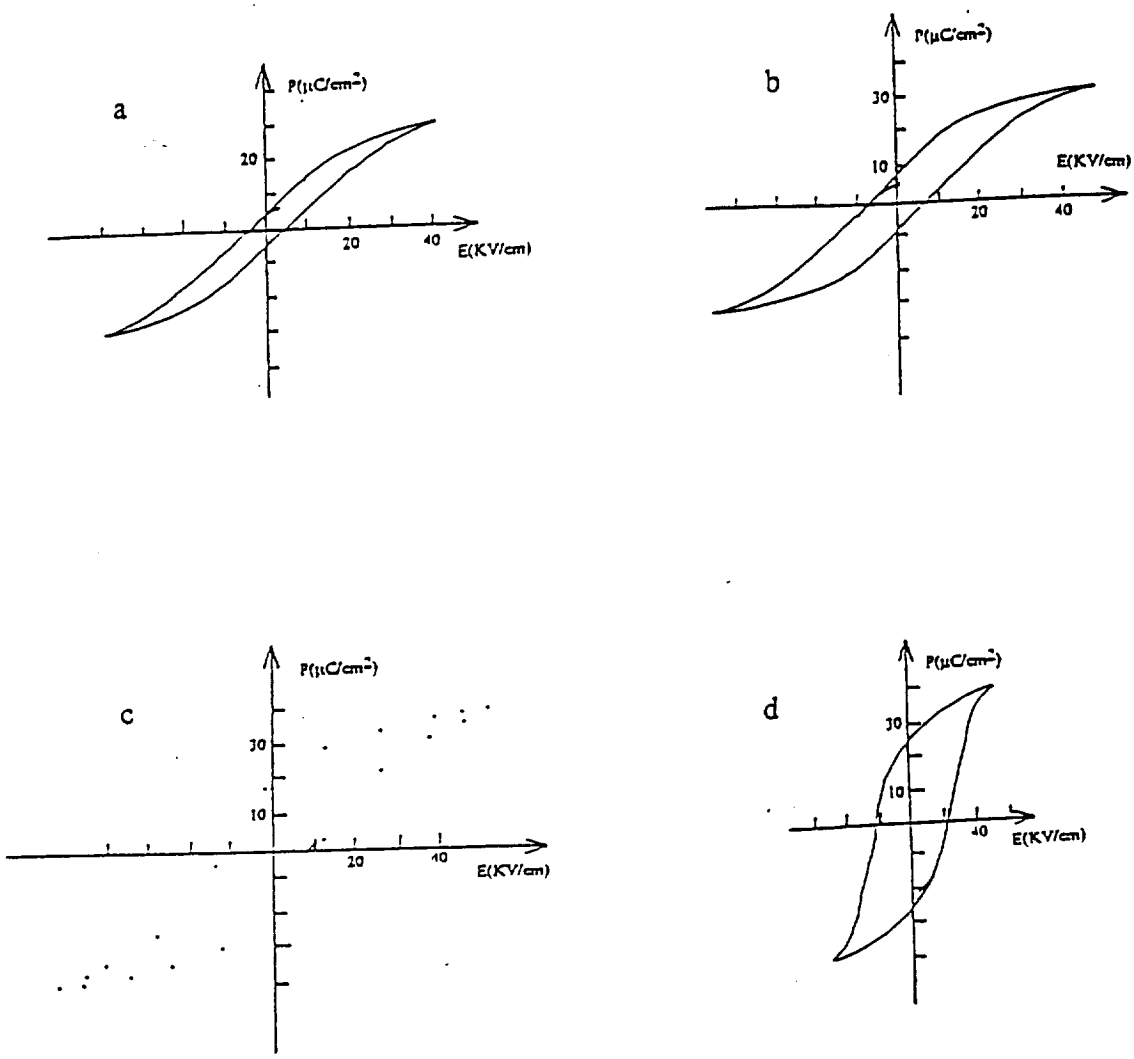

Figure 12:P-E loop of a silver electroded PLZT (9.5/65/35) at different temperatures. The sample was fired at 500°C for minutes. a: 22°C, b: O°C, c: -50°C, d: -80°C.

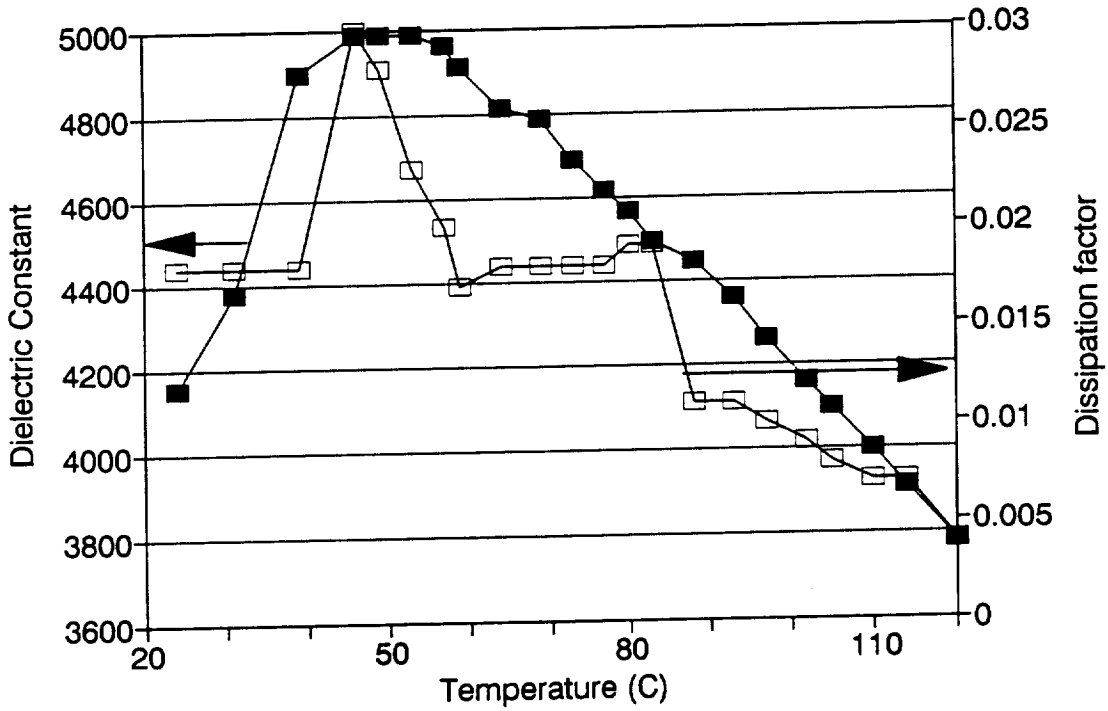

Figure 13: Dielectric constant and dissipation factor of a silver electroded sample. The sample was fired at 550°C for 30 minutes.

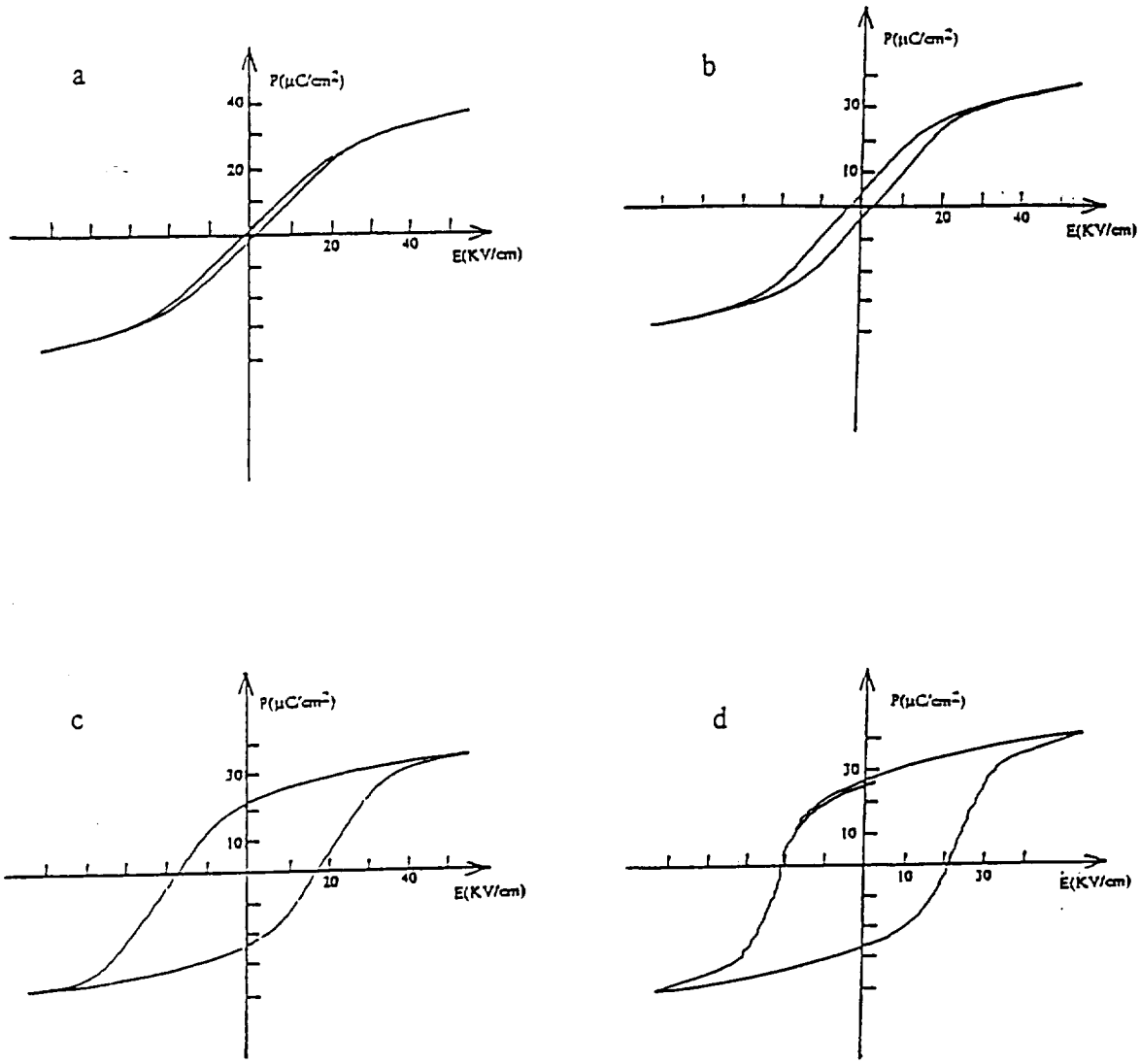

Figure 14:P-E loops of a YBCO electroded PLZT (9.5/65/35) at different temperatures. The sample was fired at 940°C for 1 hour. a: 22°C, b: 0°C, c: -58°C, d: -88°C.

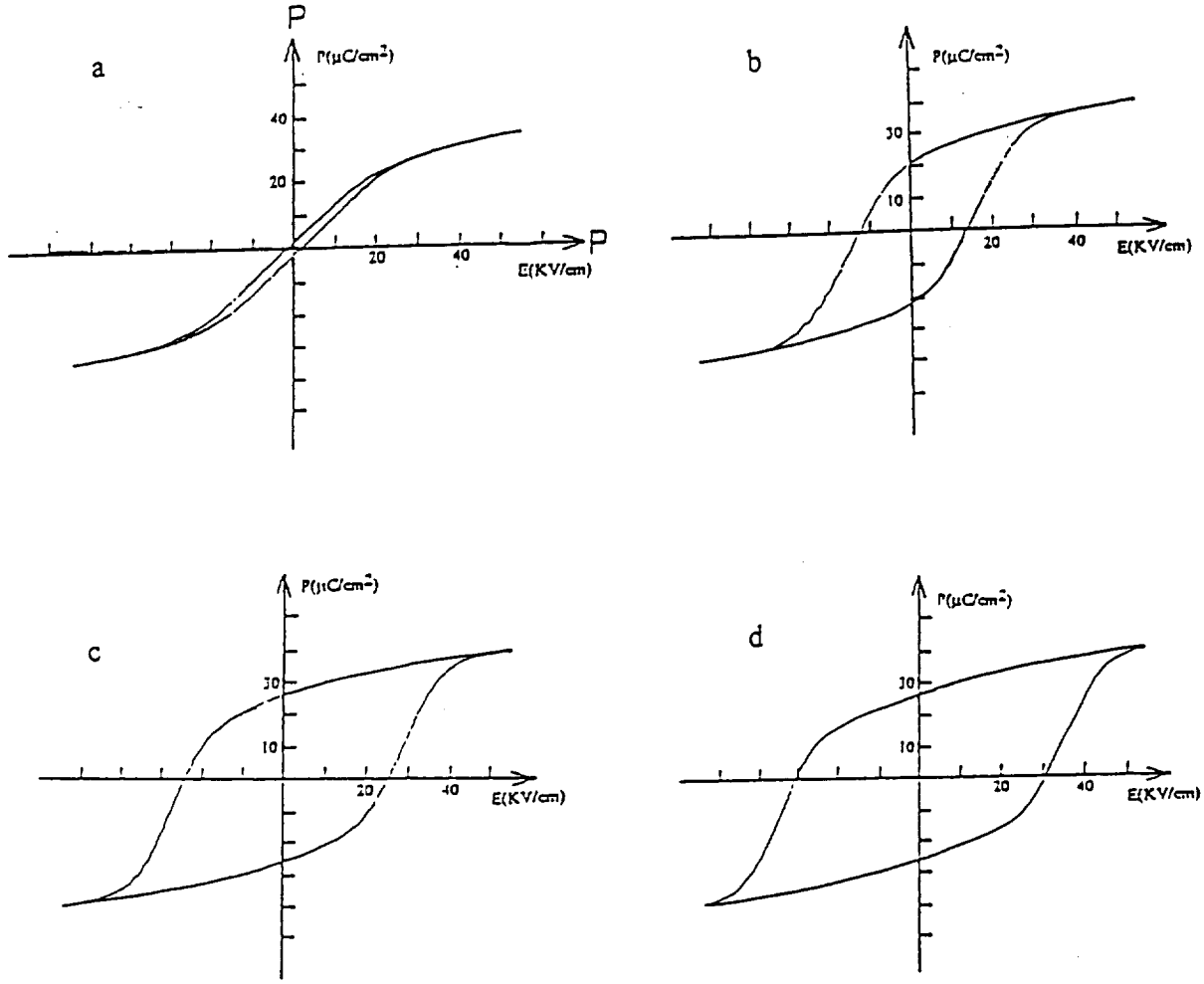

Figure 15:P-E loops of a SYP electroded PLZT (9.5/65/35) at different temperatures. The silver electrodes were fired at 900°C for 12 minutes. a: 22°C, b: -50°C, c: -80°C, d:-100°C.

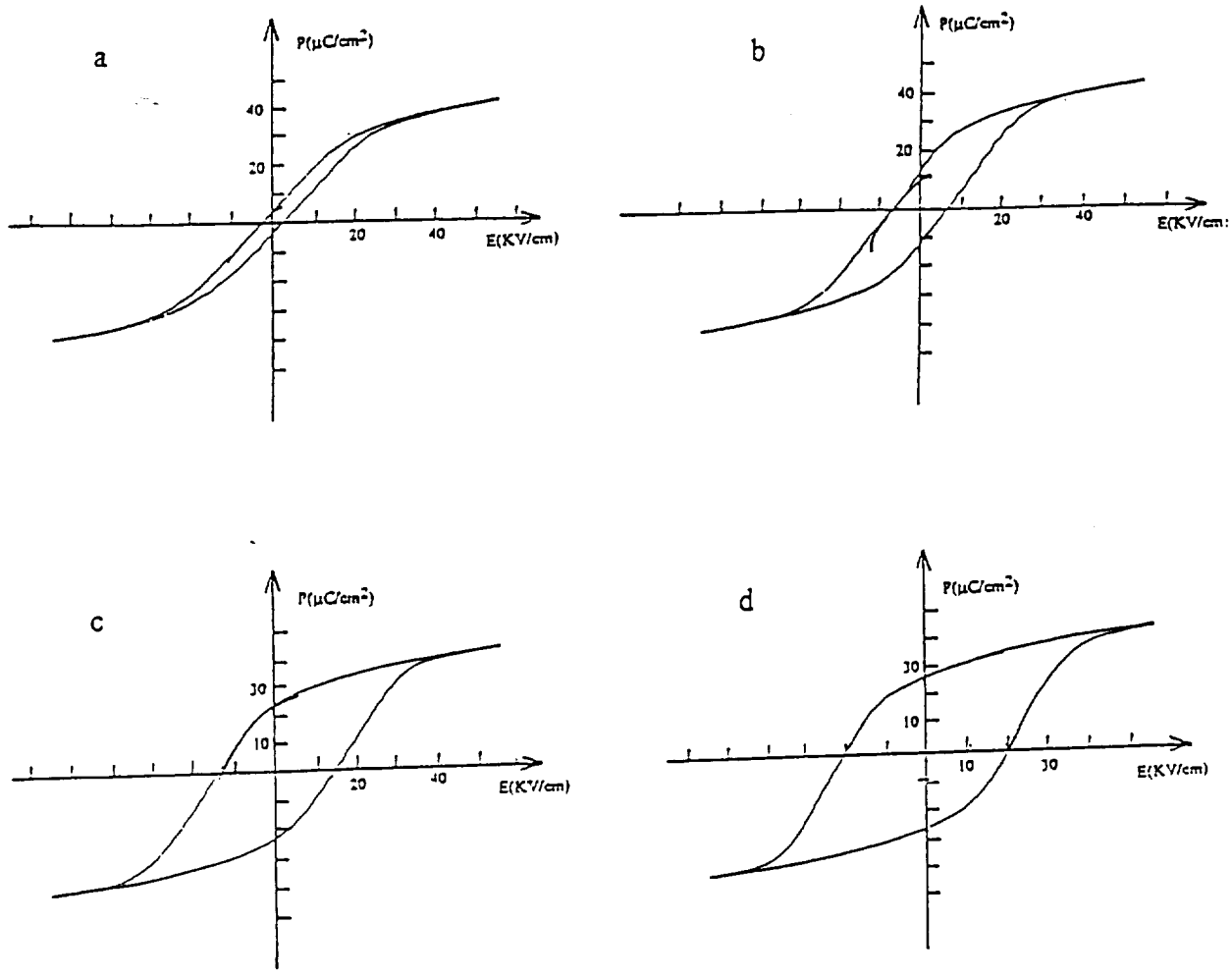

Figure 16:P-E loops of a SY electroded PLZT (9.5/65/35) at different temperatures. The sample was fired at 930°C for 1 hour. a: 22°C, b: -50°C, c: -80°C, d: -100°C.

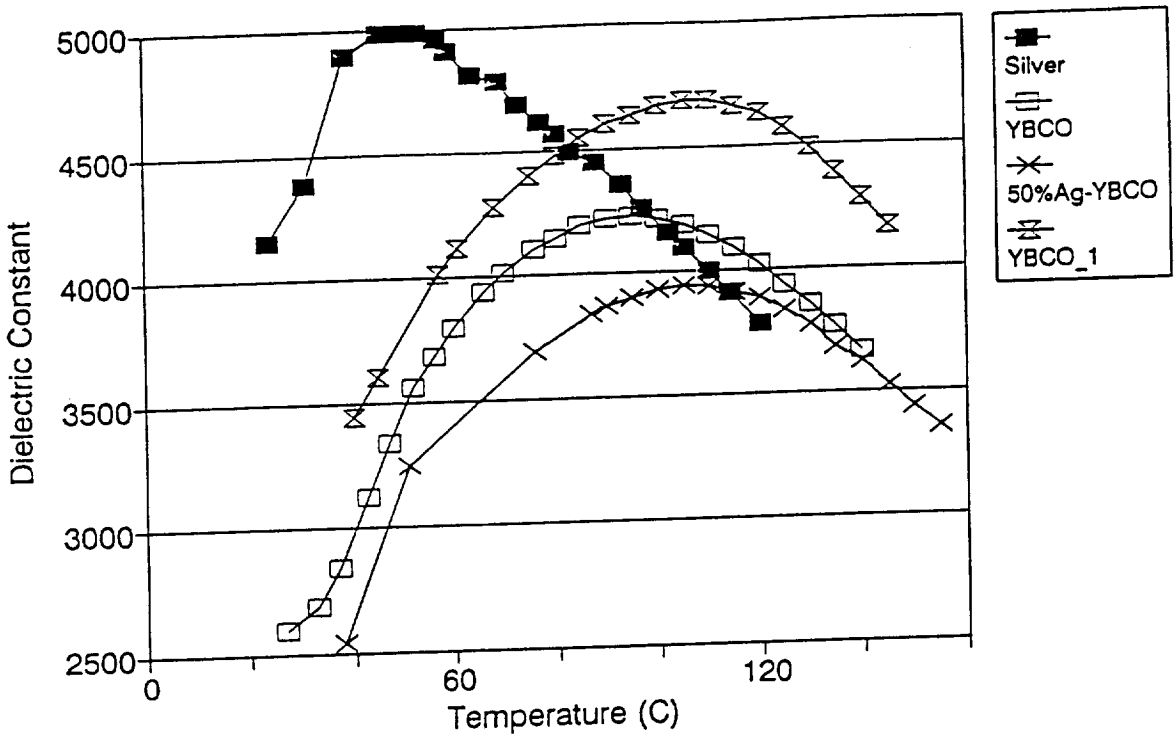

Figure 17:Dielectric constant of different electroded samples at different temperatures. YBCO: sample thickness was equal to15 mil, YBCO_1: sample thickness was equal to 27 mil.

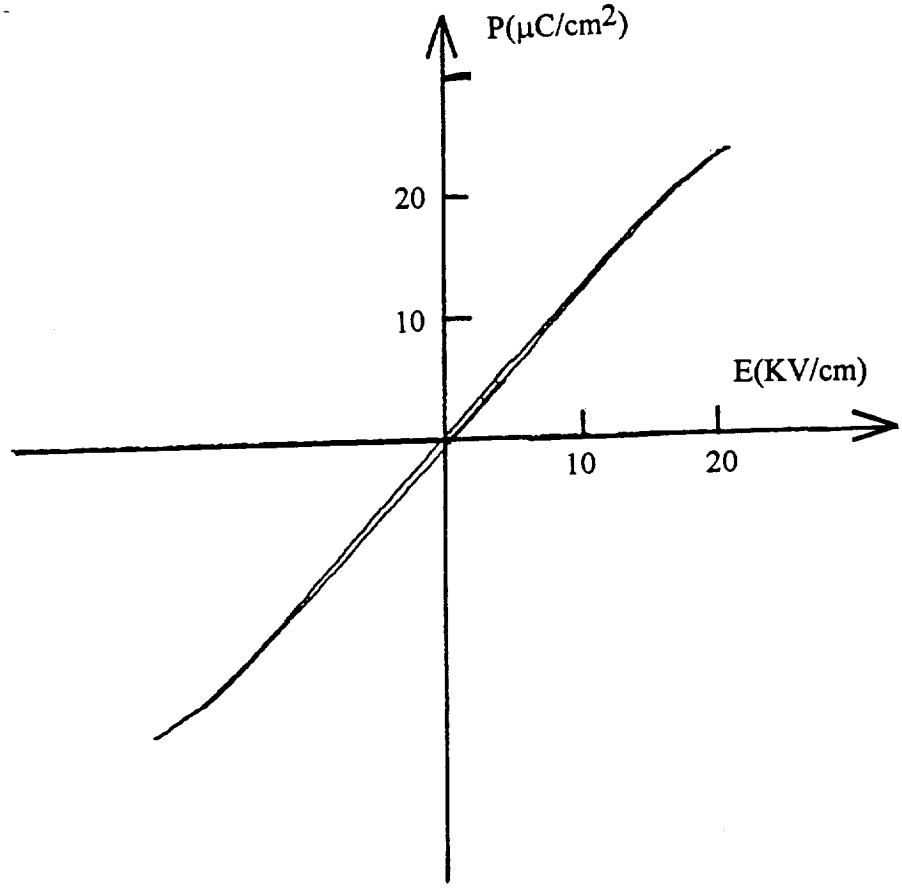

Figure 18:P-E loop of a BSCCO electroded PLZT (9.5/65/35) at room temperature. The sample was fired at 845°C for 2 hours.

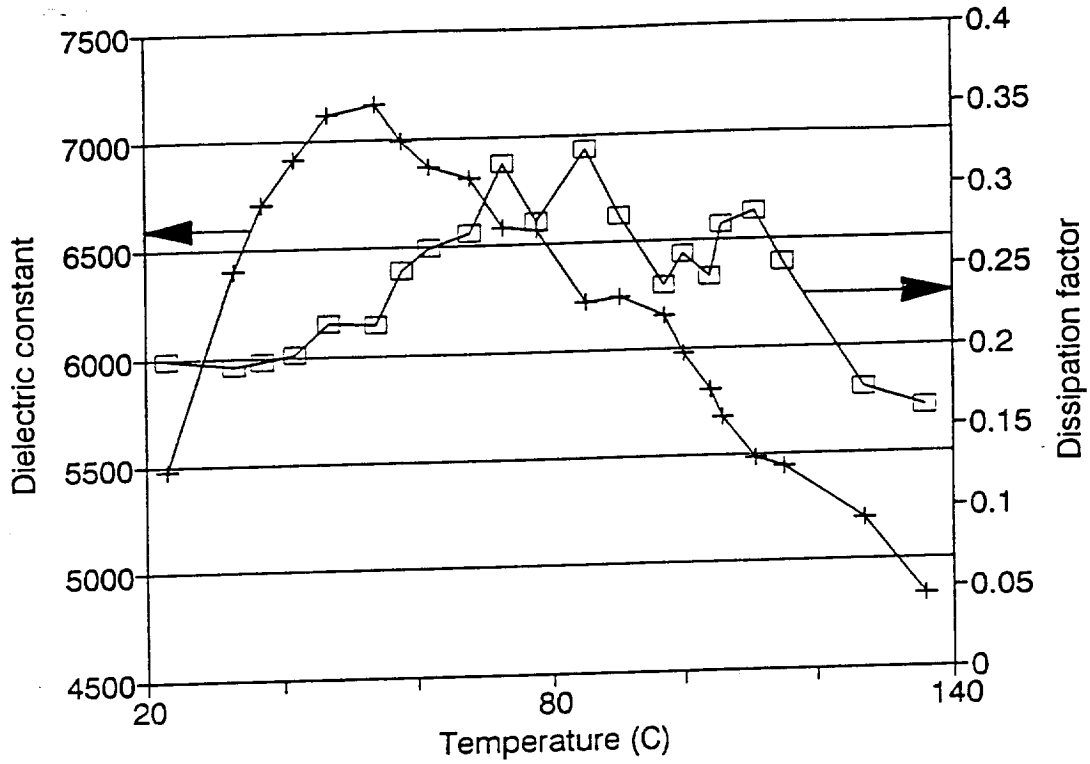

Figure 19: Dielectric constant and dissipation factor of a BSCCO electroded PLZT (9.5/65/35) at different temperature. The sample was fired at 845° for 2 hours.

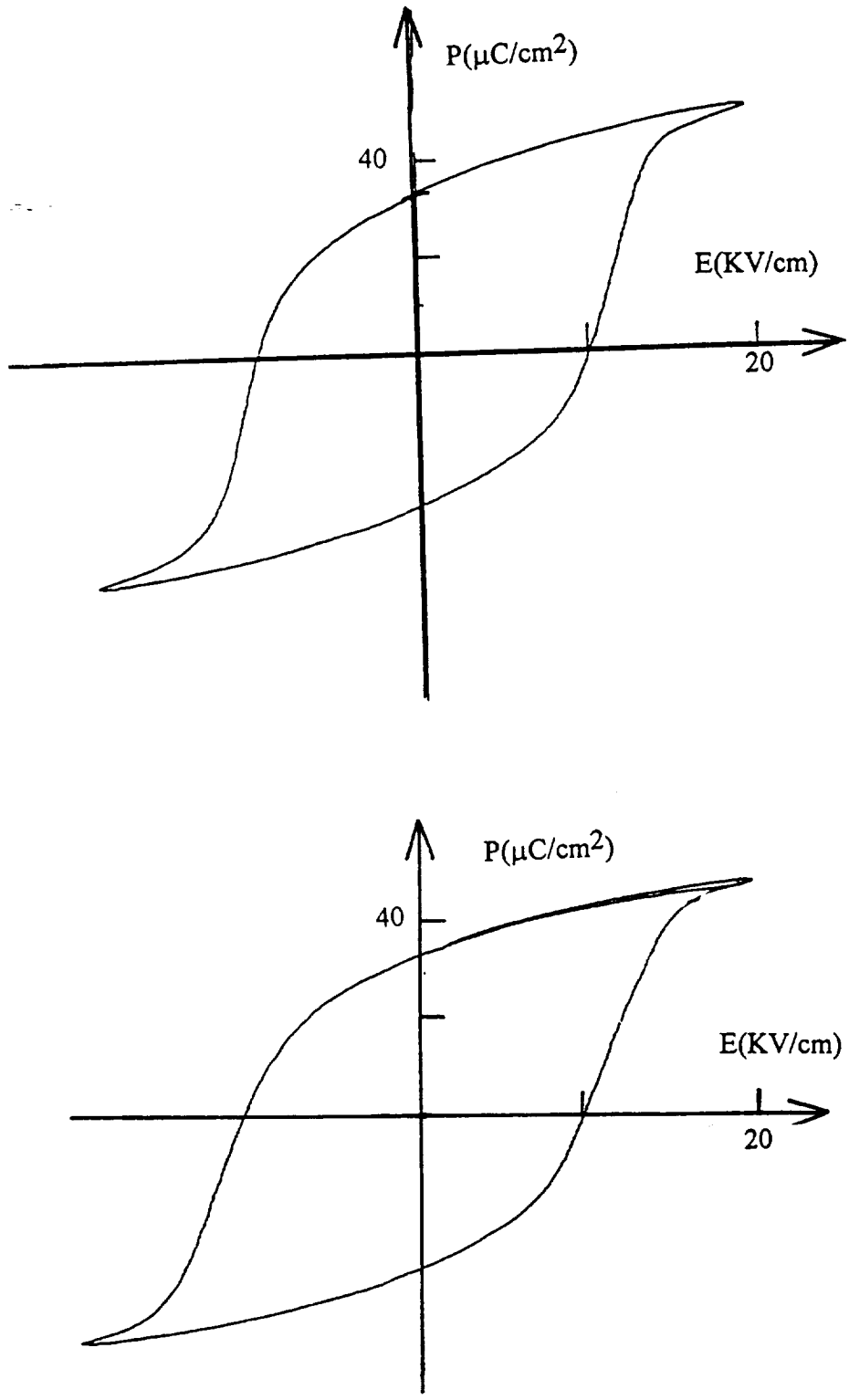

Figure 20:P-E loops of the PBNZT substrates electroded with silver and YBCO electrodes. The YBCO electrode was fired at 920°C for 1 hour.

Part II.

Semi–annual Report

SUPERCONDUCTIVITY DEVICES: COMMERCIAL USE OF SPACE

Development of PBZT and PLZT ceramics for Electrostrictive Actuators

to

National Aeronautics and Space Administration
Langley Research center
Hampton, VA 23665–5226

Principal Investigator:
Gene Haertling –Clemson University

Supporting Investigator:
Guang Li –Clemson University

Contract No. NAG–1–1301

March, 1993

1. Introduction

Our previous investigations [1] on the $(Pb_{1-x}Ba_x)(Zr_{1-y}Ti_y)O_3$ (PBZT) system indicate that the PBZT family belongs to a ceramic system with large electric field induced (electrostrictive) strains which possess many potential applications in electronic and optically controlled system as well as precision machinery. Current work is a continuation of the previous investigations with an objective that remains focused on the dielectric and electrostrictive properties of materials.

In this report, more compositions from the PBZT system were selected to be investigated so that the special regions of interest in the PBZT phase diagram were included. The dielectric properties and electrostrictive strains of the samples were measured. Several important parameters, such as E_c, P_R, P_{10}, S and ΔS, were evaluated. Additionally some (Pb,La)(Zr,Ti)O_3 (PLZT) samples of different compositions were prepared by conventional mixed–oxide processing and hot–pressing. The corresponding properties of the PLZT samples were determined and compared with PBZT.

2. Sample Preparation

The compositions of PBZT ceramics investigated are indicated in the $BaZrO_3$–$BaTiO_3$–$PbZrO_3$–$PbTiO_3$ phase diagram shown in Figure 1. The compositions were so chosen that most of them are situated along several lines in the phase diagram, either with constant Pb/Ba ratio or constant Zr/Ti ratio, which cover the regions of special interest.

Conventional mixed–oxide processing techniques were employed to prepare all of the PBZT samples. A flowchart of the processing is given in Figure 2. Reagent grade PbO, ZrO_2, TiO_2, $BaCO_3$ and Bi_2O_3 were used as starting raw materials. Here Bi_2O_3 was introduced mainly as an additive to enhance sinterability. Unless specified, 2 atom% Bi_2O_3 was used. Weighed components were first mixed for 30 minutes, and then calcined at 925 °C for two hours. The calcined powder was milled for 6 hours in distilled water using a polyethylene jar and Al_2O_3 balls. Sample pellets were obtained by pressing the milled powder with distilled water into plates of about 1.2x1.2x0.125 inches at a pressure of 7000 psi. The pellets were sintered at 1250 °C for 4 hours

in a closed alumina crucible with a flowing oxygen atmosphere. Higher sintering temperatures (about 1300 °C) were adopted for the samples with Zr/Ti >74/26. To avoid the loss of PbO from samples during sintering, a PbO–rich atmosphere was maintained by placing an equimolar mixture of PbO and ZrO_2 in the crucible. Sintered samples were then lapped to dimensions of 426x364x30 mil. The largest surfaces of the lapped samples were electroded with electroless nickel plating.

The PLZT samples are classified as two groups. One of them, called sintered PLZT samples, followed the same preparation procedures as those described above for PBZT. Another group, called hot–pressed samples, were prepared by means of a hot–pressing technique. These samples were hot–pressed at 1200 °C with a pressure of 2000 psi for 4 hours.

3. Measurements of Sample Properties

The dielectric properties of samples were measured at 1 kHz with an LCR meter (LEADER, LCR–7450–01). The temperature dependence of dielectric constant and loss factor were obtained by placing samples in an environmental chamber (DELTA DESIGN, 1740) in which samples were first cooled down to –20 °C and then measured at a heating rate of 3 °C/min up to 180 °C. The measurement of the relationship between polarization P and electric field E was carried out using conventional P–E hysteresis loop equipment. The submersion method in distilled water was employed to evaluate sample density.

An experimental device for the detection of electric field induced strains is depicted in Figure 3. An LVDT (linear variable differential transformer) was used as the displacement sensor. Details of the device have been given previously in the reference [1]. An electric field was applied to the samples continuously between negative and positive maxima (20 kV/cm). The measured results were recorded on a X–Y plotter.

Sample crystal structures were monitored with an X–ray diffractometer (Scintag XDS 2000™) with a filtered Cu radiation.

3. Results and Discussion

The important data of all the PBZT samples with different compositions obtained in this investigation are given in Table 1. The first six blocks of Table 1 illustrate, respectively, the dielectric and related properties of the compositions along the lines marked in the PBZT phase diagram of Figure 1. The variations of dielectric constant with barium content at constant Zr/Ti ratio, mainly the vertical lines 1–4 in Figure 1, are plotted in Figure 4. As shown in Figure 4, all four curves with different Zr/Ti values exhibited a maximum as barium content was increased, which were caused by the structural change from the rhombohedral F_R or tetragonal F_T phase to the paraelectric P_C phase. Figure 5 shows the change of dielectric constant with Ti concentration at constant Pb/Ba ratios; i.e., the horizontal lines 5 and 6 in Figure 1. A peak was found at about 20 atom% of titanium with Pb/Ba=73/27, which is consistent with the phase boundary given by Ikeda [2] as seen in Figure 1. No abrupt change in dielectric constant was observed near the F_R and F_T phase boundary at Pb/Ba=73/27, suggesting a strong compositional diffusion in this region. The presence of this boundary is indicated by the change of X–ray diffraction patterns with composition as given in Figure 6, whereby the intensity peaks featured by the tetragonal phase vanished as the sample composition varied across the boundary into the F_R phase. Similarly, the location of the F_T and P_C boundary at Zr/Ti=40/60 was determined from the X–ray measurement results as shown in Figure 7. Figure 8 illustrates the temperature dependence of dielectric constant and loss factor for some selected compositions along the lines 2, 4 and 5 in Figure 1. As anticipated, the temperatures of maximum dielectric constant, that is, the Curie points, decreased with decreasing Pb/Ba ratio along the lines 2 and 4, and with decreasing Zr/Ti ratio along the line 5 near the F_R and F_T phase boundary. In all cases the dielectric constant maxima appeared broad and became more diffuse as barium concentration was increased, and the magnitude of the corresponding loss factors dropped gradually above the Curie temperatures. This is an indication of the occurrence of structural relaxation. As for the sample density, no significant change was observed over the compositions studied. A desirable sintered density for those compositions with high Zr/Ti ratio was achieved by using higher sintering temperatures.

The relationships between polarization P and electric field E for all the PBZT samples were

measured. The coercive electric field E_c, the remanent polarization P_R and the polarization at an electric field of 10 kV/cm P_{10} for most of the samples were determined and are listed in Table 1. Figures 9–11 show the P–E relationships for the compositions along the lines 2, 3 and 4+6 in the phase diagram of Figure 1, respectively. The P–E relationship of some representative compositions was also projected on the PBZT phase diagram, as is depicted in Figure 12. It is evident in Figures 9–12 that as the barium concentration increased the P–E curves varied from the characteristics of a ferroelectric to a relaxor and then to a paraelectric phase. These three phases are generally identified, respectively, by a relatively square P–E hysteresis loop, a slim loop P–E curve with little or no memory and a linear P–E relationship. Based on this and the dielectric properties discussed above, a wide region characteristic of relaxor phase was outlined, which is indicated by the shadowed area in Figure 12. It is noted that the relaxor phase occurs mostly in between the F_R and P_c phases and becomes more narrow as it extends into the F_T phase.

The electric field induced (electrostrictive) lateral strain S_2 of all the PBZT samples and longitudinal strain S_1 of some samples were investigated. The curves of lateral strain vs. electric field for selected samples are presented in Figures 13 and 14. The S–E relationship of some representative compositions are also displayed in the phase diagram, as shown in Figure 15. It can be seen that as sample composition was changed from the ferroelectric phases into the relaxor phase the hysteresis of strain–electric field curves was reduced, and the variation of the strains with electric field strength approached a quadratic relationship exhibiting the characteristics of electrostrictive materials. The values of the strains $S_{1,10}$, $S_{2,10}$, $\Delta S_{1,10}$ and $\Delta S_{2,10}$ whose meanings are given in Table 1, were evaluated and are listed in Table 1 for comparison. It is noted that in general the strains are proportional to polarization, with a varied extent depending on the compositions involved. Both the total strains S and the differential strains ΔS were found to reach a maximum in the vicinity of the F_R and F_T phase boundary, whose values are among the highest discovered in the PBZT ceramic system.

Table 2 and Figure 16 show the influence of the Bi_2O_3 additive on the PBZT system. In addition to it significantly enhancing sample density, as initially expected, Bi_2O_3 behaved as if

an extra amount of equivalent BaO were added in the original pure PBZT composition, which is manifested as the P–E loop becoming slimmer with increasing bismuth content. This result is self–evident since Bi ions in the PBZT are substituted for Pb ions in A site of the perovskite structure as are Ba ions, which favors paraelectric over ferroelectric phases.

The dielectric and field induced strain properties of a number of hot–pressed PLZT ceramics are presented in Table 3. Analogous to the PBZT ceramics, the field induced strains were found to be strongly associated with the magnitude of polarization. The variations of polarization and lateral strain with electric field for the compositions with La=5.5 atom% are shown in Figures 17 and 18, respectively. Of the PLZT compositions studied, maximum total lateral strains $S_{2,10}$ (as high as 14.8×10^{-4}) occurred at the compositions close to the rhombohedral and tetragonal ferroelectric boundary where the polarization was maximized, as shown in Figure 19. The maximum of the differential lateral strain was, however, found to occur in the neighborhood of the intersection among the rhombohedral, tetragonal ferroelectric and relaxor phases. The relationship between polarization and electric field and the change of lateral strain with electric field for several compositions near the intersection with Zr/Ti=65/35 are given in Figures 20 and 21, respectively. Among the compositions displayed in Table 3, the composition 8.6/65/35 exhibits the largest $\Delta S_{2,10}$ value. Approximately speaking, as indicated in Figures 18 and 21, the strain increases linearly with electric field for the samples with relatively square P–E loop, whereas it varies with the square of field strength for those with a slim P–E loop. The later is usually referred to as electrostrictive strain. Large differential strain near ferroelectric and relaxor phase boundaries could be interpreted according to the behavior of microdomains under external and local electric fields. As shown in Figure 22, the microstructures of samples with composition close to the boundaries are characterized by isolated polar microdomains embedded in a matrix of nonpolar phase [4] [5]. In this situation, an internal depolarization field is induced to electrically compensate the corresponding microdomain so that the total energy is minimized. Upon the application of an external electric field to a sample, microdomains rotate and trend to align to the external electric field, thus generating strains macroscopically. At the same time, a local

electric field E_l is built up due to the rotation of microdomains away from the associated depolarization fields. When the external electric field is reduced, these local fields force the microdomains back to their initial directions. As a result, the sample is able to recover its initial shape with little remanent strain. For samples with large remanent polarization, ferroelectric domains are only separated by a thin domain wall and hence able to compensate each other electrically. In this case, there exists no such local field as described above that restores sample shapes when the external electric field is removed.

Table 4 lists the properties of sintered PLZT samples. Compared with the hot–pressed samples, the sintered samples exhibit no significant difference in dielectric constant. However, the electric field induced strains are approximately 15% less for sintered samples than for the hot–pressed. A probable reason for this may be the lower density of the former. The strain values of the sintered PLZT samples were found to be slightly higher than those of the highest found in the PBZT.

4. Conclusions

(1) A region in the PBZT room temperature phase diagram was revealed to exhibit the characteristics of a relaxor phase, which is situated between the rhombohedral (or tetragonal) and the paraelectric phases.

(2) A broad maximum in room temperature dielectric constant was identified within the relaxor phase area. No significant anomaly in dielectric constant along the rhombohedral and tetragonal boundary which was found in this study, suggesting a strong compositional diffusion in this compositional region. The location of the phase boundary was determined from the X–ray phase diffraction patterns.

(3) Remanent polarization and coercive field of PBZT samples decrease drastically at the ferroelectric and relaxor phase boundaries with decreasing Pb/Ba ratio.

(4) The electric field induced strains of the PBZT samples were found to be proportional to the polarization with a varied proportionality factor depending on the compositions involved.

Both total and differential strains reach a maximum in the vicinity of the rhombohedral and tetragonal boundary.

(5) The Bi_2O_3 additive significantly increased the density of pure PBZT samples.

(6) Very large electric field induced (electrostrictive) strains were discovered in the PLZT ceramics. The total strains are maximized around the boundary between the rhombohedral and tetragonal phases while the differential strains exhibit a maximum at the ferroelectric–relaxor boundaries. The later could be explained by the combined effect of local and external electric fields on microdomains.

(7) Sintered PLZT samples possess electric field induced strains about 20% smaller than those of the hot–pressed samples, resulting probably from the lower density of the sintered samples. The strain values of the sintered PLZT are slightly higher than those found in the PBZT.

5. References

[1] G. Haertling and G. Li, *Commercial Use of Space*, an annul report in the department of Ceramic Engineering, Clemson University, August 28, 1992.

[2] T. Ikeda, *J. Phys. Soc. Japan*, vol. 14(2), p168 (1959)

[3] G. H. Haertling and C. D. Land, *J. Am. Cer. Soc.*, vol. 54, p1 (1971).

[4] Z. W. Yin, *J. J. Appl. Phys.*, vol. 24, suppl. 24–2, p442 (1985).

[5] M. Yokosuka and M. Marutake, *J. J. Appl. Phys.*, vol. 25, No. 7, p981 (1986).

Table 1. Properties of PBZT ceramics.

	Dielectric Constant	tg δ (%)	ρ (g/cm^3)	E_c (kV/cm)	P_R ($\mu C/cm^2$)	P_{10}	$\Delta S_{2,10}$ $x10^4$	$S_{2,10}$ $x10^4$	$\Delta S_{1,10}$ $x10^4$	$S_{1,10}$ $x10^4$
19/84/16	460	4.4	6.88	5.0	20	26	–0.30	–1.20		
23/84/16	5250	11.5	6.97	1.5	4	26	–2.50	–2.53		
27/84/16	6270	11.1	6.94	2.0	3	20	–2.20	–2.20		
32/84/16	6370	5.7	6.98	2.5	4	18	–0.55	–0.55		
35/84/16	4110	1.9	6.97		1	8				
15/70/30	630	3.2	7.32	6.0	34	39	– 1.30	–4.40	--	--
20/70/30	1960	4.2	7.32	4.0	32	34	–1.80	–5.00	--	
25/70/30	5830	9.5	7.28		4	26	–4.27	–4.47	10.3	11.2
26/70/30	6110	9.7	7.22		3	21	–3.46	–3.46	--	
27/70/30	6400	10.0	7.19		3	18	–2.74	–3.10	8.50	8.50
29/70/30	7680	12.8	7.07		1	12	–1.20	–1.20	5.20	5.20
32/70/30	7790	6.6	7.05			8	–0.65	–0.65	--	
35/70/30	6730	2.3	6.99			6	–0.33	–0.33	--	--
43/70/30	5940	2.0	6.94			5	–0.33	–0.33	--	--
19/57/43	1450	2.6	7.38	5.0	34	40	–2.83	–10.00	--	--
23/57/43	3350	5.6	7.38	4.0	30	32	–3.00	–8.40	--	--
25/57/43	4110	8.1	7.35	3.0	17	27	–4.13	–7.20	--	--
27/57/43	5140	8.4	7.36	2.0	7	24	–5.53	–5.67	--	--
29/57/43	5410	8.7	7.34	2.0	4	19	–3.13	–3.67	--	--
32/57/43	6230	10.7	7.38		2	15	–1.10	–1.10	--	--
35/57/43	6270	7.8	7.38		1	11	–0.45	–0.45	--	--
40/57/43	4820	3.1	7.35			7	–0.25	–0.25	--	--
27/80/20	9180	11.0	7.07		1	19	–1.80	–1.80		
27/76/24	8050	11.1	7.16		2	19	–2.00	–2.00		
27/72/28	6480	10.1	7.18		2	17	–2.57	–2.57		
27/70/30	6400	10.0	7.19		3	18	–2.74	–3.10	8.50	8.50
27/68/32	6670	11.1	7.19		3	17	–2.47	–2.47	--	2.75
27/64/36	6090	10.8	7.26		4	18	–2.67	–2.73	--	--
27/60/40	5230	8.4	7.38	2.0	5	22	–3.67	–3.75	--	--
27/55/45	4760	7.8	7.34	2.5	10	24	–5.33	–5.67	--	--
27/52/48	4410	7.4	7.40	4.0	20	32	–4.34	–7.39	--	--
27/50/50	3840	4.2	7.40	7.5	21	29	–3.29	–6.18	--	--
27/47/53	2250	4.0	7.36	10.0	20	23	–2.00	–5.33	--	--

Table 1. Properties of PBZT ceramics (continued).

	Dielectric Constant	tg δ (%)	ϱ (g/cm^3)	E_c (kV/cm)	P_R	P_{10} ($\mu C/cm^2$)	$\Delta S_{2,10}$ $x10^4$	$S_{2,10}$ $x10^4$	$\Delta S_{1,10}$ $x10^4$	$S_{1,10}$ $x10^4$
35/40/60	1730	2.0	7.18	12.0	19	25	-1.10	-3.33		
40/40/60	4950	8.3	7.24	2.5	2	10	-1.10	-1.20		
45/40/60	5860	7.7	7.22			8	-0.40	-0.40		
40/35/65	1280	2.2	7.18	14.0	17	21	-1.10	-2.33		
40/40/60	4950	8.3	7.24		2	10	-1.10	-1.20		
40/45/55	5380	5.4	7.22		1	6	-0.20	-0.20		
40/50/50	6130	5.0	7.33		1	10	-0.20	-0.20		
40/57/43	4820	3.1	7.34			6			--	--
23/76/24	6030	9.9	7.06		4	22	-2.70	-2.80		
25/60/40	4490	7.4	7.34	3.0	20	36	-5.60	-7.00	--	--
25/55/45	4640	7.8	7.36	3.5	20	28	-3.20	-6.40	--	--
29/55/45	4800	8.8	7.29	2.0	2	18	-3.53	-3.80	--	--

Note: tg δ is the loss factor, ϱ the density, E_c the coercive field, P_R the remanent polarization, P_{10} the polarization at an electric field of 10 kV/cm, $\Delta S_{2,10}$ (lateral) and $\Delta S_{1,10}$ (longitidunal), the differential strains, are defined as the difference between the strains at an electric field of 10 kV/cm and 0 kV/cm, $S_{2,10}$ and $S_{1,10}$ are, respectively, the total lateral and longitidunal strains at an electric field of 10 kV/cm.

Table 2. Influence of additive Bi_2O_3 on the properties of pure PBZT ceramics.

	Dielectric Constant	tg δ (%)	ϱ (g/cm^3)	E_c (kV/cm)	P_R	P_{10} ($\mu C/cm^2$)	$\Delta S_{2,10}$ $x10^4$	$S_{2,10}$ $x10^4$	$\Delta S_{1,10}$ $x10^4$	$S_{1,10}$ $x10^4$
$27/70/30_{0*}$	4020	4.5	6.92	3.5	7	24	-3.70	-4.00		
$27/70/30_1$	5230	8.2	7.07	2.0	3	22				
$27/70/30_2$	6310	10.0	7.19	2.0	3	21	-3.33	-3.33		
$27/70/30_3$	6660	11.0	7.27	1.5	3	20	-1.80	-1.80		

* the mole percentage of bismuth oxide.

Table 3. Properties of hot-pressed PLZT ceramics

	Dielectric Constant	tg δ (%)	ρ (g/cm^3)	E_c (kV/cm)	P_R	P_{10} ($\mu C/cm^2$)	$\Delta S_{2,10}$ $x10^4$	$S_{2,10}$ $x10^4$	$\Delta S_{1,10}$ $x10^4$	$S_{1,10}$ $x10^4$
55560	1820	3.2		7.0	30	37	-5.3	-15.2		
55565	2320	3.0		9.0	27	31	-4.5	-13.7		
55570	1920	3.8		8.5	30	36	-4.2	-13.5		
55575	1600	3.7		8.0	32	36	-4.0	-13.5	10.0	36.5
55580	1690	3.8		8.0	32	36	-4.0	-14.0		
55585	1750	3.8		7.5	32	34	-3.8	-14.2	10.0	39.6
79700/6	5070	5.9		3.5	22	27	-2.7	-8.3		
79700/10	4800	5.8		2.0	5	24	-6.0	-7.7	20.0	23.7
120400	1130	2.2		12.0	20	22	-5.4	-3.0		
20540	1270	2.6		12.0	32	36	-3.8	-12.4		
23660/Sn	1120	2.3		7.0	32	36	-0.7	-2.0		
60650	1180	2.8		5.5	31	35	-2.7	-11.0	9.0	34.2
70650	2600	2.1		5.0	28	34	-2.4	-13.5		
80650	4970	4.1		3.0	23	33	-4.0	-12.0		
86650	5540	5.3		1.0	4	31	-8.2	-8.8		
88650	5700	5.9			1	30	-5.4	-5.7		
90650	6090	6.6				23	-3.6	-3.6	5.7	5.8
95650	6760	6.8				22	-2.4	-2.4		
96650	5750	6.0				17	-0.9	-0.9		
140650	1880	0.6				3				
50550	1760	2.5		12.0	27	33	-4.0	-11.2		
50560	1720	3.2		10.0	29	34	-4.7	-13.1		
50570	1560	3.5		9.5	30	34	-4.5	-13.0	10.0	28.0

Note: tg δ is the loss factor, ρ the density, E_c the coercive field, P_R the remanent polarization, P_{10} the polarization at an electric field of 10 kV/cm, $\Delta S_{2,10}$ (lateral) and $\Delta S_{1,10}$ (longitidunal), the differential strains, are defined as the difference between the strains at an electric field of 10 kV/cm and 0 kV/cm, $S_{2,10}$ and $S_{1,10}$ are, respectively, the total lateral and longitidunal strains at an electric field of 10 kV/cm. 60650 denotes 6.0/65.0/35 (La/Zr/Ti).

Table 4. Properties of sintered PLZT ceramics.

	Dielectric Constant	tg δ (%)	ρ (g/cm^3)	E_c (kV/cm)	P_R ($\mu C/cm^2$)	P_{10} ($\mu C/cm^2$)	$\Delta S_{2,10}$ x10^4	$S_{2,10}$ x10^4	$\Delta S_{1,10}$ x10^4	$S_{1,10}$ x10^4
55550	2250	2.6	7.55	12.0	30	37	–3.6	–9.4		
55560	2300	2.7	7.42	11.0	30	36	–4.0	–10.9		
55570	1820	3.2	7.33	7.7	34	40	–3.8	–12.6		
55580	1580	3.3	7.55	6.5	30	34	–2.8	–12.2		
55590	1590	2.7	7.56	7.0	32	34	–2.8	–12.6		
55600	1660	3.2	7.56	6.5	34	37	–3.7	–13.7		
55560/1	2830	2.6	7.67	11.0	34	39	–4.5	–11.3	--	--
86650/1	4890	6.7	7.58	3.0	20	27	–5.4	–8.3	--	--
86650/2	5370	6.9	7.61	3.0	20	33			--	--
86650_1	5120	6.7	7.61	4.0	34	37			--	--
86650_2	4530	6.9	7.61	4.0	34	37			--	--

86650_1: K906 Milled ZrO_2; 86650_2: CS Milled ZrO_2.

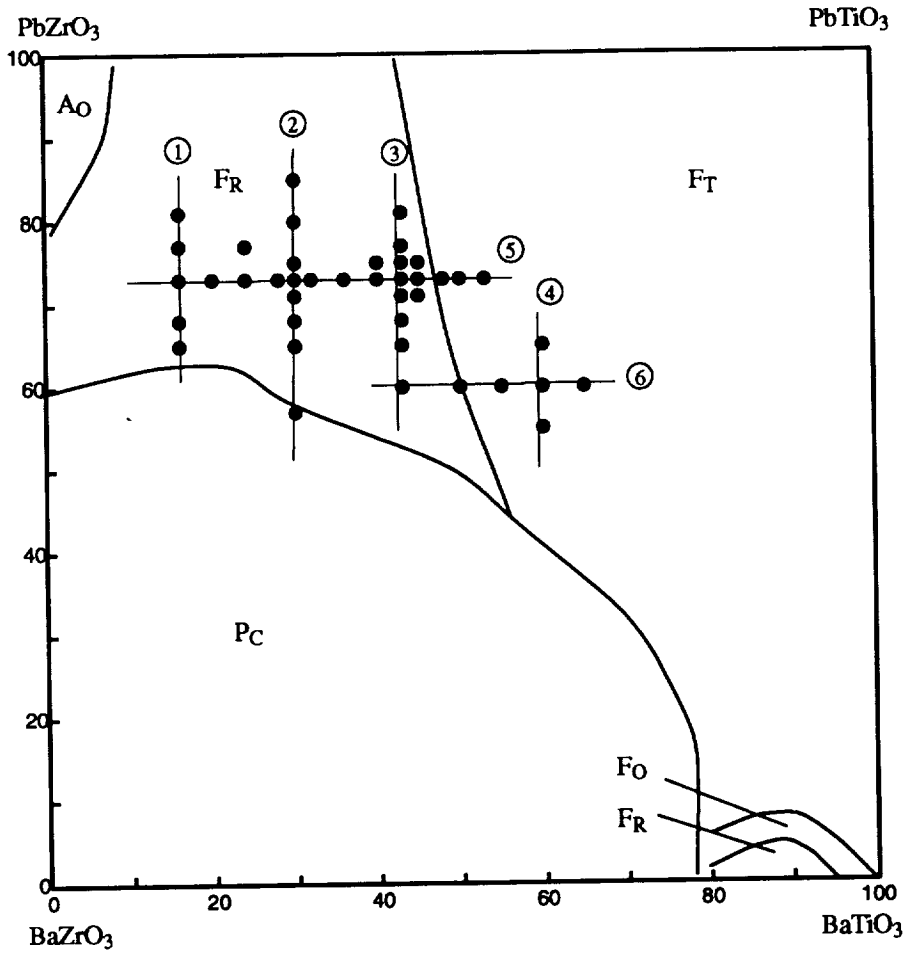

Figure 1. Room temperature phase diagram for the system $PbZrO_3$–$PbTiO_3$–$BaZrO_3$–$BaTiO_3$ (PBZT). where F_R denotes rhombohedral phase, F_T tetragonal phase and P_C paraelectric phase [2].

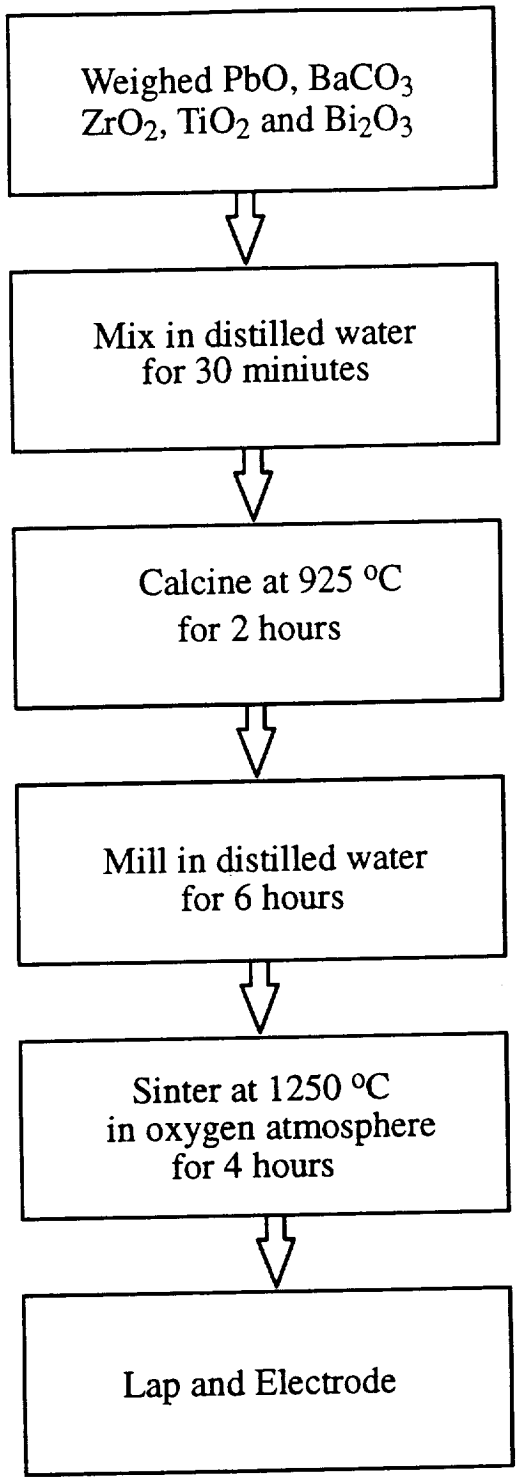

Figure 2. Flowchart of PBZT processing.

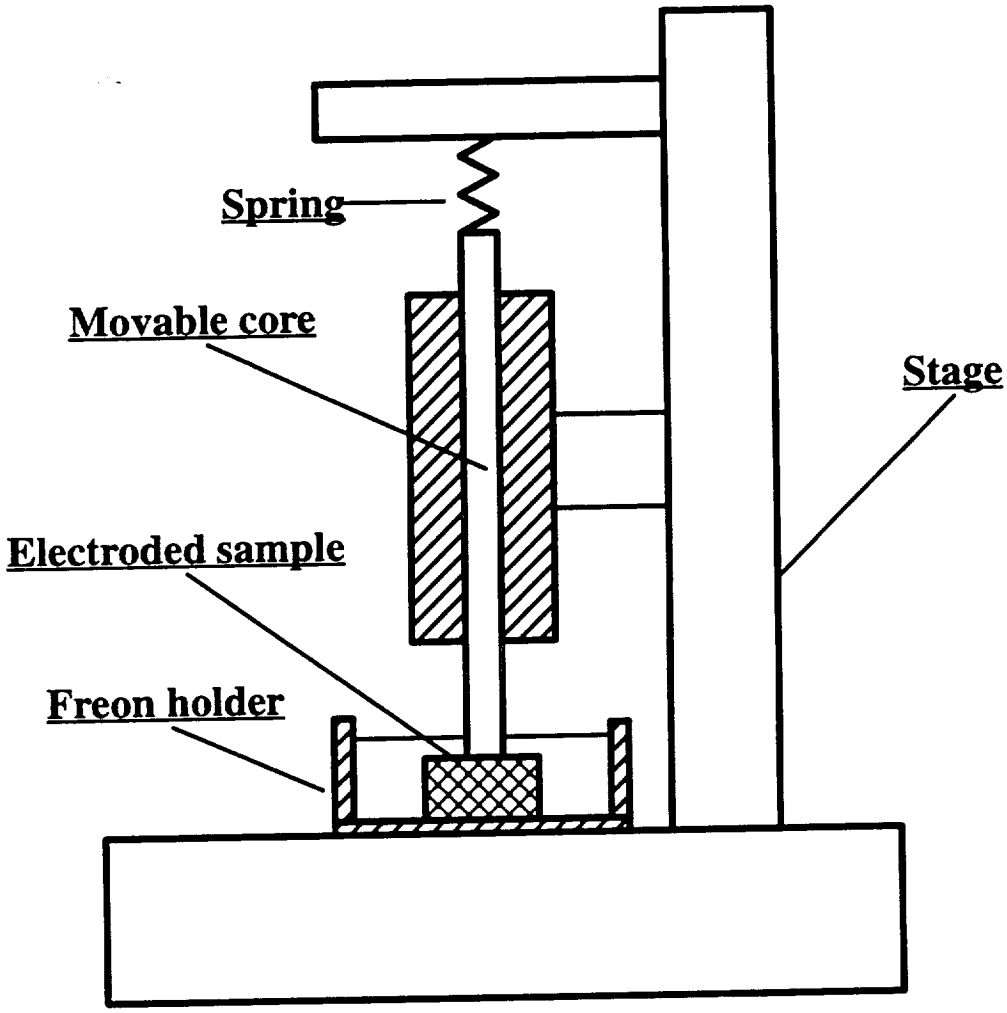

Figure 3. Device for measurement of electric field induced strains.

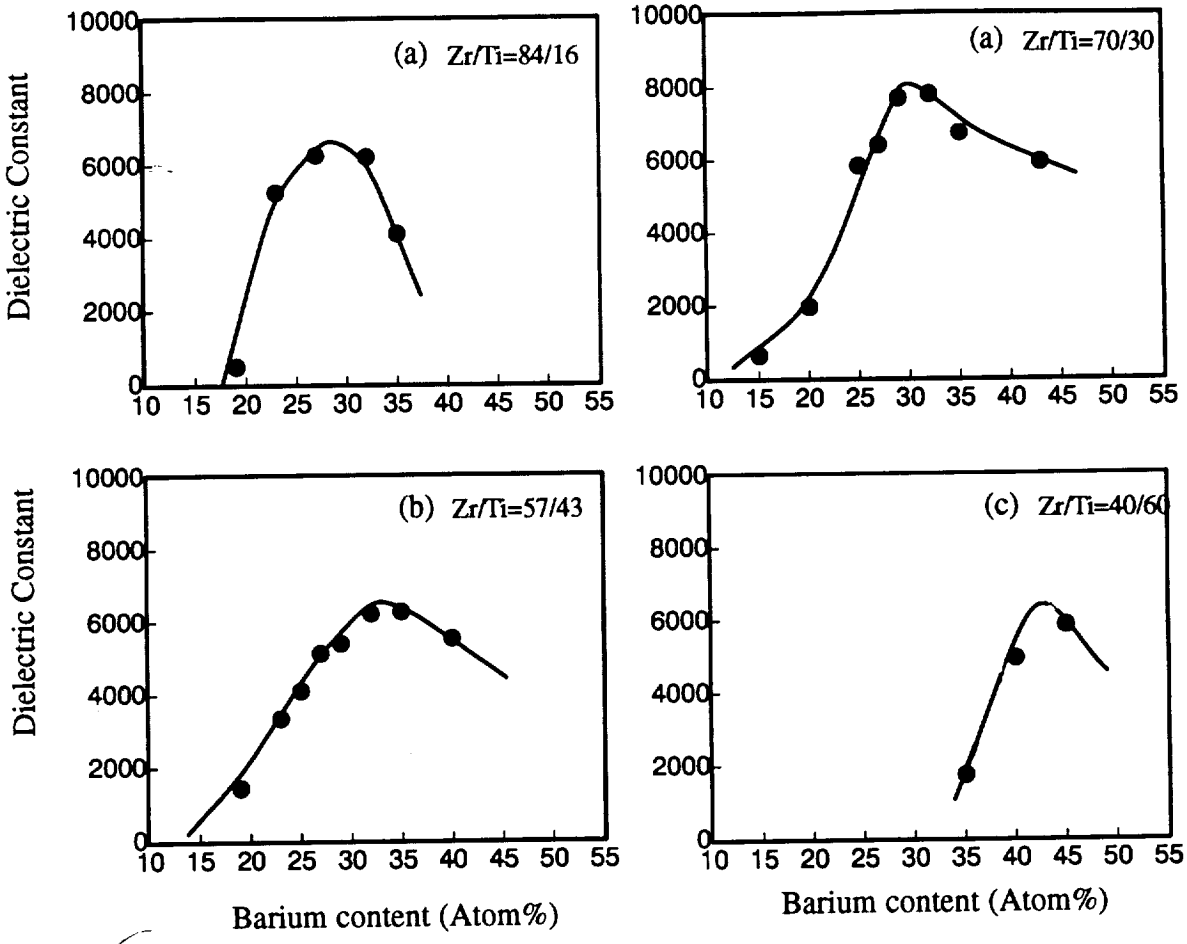

Figure 4. Variation of dielectric constant with barium content at constant Zr/Ti ratios.

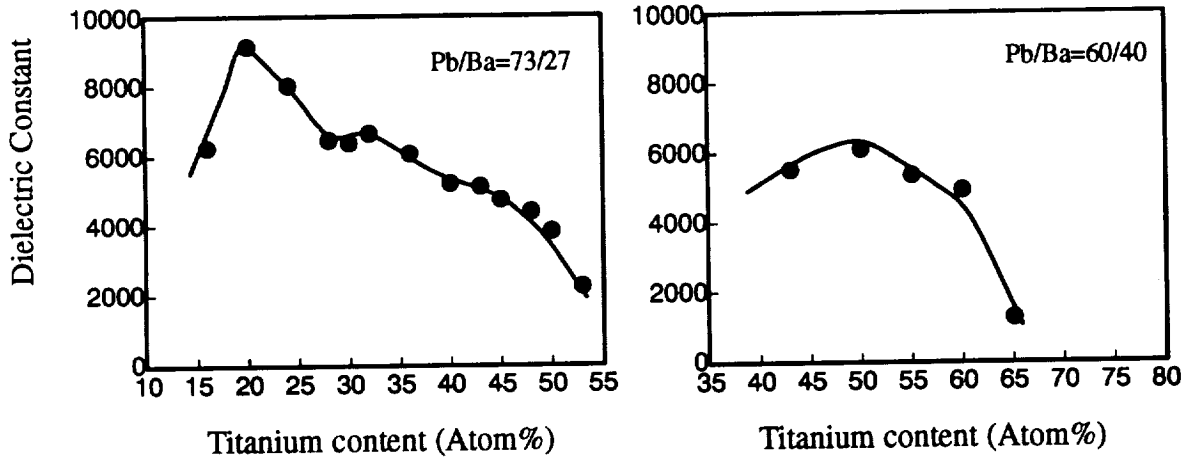

Figure 5. Variation of dielectric constant with titanium content at constant Pb/Ba ratios.

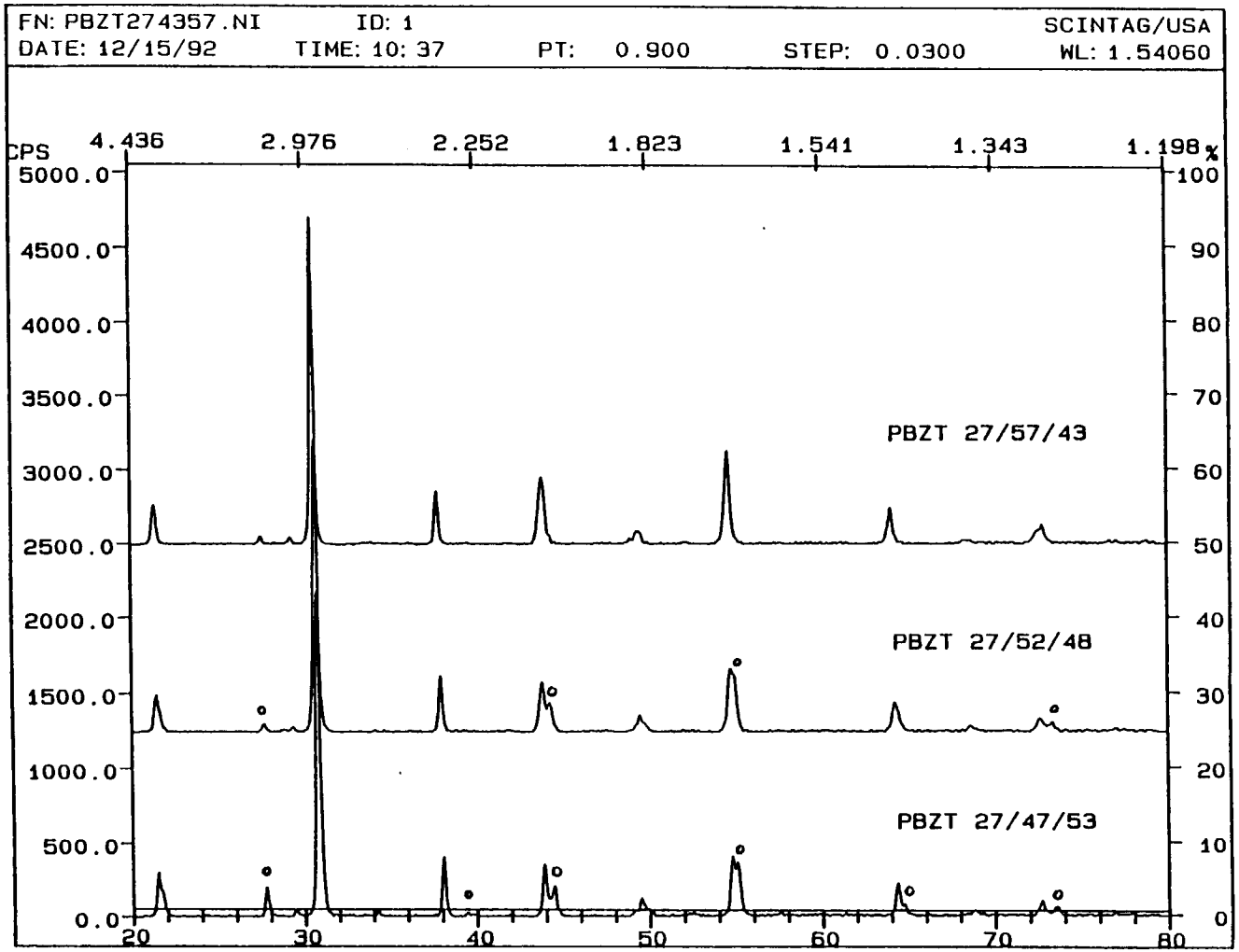

Figure 6. X-ray diffraction pattern of PBZT ceramics with Pb/Ba=73/27. o indicates the characteristic peaks of the tetragonal phase.

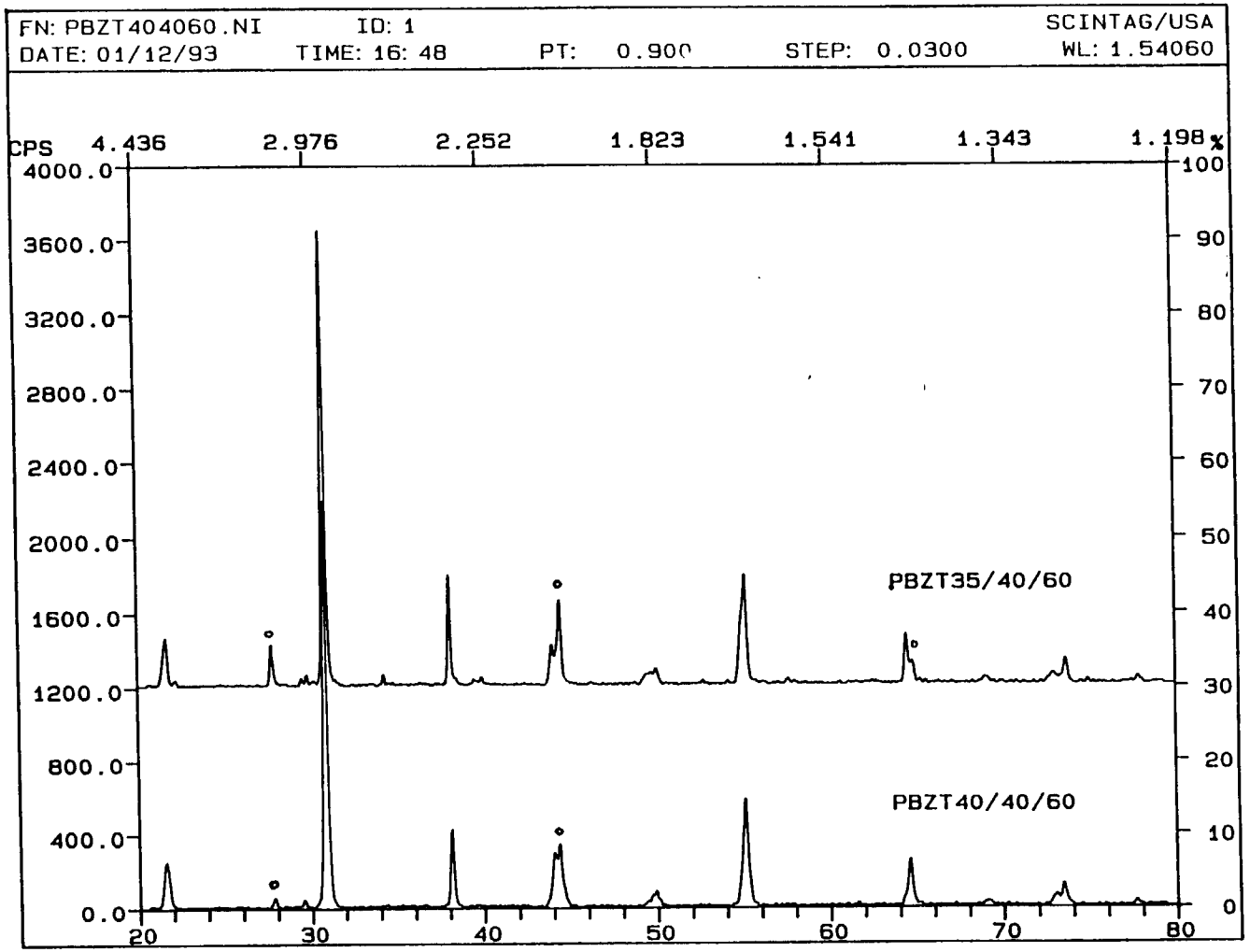

Figure 7. X-ray diffraction pattern of PBZT ceramics with Zr/Ti=40/60. o indicates the characteristic peaks of rhombohedral phase.

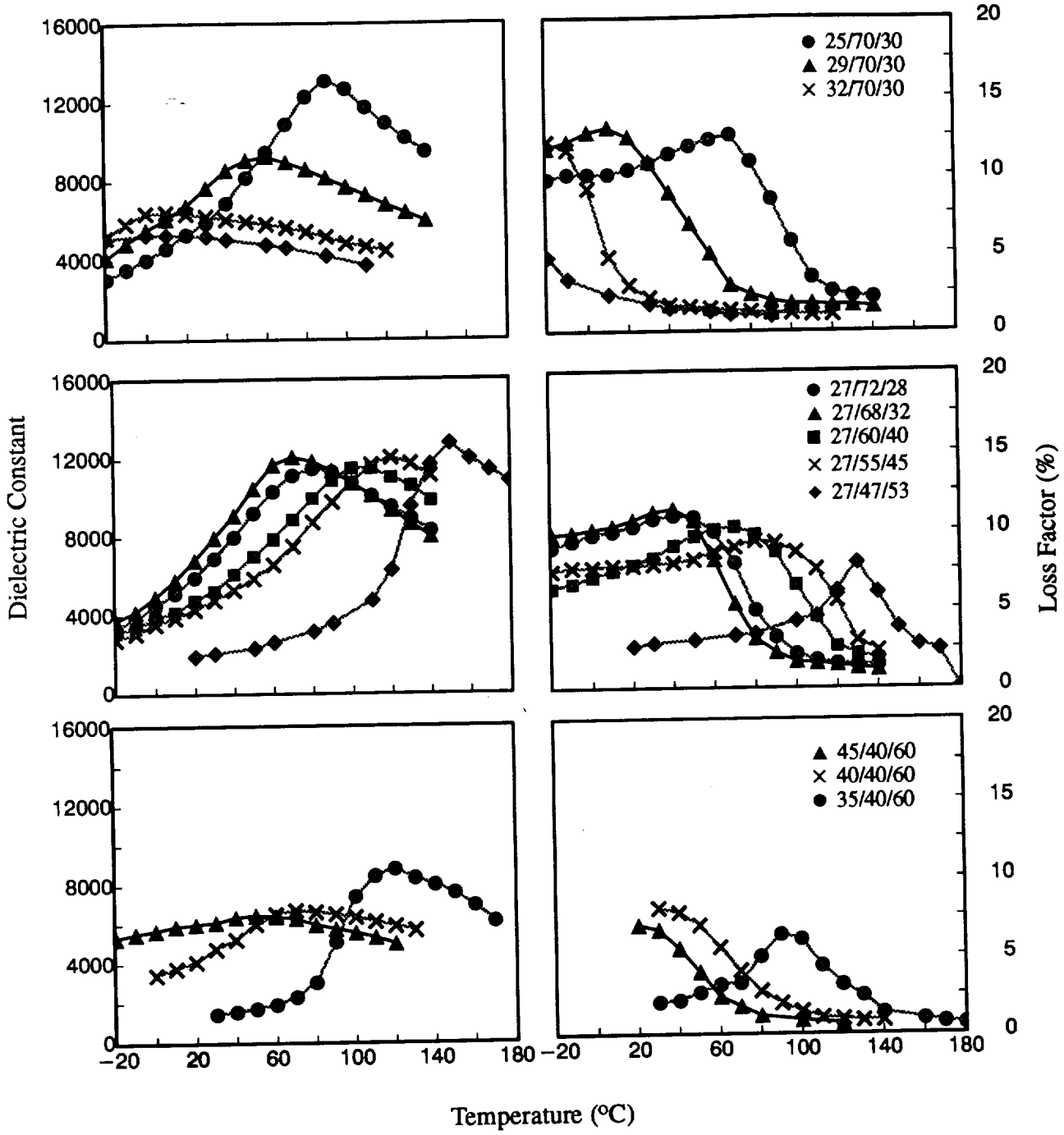

Figure 8. Temperature dependence of dielectric constant and loss factor for the PBZT compositions with constant Zr/Ti ratios (top and bottom) and with constant Pb/Ba ratio (middle).

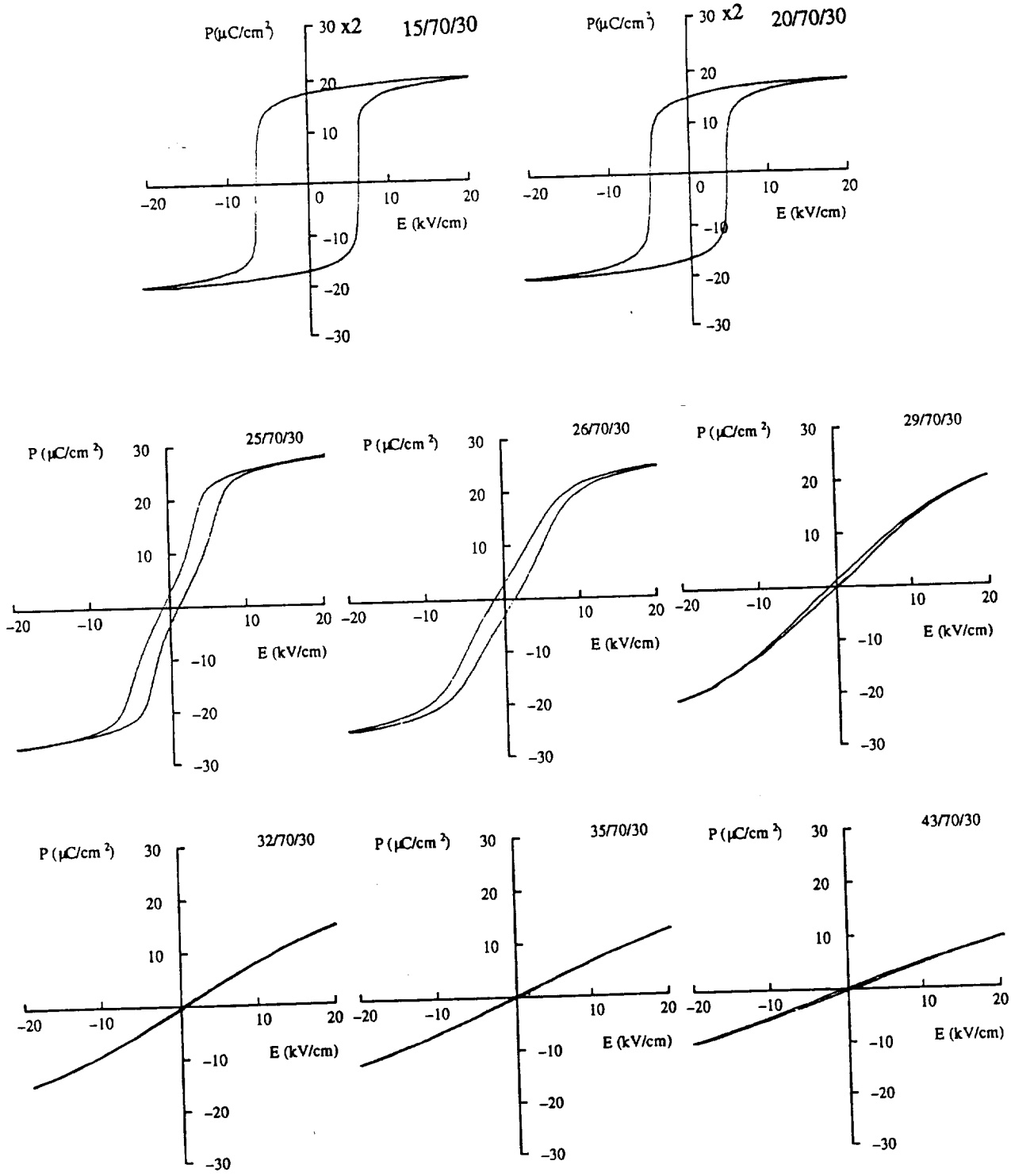

Figure 9. Relationship between polarization and electric field for the PBZT ceramics with Zr/Ti=70/30.

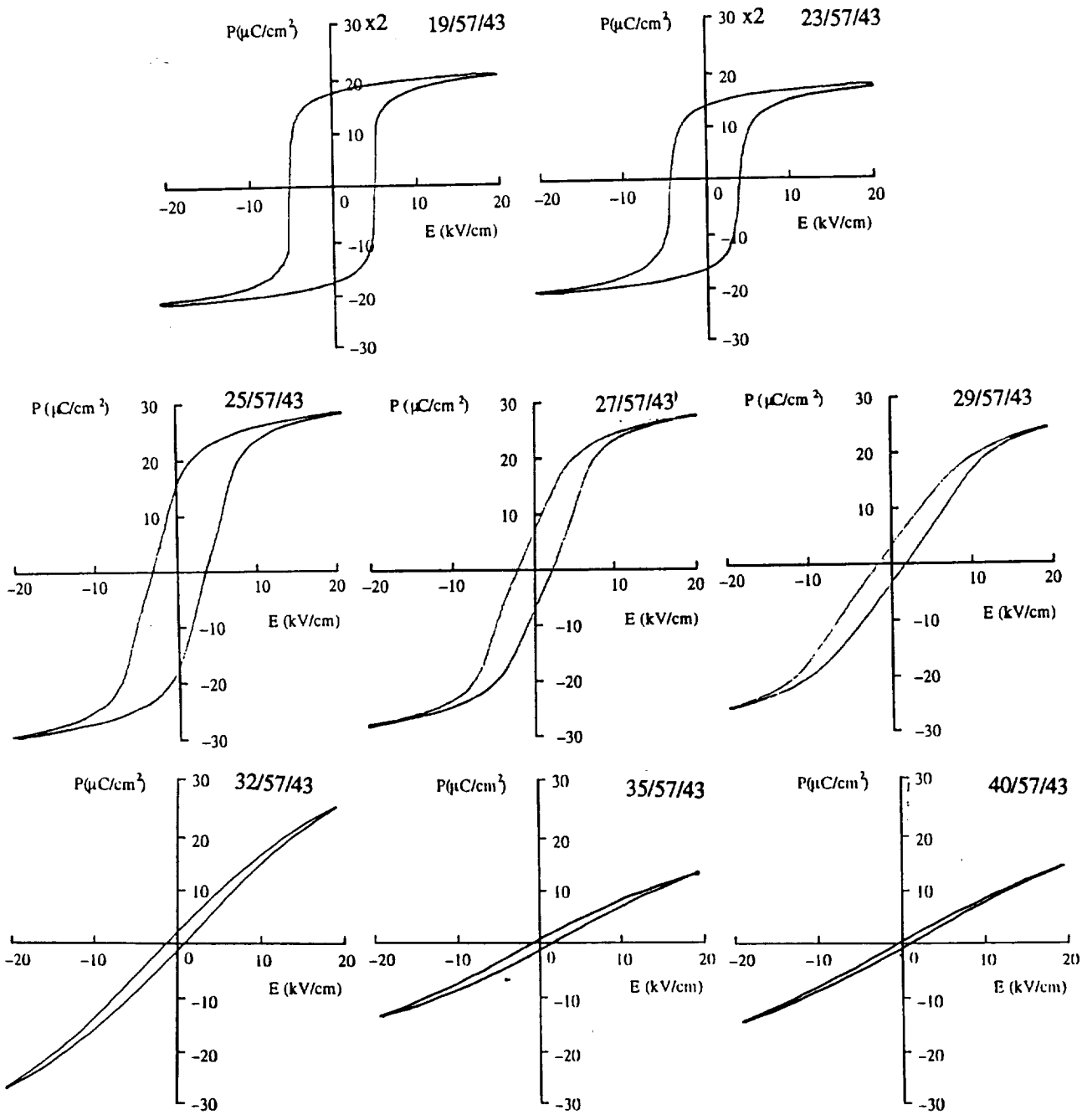

Figure 10. Relationship between polarization and electric field for the PBZT ceramics with Zr/Ti=57/43.

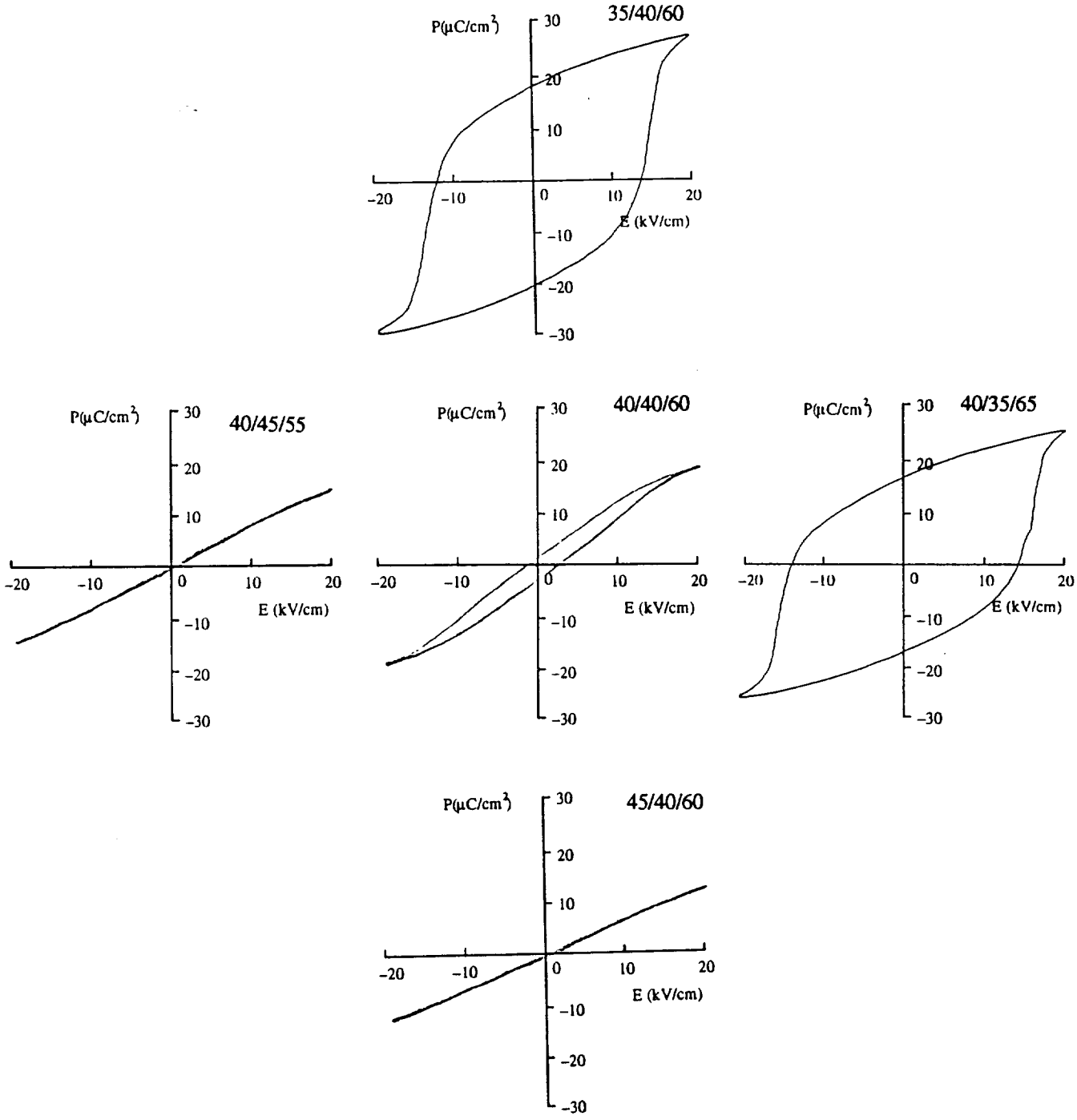

Figure 11. Relationship between polarization and electric field for the PBZT ceramics with Zr/Ti=40/60 and Pb/Ba=60/40.

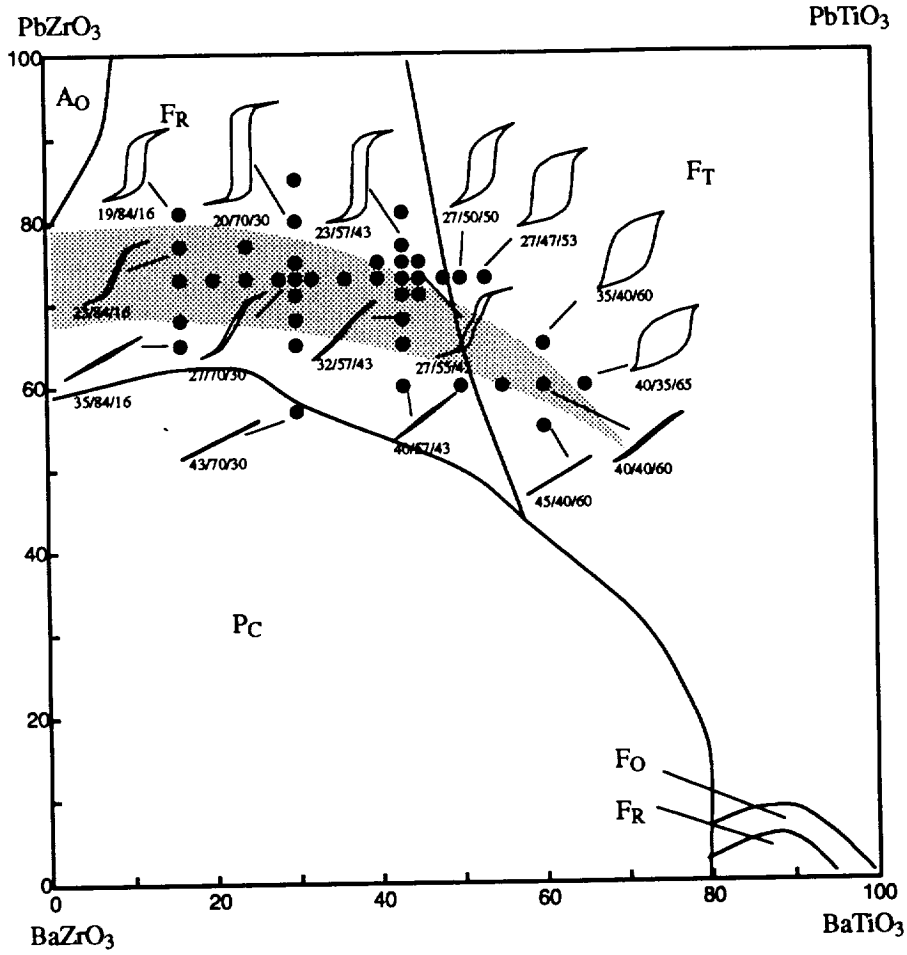

Figure 12. P–E relationship with corresponding composition in the room temperature phase diagram of the PBZT system. Shadowed area represents relaxor phase region.

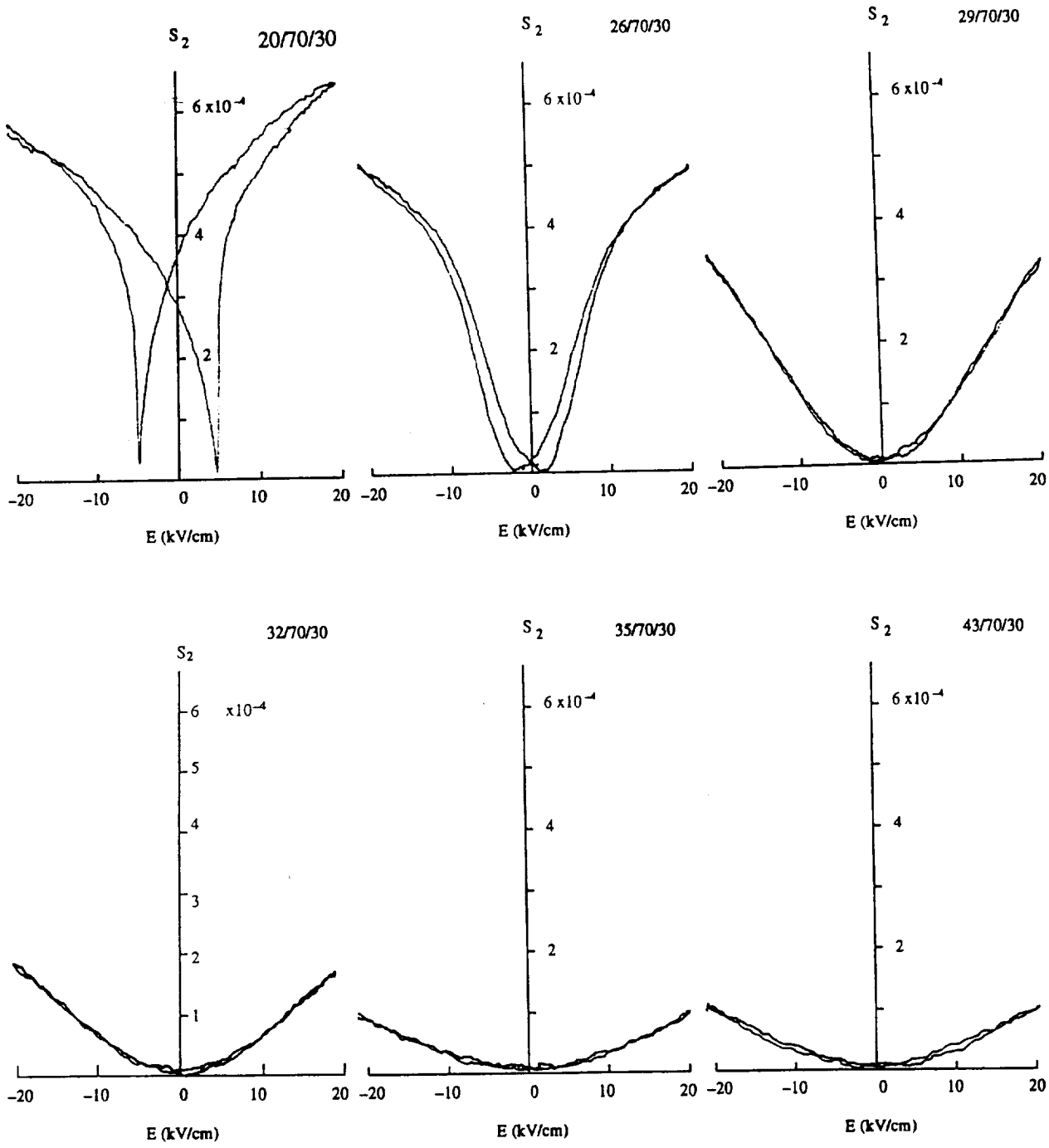

Figure 13. Variation of lateral strain with electric field for the PBZT ceramics with Zr/Ti=70/30.

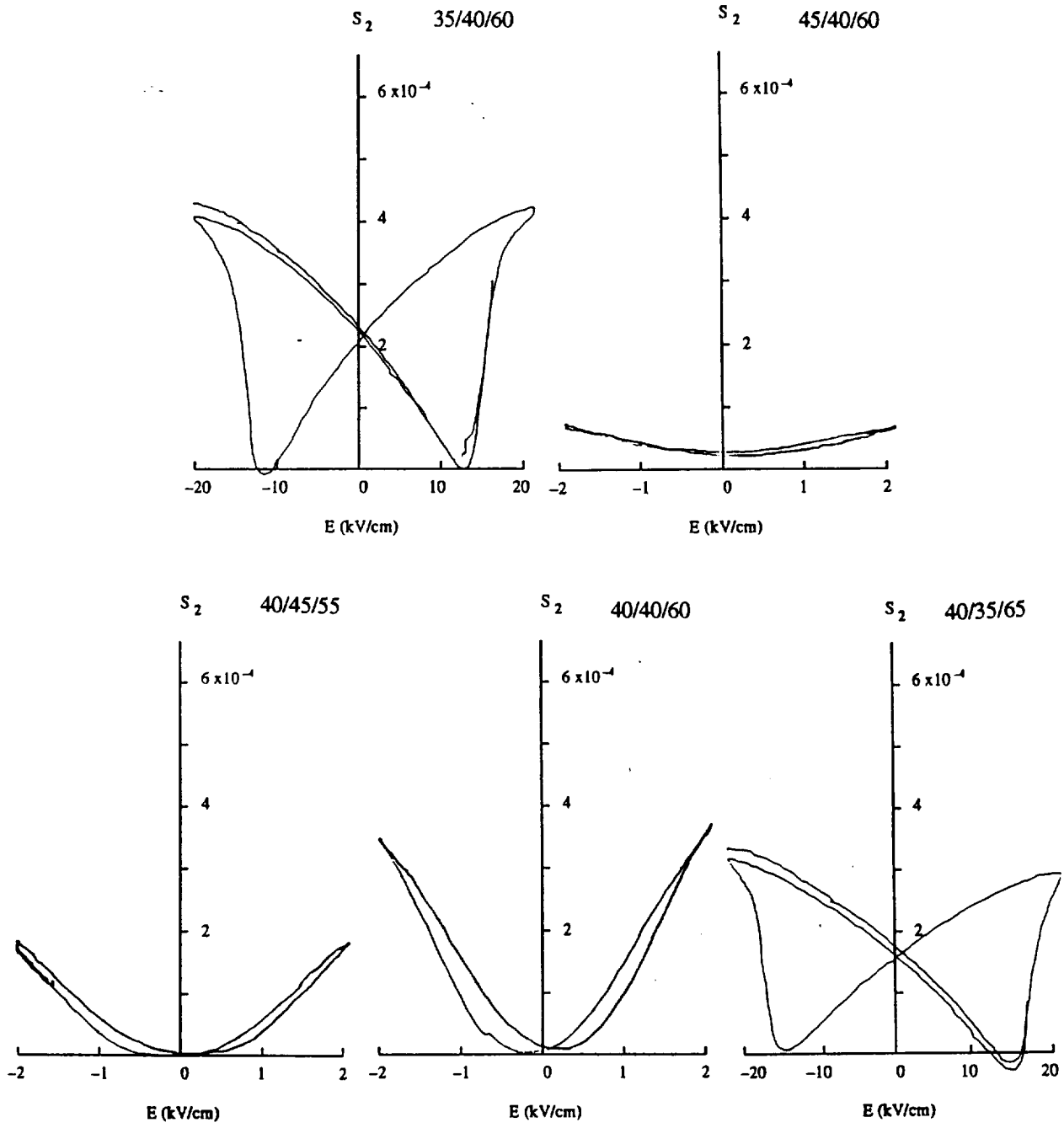

Figure 14. Variation of lateral strain with electric field for the PBZT ceramics with Zr/Ti=40/60 and Pb/Ba=60/40.

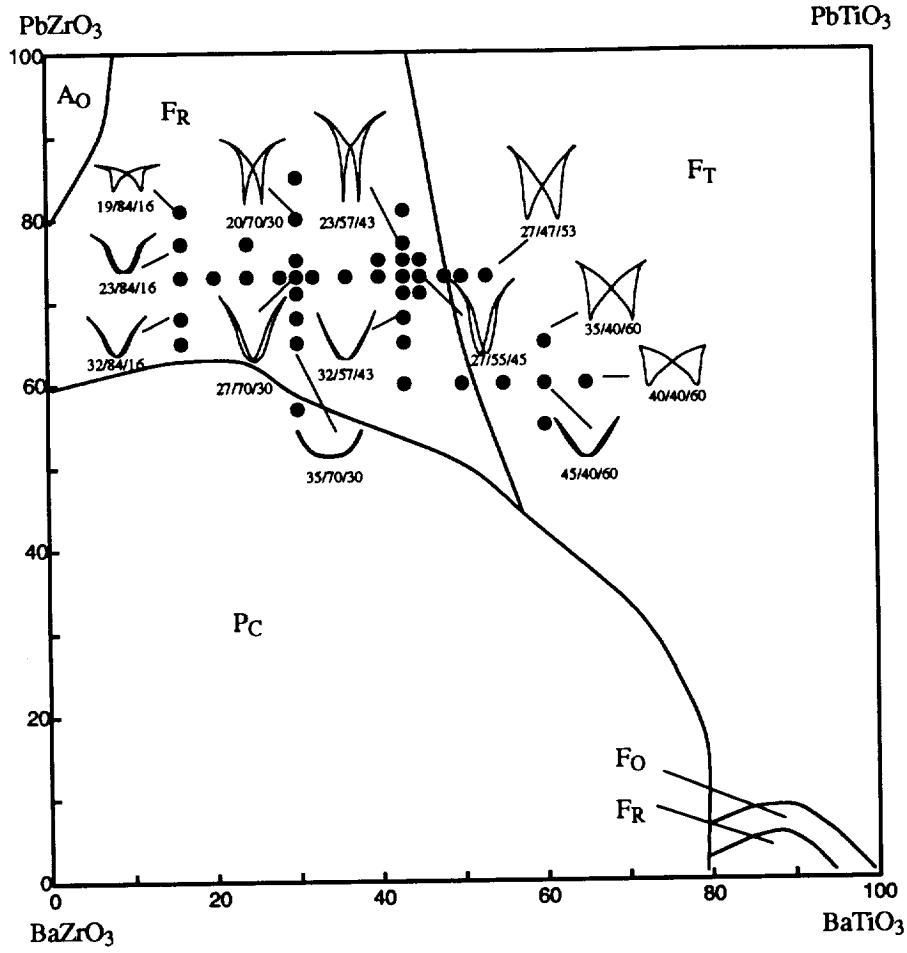

Figure 15. S–E relationship with corresponding composition in the room temperature phase diagram of the PBZT system.

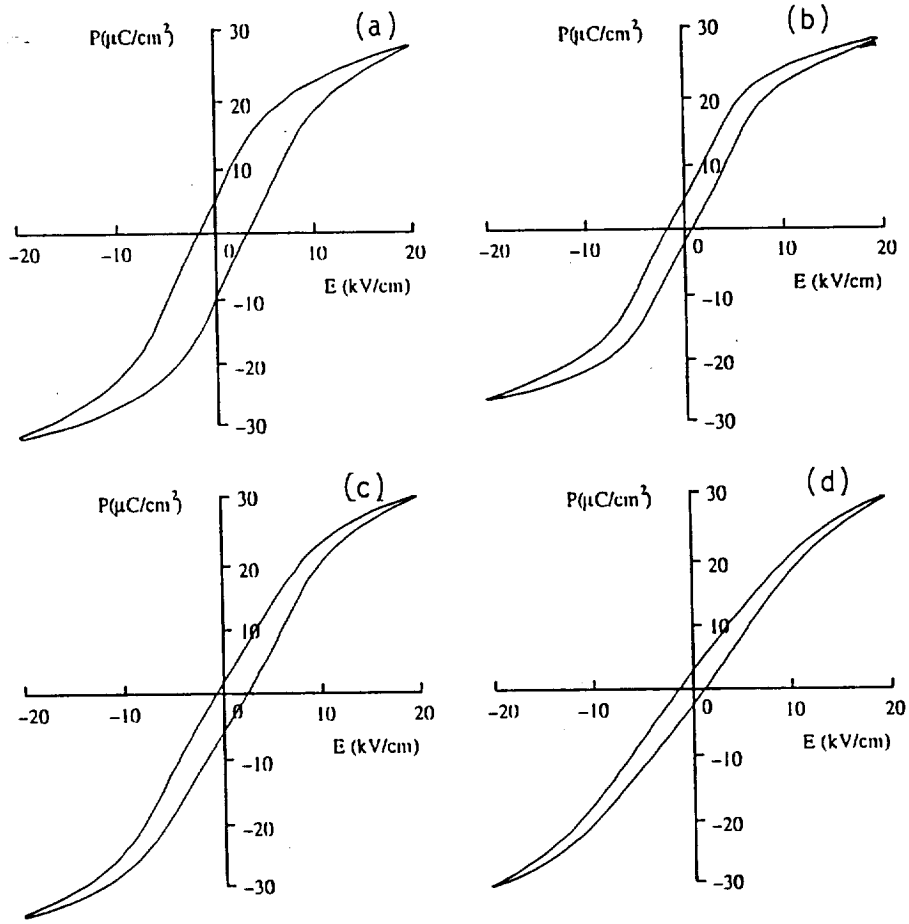

Figure 16. Influence of addictive Bi_2O_3 on the P–E relationship of PBZT 27/70/30; (a) 0 Atom% Bi_2O_3, (b) 1 Atom%, (c) 2 Atom% and (d) 3 Atom% Bi_2O_3.

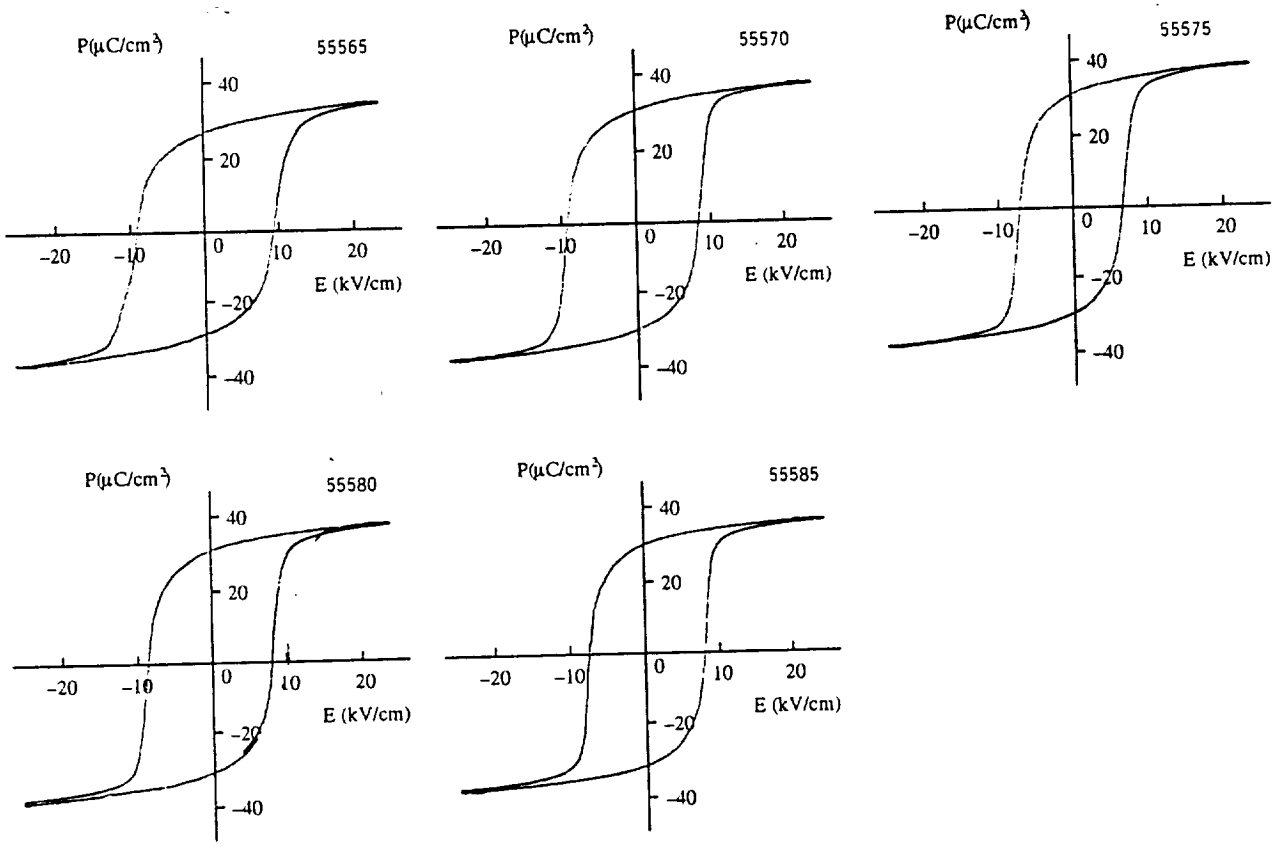

Figure 17. Relationship between polarization and electric field for the PLZT ceramics with La=5.5 Atom%.

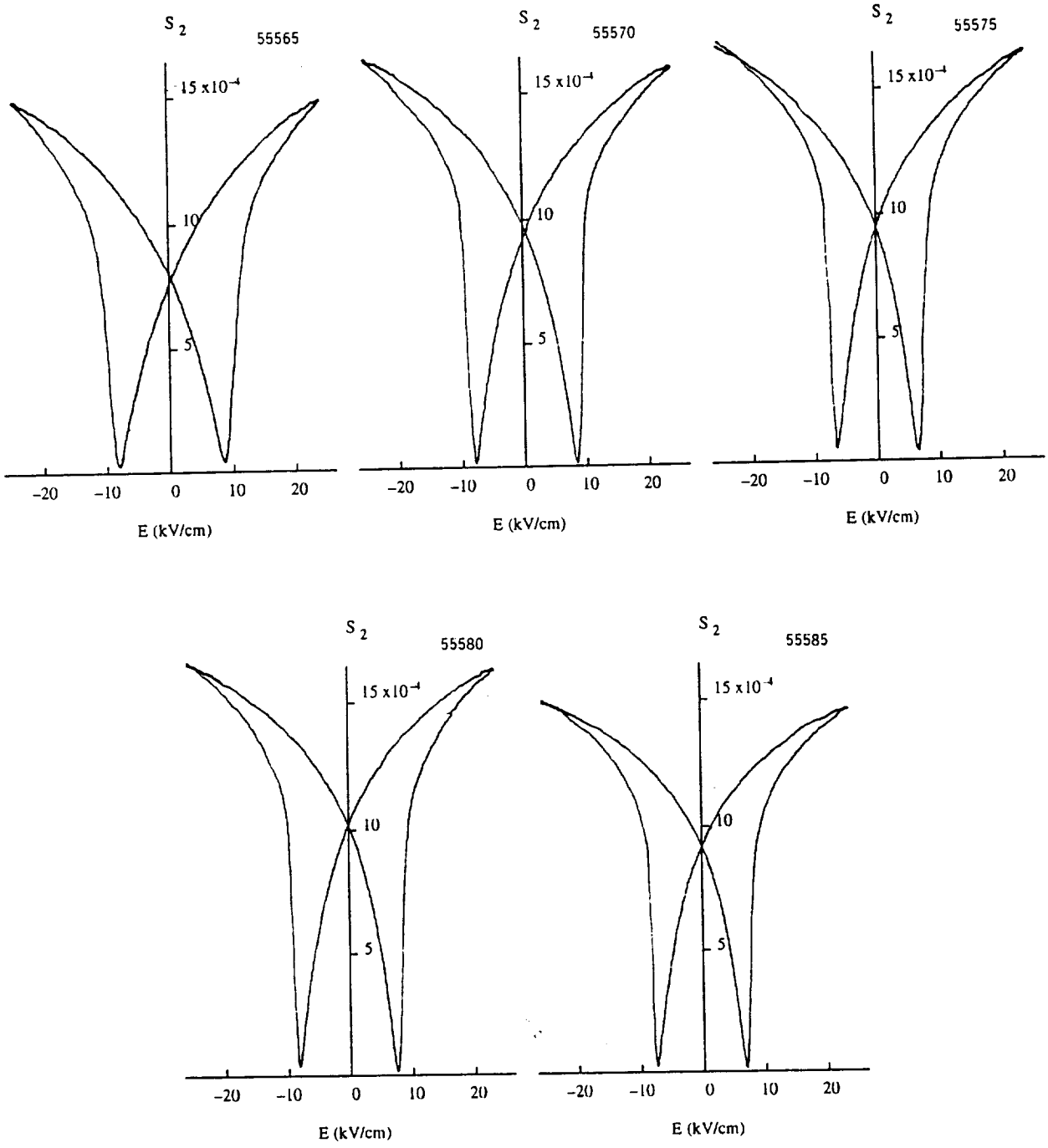

Figure 18. Variation of lateral strain with electric field for the PLZT ceramics with La=5.5 Atom%.

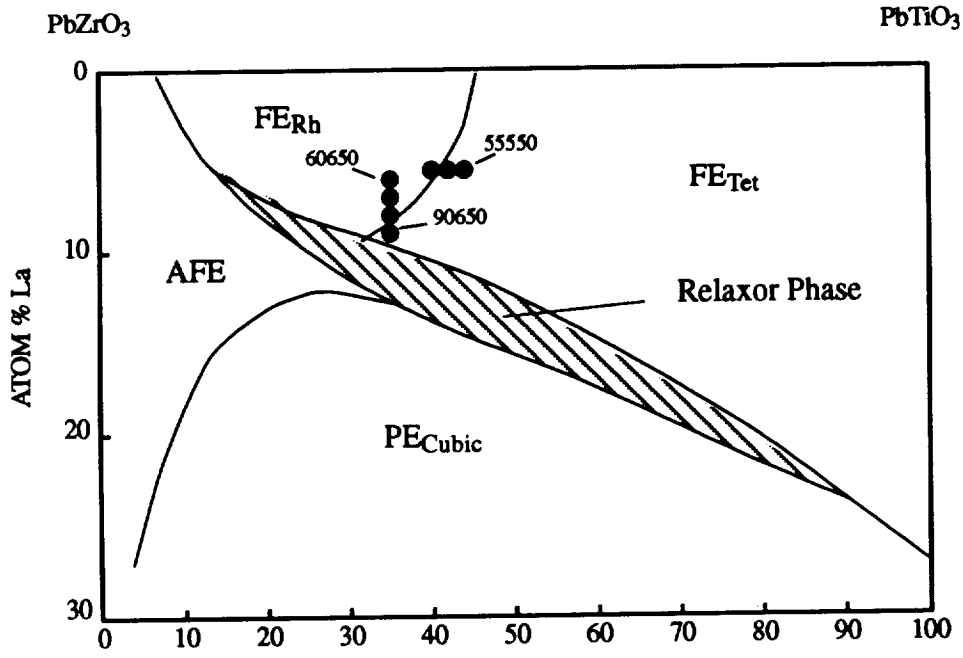

Figure 19. Room–temperature phase diagram of PLZT system [3].

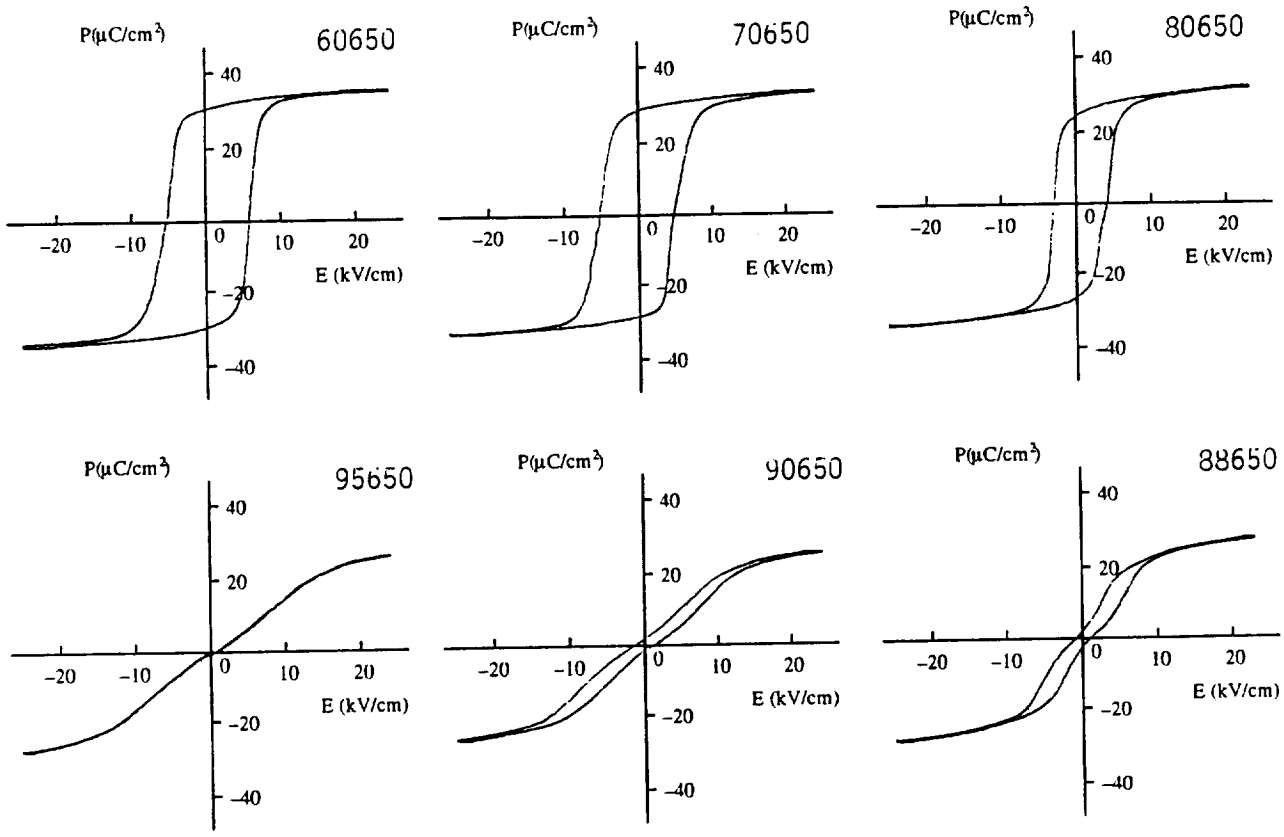

Figure 20. Relationship between polarization and electric field for the PLZT ceramics with Zr/Ti=65/35.

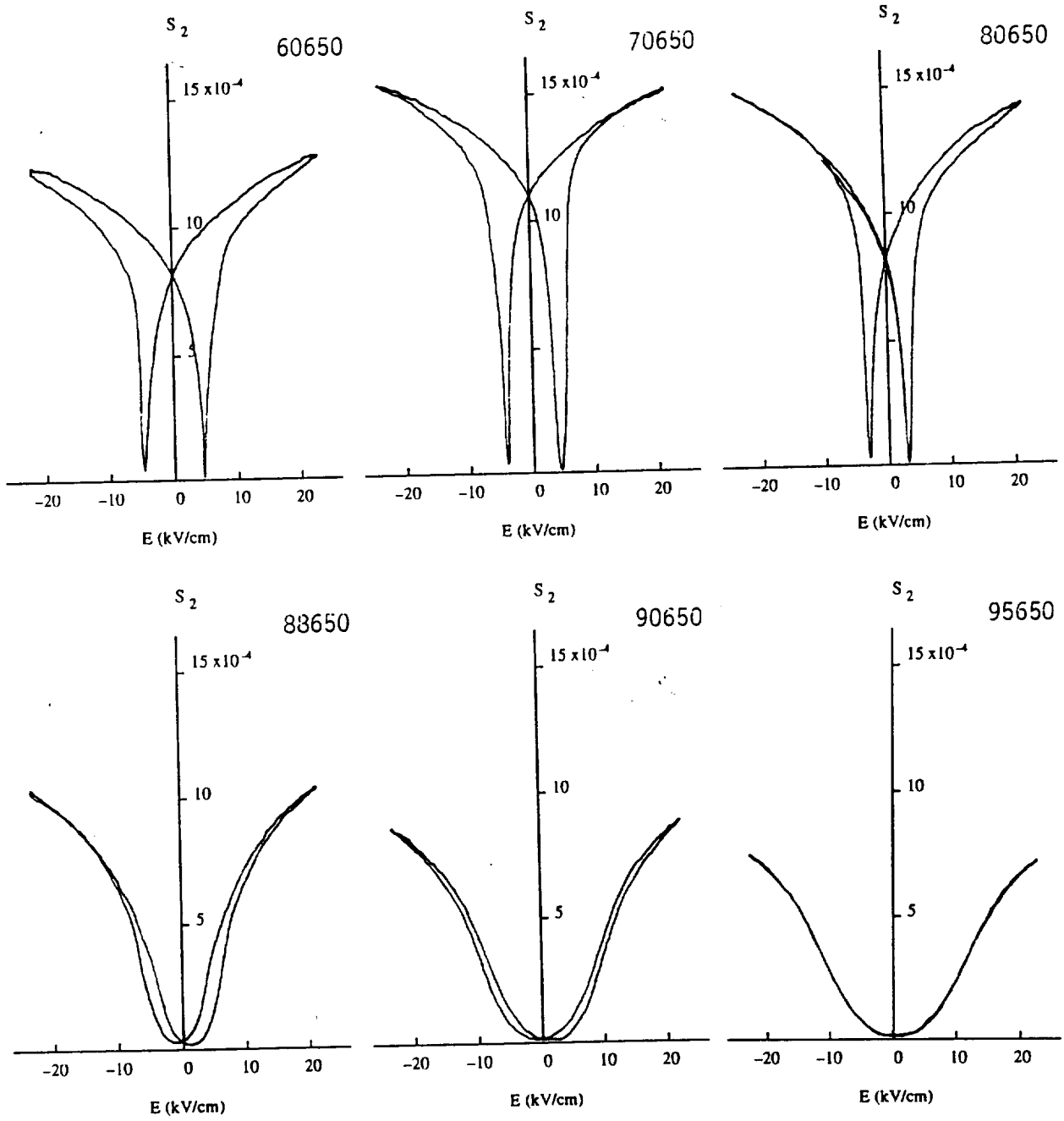

Figure 21. Variation of lateral strain with electric field for the PLZT ceramics with with Zr/Ti=65/35.

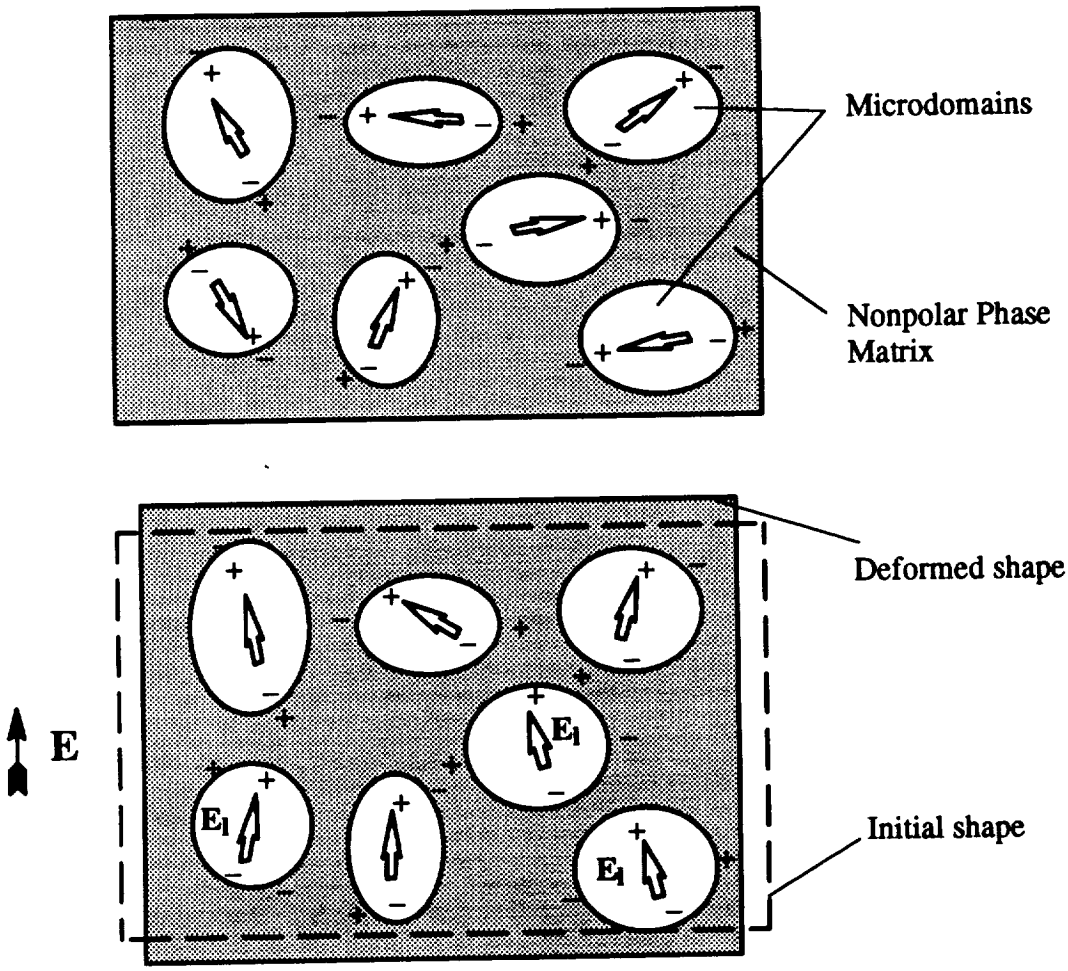

Figure 22. Microdomain rotation under external and local electric fields.

Part III.

Semi-annual Report

SUPERCONDUCTIVITY DEVICES: COMMERCIAL USE OF SPACE

Characterization of the Rainbow Devices

to

National Aeronautical and Space Administration
Langley Research Center
Hampton, VA 23665-5226

Principal Investigator:
Gene Haertling -Clemson University
Co-Investigator:
Eugene Furman -Clemson University

Contract No. NAG-1-1301 March, 1993

Characterization of the RAINBOW Devices

I. Introduction

This report summarizes the recent progress in the characterization of RAINBOW (Reduced And Internally Biased Oxide Wafer) devices.

There is considerable interest at the present time to develop materials and devices capable of producing displacements above those achieved with the monolithic ferroelectric materials and transducers. A partial list of applications where such materials can be used includes micropumps, portable speakers, ultrasonic cleaners, and micropositioners.

The RAINBOW technology represents a novel approach for producing devices capable of large displacement. A RAINBOW device is obtained as a result of the partial reduction of a sintered ceramic which was initially fired in an oxidizing atmosphere resulting in a composite consisting of oxidized/reduced layers with a 2-2 connectivity[1]. Because of the decrease in volume during the reduction and its higher coefficient of thermal expansion, the reduced layer is in tension and the remaining oxide layer is in compression at room temperature. To reduce interfacial stress, the samples develop curvature.

In its mode of operation, a RAINBOW device is similar to the piezoelectric unimorph, which consists of a metal layer bonded to a piezoelectric ceramic[2]. In the unimorph, activation of the piezoelectric element with voltage, results in a deflection of the metal/ceramic composite. In comparison to the unimorph, in which the layers are bonded near room temperature, RAINBOW devices are characterized by a significantly higher level of internal stress.

In principle, any piezoelectric, ferroelectric, or electrostrictive materials with high electrical conductivity in a reduced state and low conductivity in the oxidized state can be considered for a RAINBOW device.

II. RAINBOW Characterization

Lead lanthanum zirconate titanate (PLZT) materials were found to be reducible in carbon-rich atmosphere[3,4]. As a result of a partial reduction of the PLZT samples, the structure shown in Figure 1 is obtained. The reduced PLZT layer is highly conducting and can be used as one of the electrodes. Thermosetting silver epoxy electrodes are applied to the reduced and oxidized layers. Measurements of the dielectric loss (tan δ) indicate that the oxide layer of the RAINBOW device retains its insulating properties since the observed losses are comparable to those seen in the bulk PLZT ceramics. The dielectric data is summarized in Table 1.

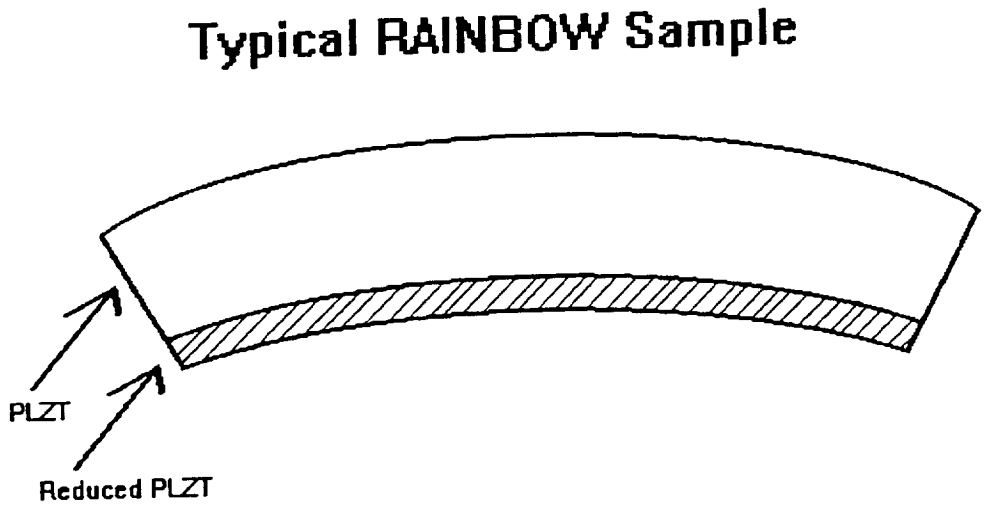

Figure 1. Sample structure.

Table 1. Dielectric data for RAINBOW devices

Composition	Frequency	Capacitance	Dielectric Loss
La/Zr/Ti temp.(°C)/time(min.)	Hz	nF	tan δ
5.5/56/44	120	13.53	0.035
	1000	13.03	0.025
6.0/59.5/40.5 975/90 (#1328)	120	8.02	0.021
	1000	7.74	0.017
6/59.5/40.5 975/60	120	20.0	0.028
	1000	19.4	0.026
6/59.5/40.5 975/105	120	10.15	0.036
	1000	9.57	0.088
9.5/65/35 975/60	120	21.1	0.179
	1000	31.9	0.607

Larger than expected dielectric losses were observed only in the sample with the composition of 9.5/65/35. Since the loss measurements on this sample were performed after considerable field testing, which may have permanently degraded this sample, it will be necessary to repeat this measurement with a virgin sample.

Scanning electron microscopy was used to characterize interfaces between the reduced layer and oxide layer. The results are shown in Figure 2. The reduced layer extends approximately 100 microns into these samples. The interfaces have good mechanical integrity - no cracks were observed in the vicinity of the interfaces. The width

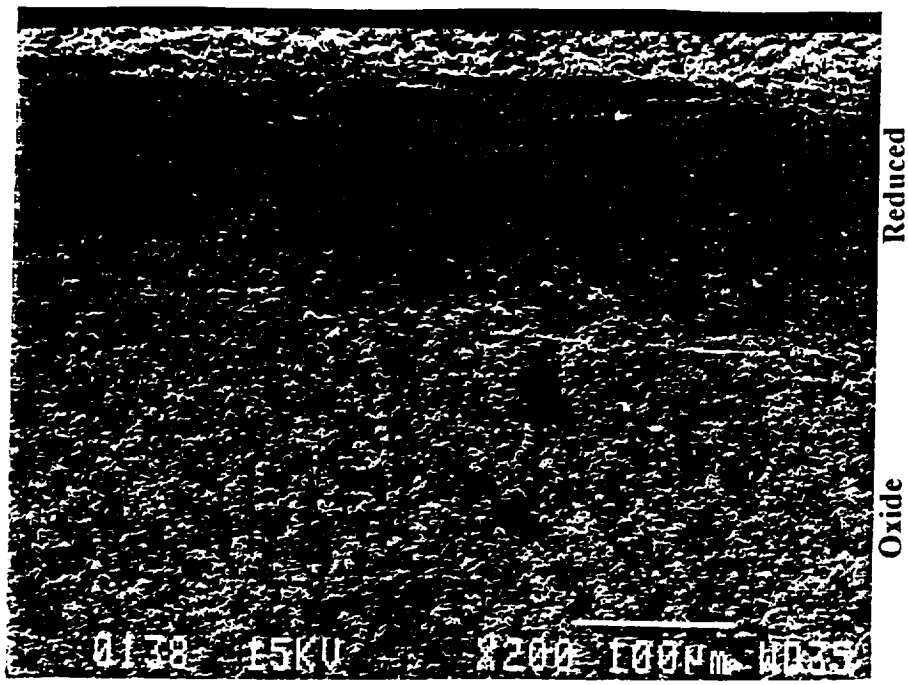

PLZT 7.9/70/30

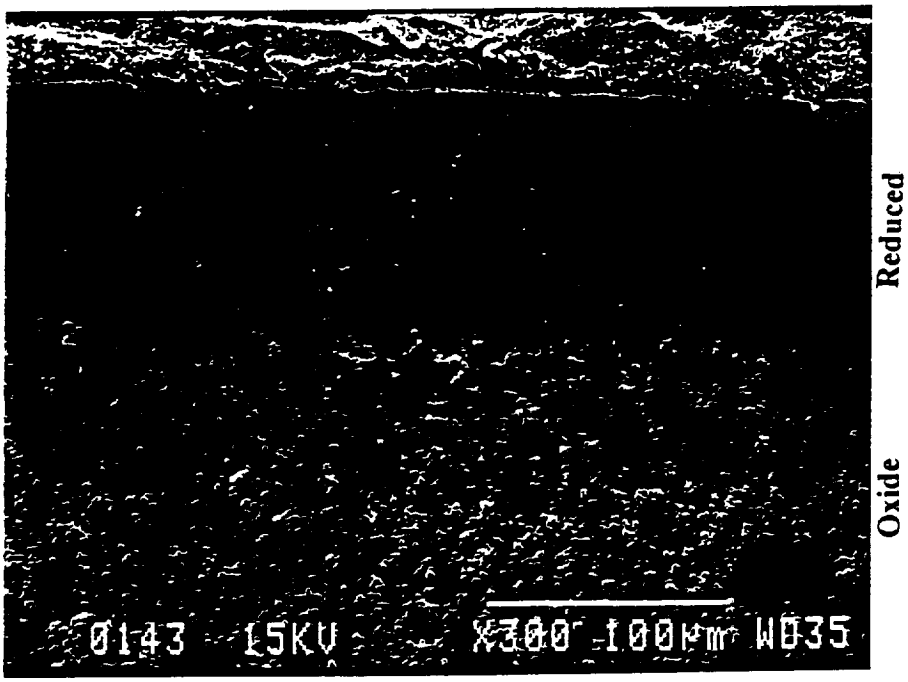

PLZT 8.6/65/35

Figure 2. Cross sections of the RAINBOW devices

of the reduced layer can be controlled by the duration and the temperature of the reduction cycle.

The experimental setup for studying strain as a function of the applied electrical field was constructed and tested. Figure 3 shows the schematic diagram of the equipment. The waveform generator capable of producing sinusoidal, square, and triangular waveforms is connected to the amplifier. The amplifier is rated at ±500 V, 2000 Hz, and 80 mA. In addition, it permits the application of a DC bias voltage to be added to the amplified signal. A probe positioned on the top

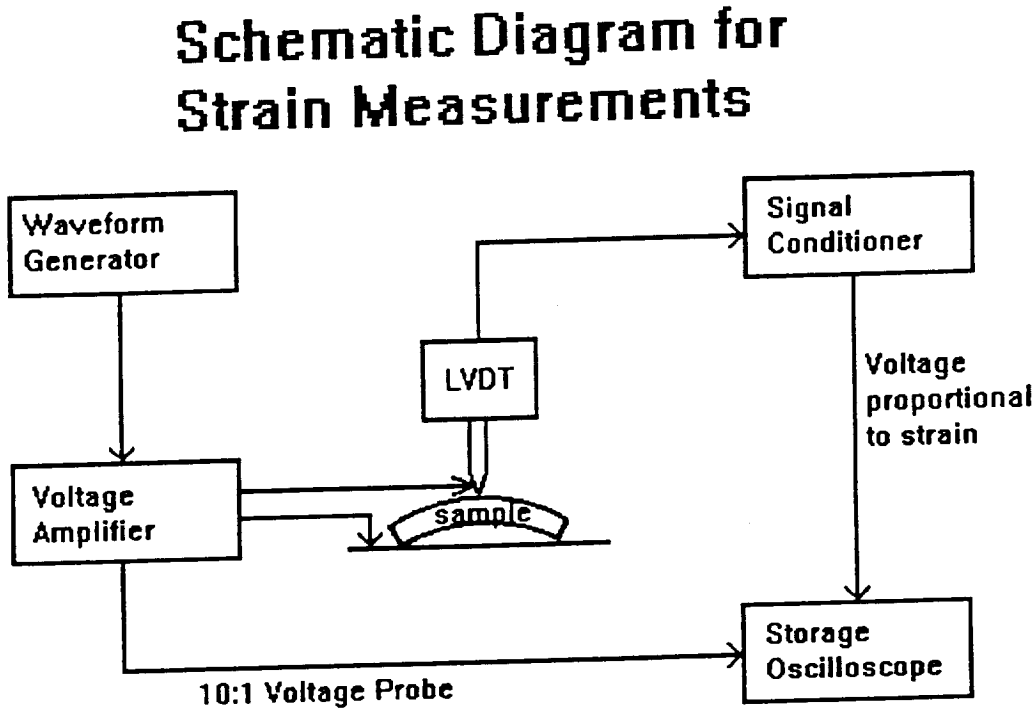

Figure 3. Schematic diagram of the experimental setup

electrode serves a dual purpose: it connects the top electrode to the amplifier and functions as a magnetic core for the linear variable differential transformer (LVDT). The LVDT produces a voltage which is proportional to the displacement of the sample. A signal conditioner attached to the LVDT converts the AC signal to DC, and this signal is then stored in the storage oscilloscope. Voltage applied to the sample is also stored in the oscilloscope, and the data is presented in both time domain and X-Y domain. This setup is used to study the large-signal, low-frequency displacement characteristics of the RAINBOW devices.

Samples characterized by electrostrictive or piezoelectric responses were investigated. Piezoelectricity is observed in PLZT samples with a maximum in the dielectric constant at high temperatures. For the materials with a maximum in the dielectric constant near room temperature, electrostrictive response is observed. Since the addition of lanthanum to PZT reduces the transition temperature, compositions with higher lanthanum content are more likely to exhibit electrostrictive response at room temperature.

An example of a RAINBOW device with the electrostrictive response at low frequency (1.22 Hz) is shown in Figure 4. This figure contains two parts. In the upper portion of the plot, time dependence of the applied voltage and the induced displacement are shown. In the lower portion of the plot, the displacement is shown on the vertical axis as a function of the applied voltage. Inspection of the top portion of the figure indicates that the frequency of the displacement is double that of the applied voltage. This is consistent with the electrostrictive response, in which the strain is proportional to the square of the electric field. The maximum span of the displacement is 21.9 microns, corresponding to the maximum voltage span of 254 V. The figure shows that the displacement of the sample is primarily downward. This is in agreement with the previously determined negative value of Q_{12} for PLZT ceramics. A negative Q_{12} implies a contraction of the oxide layer which is parallel to the interface with the reduced layer when voltage is applied. This contraction reduces the compressive stress in the PLZT at the interface, permitting a new equilibrium state for the RAINBOW device with a lower curvature. A reduction in the curvature of the RAINBOW device is accompanied by the downward motion of the sample.

The asymmetry of the strain for the two polarities should be noted. It is likely that the asymmetry is rooted in the nature of the reduced layer. This layer acts as an electrode.

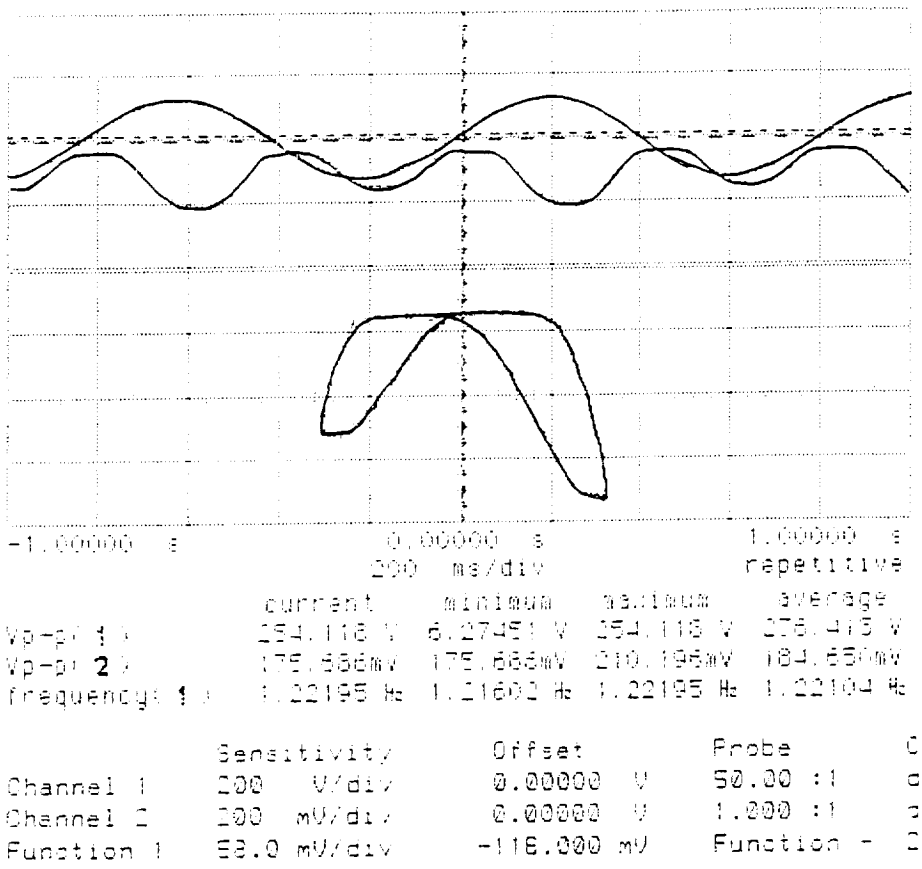

Figure 4. Electrostrictive response of the RAINBOW device based on composition 9.5/65/35

Little is known at this time about the conductivity of the reduced layer near its interface with the oxide layer. If the amount of the metallic lead is below its percolation threshold, conduction through the ceramic particles in the reduced layers is important. In particular, the depolarization field in PLZT may depend on the type of conduction (p-type or n-type) of the ceramic particles in the reduced layer[5].

A typical low-frequency response for a RAINBOW device, based on the piezoelectric composition, is shown in Figure 5. Low frequency implies operation significantly below the lowest resonance frequency of the device. A well-defined hysteresis loop, characteristic of the piezoelectric response, can be seen at the bottom of the figure. Asymmetry of the displacement response for the two polarities of the applied voltage are seen. The origin of the asymmetry is similar to the one described for the electrostrictive case above.

The strain in the top portion of Figure 5 is shown with respect to the equilibrium position. The equilibrium position is defined as the position of the top surface of the sample with no external voltage applied. Prior to the application of the voltage, the LVDT housing is moved with respect to the needle to read zero volts. From the top portion of the figure it is clear that the resistance of the RAINBOW device with respect to the downward displacement of the sample is smaller than for the upward displacement. A probable explanation is that downward displacement is associated with the reduction of the mechanical energy stored in the sample; the opposite occurs for the upward displacement. The shape of the displacement/electric field curve is consistent with the strain of the RAINBOW device being controlled by the d_{31} coefficient.

For the piezoelectric RAINBOW devices it is useful to determine the level of linearity of the strain response as a function of the applied voltage. In Figure 6 peak-to-peak strain in PLZT 6.0/59.5/40.5 is plotted as a function of the applied peak-to-peak voltage (twice the amplitude of the sinusoidal voltage). It can be observed that a roughly linear response exists for a wide range of voltages studied. Thus RAINBOW devices should be considered for the "dial-a-strain" devices.

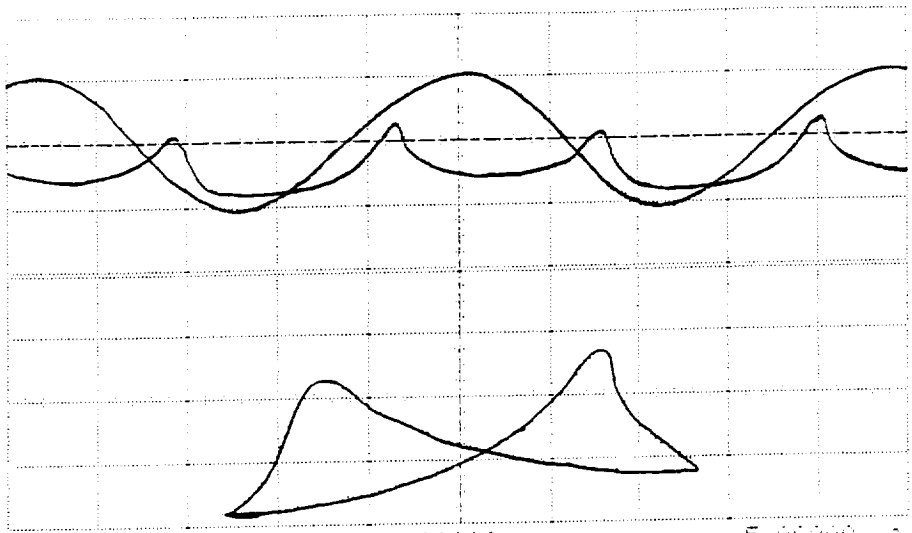

Figure 5. Piezoelectric response of the RAINBOW device based on composition 6.0/59.5/40.5

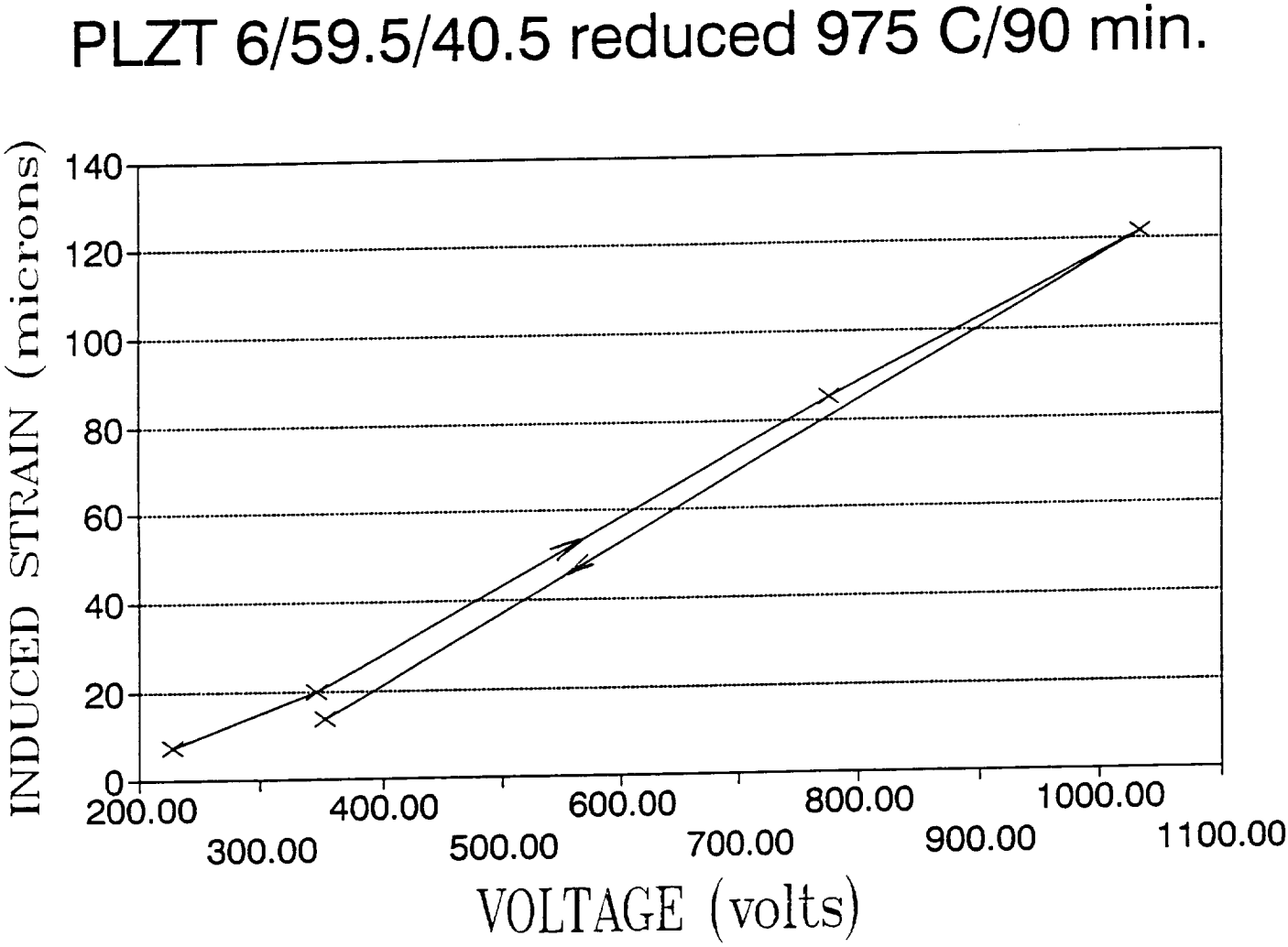

Figure 6. Peak-to-peak strain as a function of peak-to-peak voltage

III. Conclusions

The feasibility in obtaining large displacements with the RAINBOW devices has been shown. Large strains were obtained with electrostrictive and piezoelectric devices. RAINBOW devices act as mechanical analogs of diodes - a mechanical displacement is easier in the downward direction. The explanation for the asymmetric displacement may be found in the interaction between the movement of the RAINBOW device and the energy stored in the mechanical component of the free energy. The downward movement of the RAINBOW device is accompanied by the reduction of the stored mechanical energy; the opposite occurs for the upward movement. The displacement of the RAINBOW device was shown to be controlled by the d_{31} coefficient for the piezoelectric compositions and by the Q_{12} coefficient for the electrostrictive compositions.

IV. Future work

Preliminary work indicates that RAINBOW devices are capable of producing significant displacement, and because of this, they are promising candidates for a number of applications. Continuing work will concentrate in three key areas: characterization, modeling, and optimization.

In the area of characterization strain measurements will be extended to higher frequencies. A miniature spring-loaded LVDT probe will be used for this purpose. It is essential to have the resonance frequency of the probe above the frequency range of the important resonances of the RAINBOW sample. The effect of mass loading on the performance of the RAINBOW device will also be studied. The direct strain measurements by the LVDT will be complemented by electrical impedance measurements which will be useful in characterizing resonant modes.

Measurements of the volume change during the reduction of the PLZT, determination of the thermal expansion coefficients, and elastic constants of the oxide layers and the reduced layers will also be performed. These measurements will be tied in with the modeling work.

In the area of modeling, a finite element analysis of the RAINBOW device will be performed using the ALGOR software package. The initial goals are to be able to predict resonant frequencies as well as low-frequency displacement characteristics of RAINBOW

devices. Modeling should also aid in determining the importance of the internal stress on the performance of a RAINBOW device.

Work in the optimization area will be based on the foundation of characterization and modeling. Figures of merit for different applications of interest will be determined. Once clearly defined goals are set, we can concentrate on optimizing compositions, dimensions, and processing conditions.

V. References

1. R.E. Newnham, D.P. Scinner and L.E. Cross, Mat. Res.Bull. 13, 525 (1978).

2. J.G. Smits and W. Choi, IEEE Trans. Ultrasonics, Ferroel., and Frequency Control 38, 3, 256 (1991).

3. G.H. Haertling and C.E. Land, J. Am. Ceram. Soc. 54, 1 (1971).

4. G.H. Haertling, Proc. 4th Int. SAMPE Electronics Conf. 699 (1990).

5. P. Wurfel and I.P. Batra, Phys. Rev. B8, 5126 (1973).

Part IV.

Semi-Annual Report

SUPERCONDUCTIVITY DEVICES: COMMERCIAL USE OF SPACE

General Studies of Rainbow Processing, Properties and Devices

to

National Aeronautics and Space Administration
Langley Research Center
Hampton, VA 23665-5225

Period: July 3, 1992 - March 31, 1993

Principal Investigator:
Gene Haertling - Clemson University

Contract No. NAG-1-1301 March, 1993

General Studies of Rainbow Processing and Devices

I. Introduction

In the last several years, the technology of using piezoelectric and electrostrictive ceramic materials as solid state actuators for small (<10 microns) and precise mechanical (linear and rotary) movement devices has undergone considerable investigation and development. More recently, it has become evident that these same solid state devices would be desirable in earth-bound and space-related applications requiring larger displacements (100 to several thousand microns) such as pumps, active structures, antivibration components, noise-canceling devices, electrically-controlled compliance elements and smart sensors. Unfortunately, the materials required for these devices are not directly suitable for large displacements; consequently, various techniques of strain amplification must be developed for these applications.

A new processing method which has recently been developed for piezoelectric and electrostrictive devices and which shows considerable promise for meeting some, if not many, of the high strain applications is known as the **RAINBOW** technology. This acronym denotes the basic active structure of the Rainbow device and stands for **R**educed **A**nd **IN**ternally **B**iased **O**xide **W**afer.

During this reporting period a considerable amount of information about the processing, properties and devices possible from the new Rainbow technology has been obtained. Much of it will be included here; however, it should be recognized that some of this information is only preliminary and is subject to further investigation. Many of the graphs of data are self explanatory and will not be described individually in this semi-annual report. They will be covered more thoroughly in the annual report.

II. Description of the Rainbow Technology

In its most basic sense, the Rainbow technology comprises a new processing method that is applied to standard, high lead-containing piezoelectric or electrostrictive ceramic wafers which are transformed by the process into unique, monolithic material structures capable of carrying moderate loads while, at the same time, achieving unusually high linear displacements when activated with an appropriate voltage. Since these materials are ferroelectric, they are multifunctional by nature and are capable of performing both actuator and sensor functions, thus providing simultaneous electromechanical, pyroelectric and/or electrooptic transduction. Typical devices which can be made from these materials are reciprocating pumps, linear actuators, relays, switches, accelerometers, gages, loud speakers, benders, microphones, optical shutters and pyroelectric detectors. Key features of these all-solid state devices are simplicity,

ruggedness, high reliability, high axial strain, fast response, compressive pre-stressing, monolithic construction, mechanical overload protection, ease of fabrication and low cost.

In regard to operation, the Rainbow is similar to a device known in the industry as a unimorph bender. A unimorph is composed of a single piezoelectric element externally bonded to a flexible metal foil which is stimulated into action by the piezoelectric element when activated with an ac or dc voltage and results in an axial buckling or deflection as it opposes the movement of the piezoelectric element. However, unlike the unimorph, the Rainbow device is a monolithic structure with an integral electrode which is fabricated such that it puts an internal compressive stress bias on the piezoelectric or electrostrictive element, thus rendering it more rugged and able to sustain heavier loads than normal. The integral electrode (usually the bottom electrode) consists of a conductive metal (chemically reduced Pb)/oxide structure which is produced by chemically reducing one surface of the wafer.

A summary of the present-day ceramic actuator technologies is presented in Table 1. The first four types presented are direct-mode actuators in that they make direct use of the change is dimensions of the material, when activated, without amplification of the actual displacement. They utilize either the longitudinal extensional or lateral extensional modes and are capable of sustaining high loads under compression. Their primary disadvantage is the small displacement (strain) that they are able to achieve, which is, at best, a few tenths of a percent.

The next group of five actuators are of the indirect-mode type since they achieve strain amplification via external (flextensional devices, Moonie, unimorph, bimorph) or internal (Rainbow) structures. As may be noted, the load bearing capacity generally decreases as the achievable strain increases. Although no exception to this rule, the Rainbow benders can produce strains up to several hundred percent (an order of magnitude better than the bimorph bender) and can sustain loads of at least eight pounds which is, again, an order of magnitude better than the best bimorphs. An illustration of how these various actuator technologies fit into a stress vs. strain diagram is shown in Figure 1.

III. Processing

The processing techniques for producing the Rainbow structure is simply one of heat treating/chemically reducing one surface of a normal piezoelectric or electrostrictive wafer (as obtained from a materials vendor) in a furnace at a given temperature for a given length of time, cooling and then applying appropriate electrodes to the wafer. A more specific step-by-step description is as follows:

1. Fabricate or purchase high density (>95% theoretical), high-lead containing ferroelectric, piezoelectric or electrostrictive material by suitable means such as atmosphere sintering or hot pressing.

2. Chemically reduce one major surface of the material with carbon (graphite), carbon monoxide, hydrogen or other suitable reducing agent at a temperature of approximately 950 - 1000°C for a time ranging from 15 minutes to one hour. Generally the lower temperatures require the longer times. Typical values for reduced layer thickness as a function of time is shown in Figure 2. The reduction process extracts oxygen atoms from the crystalline lattice producing excess electrons which are responsible for the increased electrical conductivity of the reduced material along with the presence of precipitated metallic lead which is finely distributed throughout the reduced layer. The reduction process normally produces resistivities less than one ohm-cm. Reduction of lead zirconate titanate (PZT) or lead lanthanum zirconate titanate (PLZT) has produced electrical resistivities as low as 3.8×10^{-4} ohm-cm. as given in Figure 3.

4. Expose the conductive reduced layer of the wafer (a thin oxide layer usually exists because the lead is reduced and lost from that layer) by mechanical or air abrasion techniques.

5. Electrode the wafer on both surfaces with an appropriate electrode such as air dried silver, epoxy silver, vacuum evaporated metals, electroless nickel, sputtered metals, etc.

6. Test and evaluate the wafer

Proper high temperature chemical reduction will result in a wafer of material which is curved or domed concave toward the reduced side. This effect is caused by the reduction in volume of the reduced layer as well as the difference in thermal expansion between the reduced layer (higher thermal expansion) and the dielectric layer (lower thermal expansion). The net effect of this process is to place the piezoelectrically active side of the wafer in compression, which is the most desirable configuration for reliability, load-bearing capability and long life.

Since the reduced ferroelectric or piezoelectric serves as the mechanical substrate and also the monolithic, conductive base electrode, a metallic electrode need only be deposited or applied to the opposite face (dielectric side) of the wafer. In practice, however, it has been found to be beneficial to deposit an electrode on top of the reduced layer in order to assure good electrical contact under high speed operation. For piezoelectric transducer applications, use of the reduced piezoelectric as a stress-biasing substrate as well as one of the electrodes affectively eliminates the bonding problem usually encountered in transducer fabrication and operation.

After attaching leads to the two electrodes, the device is finished and ready for operation. Since each individual device approximates one-half of a clamshell structure, two of them can be placed together to form a completed clamshell. These two Rainbow units can then be operated in series to produce twice the displacement of one unit. Additional units, in pairs of two, can be added to form a pump or motor of unusually high displacement in a very small volume. Axial displacements has high as 500% (relative to the wafer thickness); i.e., 50 mils displacement from a 10 mil wafer) have been obtained. However, these extremely high displacements are only available at relatively low pumping loads of less than 0.25 lb.

IV. Properties

The mechanical, dielectric and electromechanical properties of a selected number of PLZT piezoelectric and electrostrictive materials are shown in a number of figures (Figures 4 thru 31) in this section. They are given here without comment or description in the interest of disseminating them as expeditiously as possible. Some figures are replots of data to make them more useful and easy to obtain the desired information. The compositions for most of the work shown in the figures are of the piezoelectric type (typical: 5.5/56/44) and electrostrictive type (typical: 8.6/65/35).

Fig. 27. Characteristics of Temperature Compensated PLZT Wafer Combinations
Fig. 28. Voltage Dependent Strain/Hysteresis Characteristics of PLZT 9.5/65/35
Fig. 29. Voltage Dependent Strain/Hysteresis Characteristics of PLZT 9.5/65/35
Fig. 30. Effect of Pulse Frequency on ac Input Current
Fig. 31. Effect of Wafer Diameter on ac Input Current

The trade-offs of strain, point load, displacement, thickness and wafer diameter are given in Table 2. Although the values in the table are only approximate (being derived from rule-of-thumb observed relationships), they are considered to be real numbers in that the values presented can be obtained or exceeded in actual devices. As noted in the table notes, the displacements and strains are those achievable with a positive pulse at 450 volts. Less voltage will, of course, produce less displacement and strain; however, higher voltage will produce more. Also, bipolar pulses (or ac) will produce more displacement and strain than indicated in the table; more specifically, approximately twice as much.

V. Devices

A number of proof-of-principle demonstration devices have been constructed in the last few months. These include piston-type motors, cavity pumps, speakers, laser deflection devices, sensors, hydrophones, relay switches, fans and multifunction devices. All of these are in various stages of testing. In addition, life testing was carried out on one 1.25 inch diameter, 20 mil thick Rainbow piezoelectric wafer at 500 Hz. After 8 weeks of continuous operation consisting of 2.4×10^9 cycles at 350 volts (bipolar), there was no noticeable change in the amount of displacement (strain) at the given voltage. More work will be done in the future on device development, testing and evaluation. Present work is focusing on a cavity pump for space applications (cryogen pump) which necessitates the characterization of the Rainbow devices at 77K and an evaluation of their suitability for long term operation at these low temperatures.

Table 1. Ceramic Actuator Technologies

Type	Configuration	Max. Stress* (kg/cm^2)	Actuator Movement w/Voltage	Actuator Behavior (P or E)	Actuator Strain (%)
Monolithic (d_{33} mode)	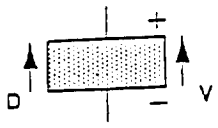	400	Expansion	P	0.40
Monolithic (d_{31} mode)	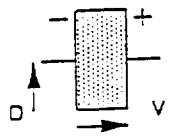	400	Contraction	P	-0.15
Monolithic (s_{11} mode)	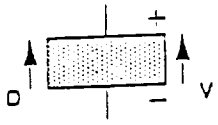	400	Expansion	E	0.24
Monolithic (s_{12} mode)	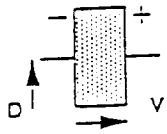	400	Contraction	E	-0.08
Composite Structure (d_{33} mode) (flexten.)	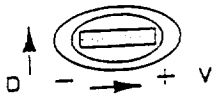	100	Contraction	P	-1.0
Composite Structure (d_{33}/d_{31}) (Moonie)	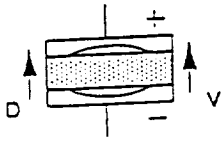	5	Expansion	P	1.2
Unimorph (bender)	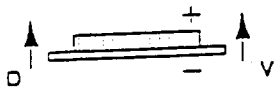	0.1	Expansion/ Contraction	P/E	10
Bimorph (bender)	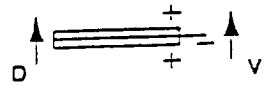	0.1	Expansion/ Contraction	P/E	20
Rainbow Monomorph (bender)	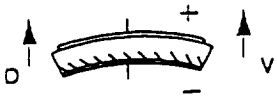	5	Expansion/ Contraction	P/E	500

Notes: V = Voltage; D = Actuator Displacement; P = Piezoelectric; E = Electrostrictor
Strain values at + or - 10 kV/cm; * = Maximum generated stress

Table 2. Performance Specifications of PLZT Rainbow Wafers

	d (wafer diameter)																				
	0.5			0.75			1			1.25			1.5			1.75			2		
t	y	L	S	y	L	S	y	L	S	y	L	S	y	L	S	y	L	S	y	L	S
mil	mil	lb.	%	mil	lb.	%	mil	lb.	%	mil	lb.	%	mil	lb.	%	mil	lb.	%	mil	lb.	%
6	14	0.7	233	21	0.5	350	28	0.4	467	35	0.3	583	42	0.3	49	49	0.2	817	56	0.2	933
8	8	1.3	100	12	0.9	150	16	0.6	200	20	0.5	250	23	0.4	27	27	0.4	338	31	0.3	388
10	5	2	50	8	1.3	80	10	1	100	13	0.8	130	15	0.7	18	18	0.6	180	20	0.5	200
15	2	4.5	13.3	3	3	20	4	2.3	26.7	6	1.8	40	7	1.5	8	8	1.3	53.3	9	1.1	60
20	1.3	8	6.5	1.9	5.3	9.5	2.5	4	12.5	3	3.2	15	3.8	2.7	4.5	4.5	2.3	22.5	5	2	25
25	0.8	12.5	3.2	1.2	8.3	4.8	1.6	6.3	6.4	2	5	8	2.4	4.2	2.8	2.8	3.6	11.3	3.2	3.1	12.8
30	0.6	18	2	0.8	12	2.7	1.1	9	3.7	1.4	7.2	4.7	1.7	6	1.9	1.9	5.1	6.3	2.2	4.5	7.3
35	0.4	24.5	1.1	0.6	16.3	1.7	0.8	12.3	2.3	1	9.8	2.9	1.2	8.2	1.4	1.4	7	4	1.6	6.1	4.6
40	0.3	32	0.8	0.5	21.3	1.3	0.6	16	1.5	0.8	12.8	2	0.9	10.7	1.1	1.1	9.1	2.8	1.3	8	3.3
45	0.3	40.5	0.7	0.4	27	0.9	0.5	20.3	1.1	0.6	16.2	1.3	0.7	13.5	0.9	0.9	11.6	2	1	10.1	2.2
50	0.2	50	0.4	0.3	33.3	0.6	0.4	25	0.8	0.5	20	1	0.6	16.7	0.7	0.7	14.3	1.4	0.8	12.5	2
55	0.2	60.5	0.3	0.3	40.3	0.5	0.3	30.3	0.6	0.4	24.2	0.7	0.5	20.2	0.6	0.6	17.3	1.1	0.7	15.1	1.3
60	0.1	72.1	0.2	0.2	48	0.3	0.3	36	0.5	0.4	28.8	0.7	0.4	24	0.5	0.5	20.6	0.8	0.6	18	1

Notes:

L = Load in pounds

S = Axial Strain in percent (based on wafer thickness)

t = Wafer thickness in mils

d = Wafer diameter in inches

y = Wafer axial displacement in mils

All values are for +450 volts operation

Formulae for generating this table:

$y = (d/t^2) \times 10^{-3}$ (mils)

$S = (d/t^3) \times 10^{-4}$ (%)

$L = (t^2/d) \times 10^4$ (lbs.)

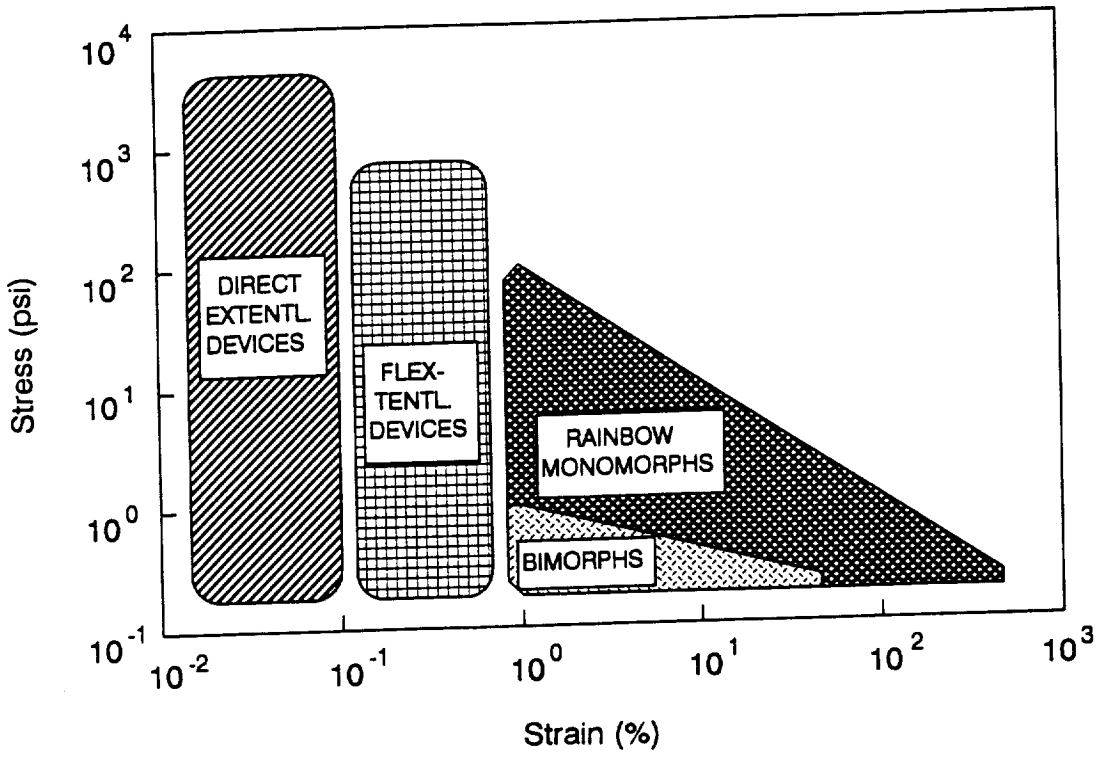

Figure 1. A Comparison of Ceramic Actuator Technologies

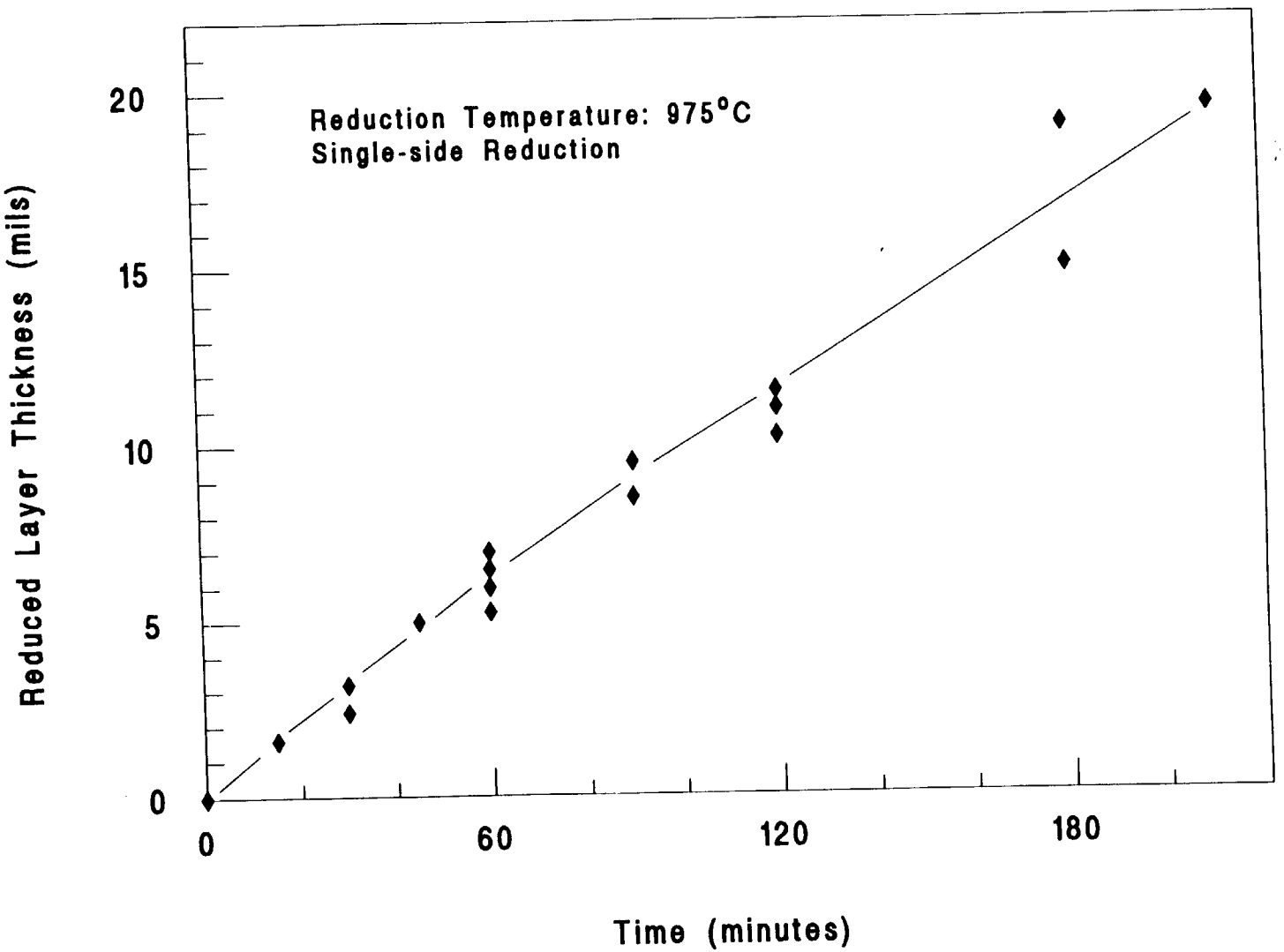

Figure 2. Effect of Reduction Time on the Thickness of the Reduced Layer in PLZT Ceramics

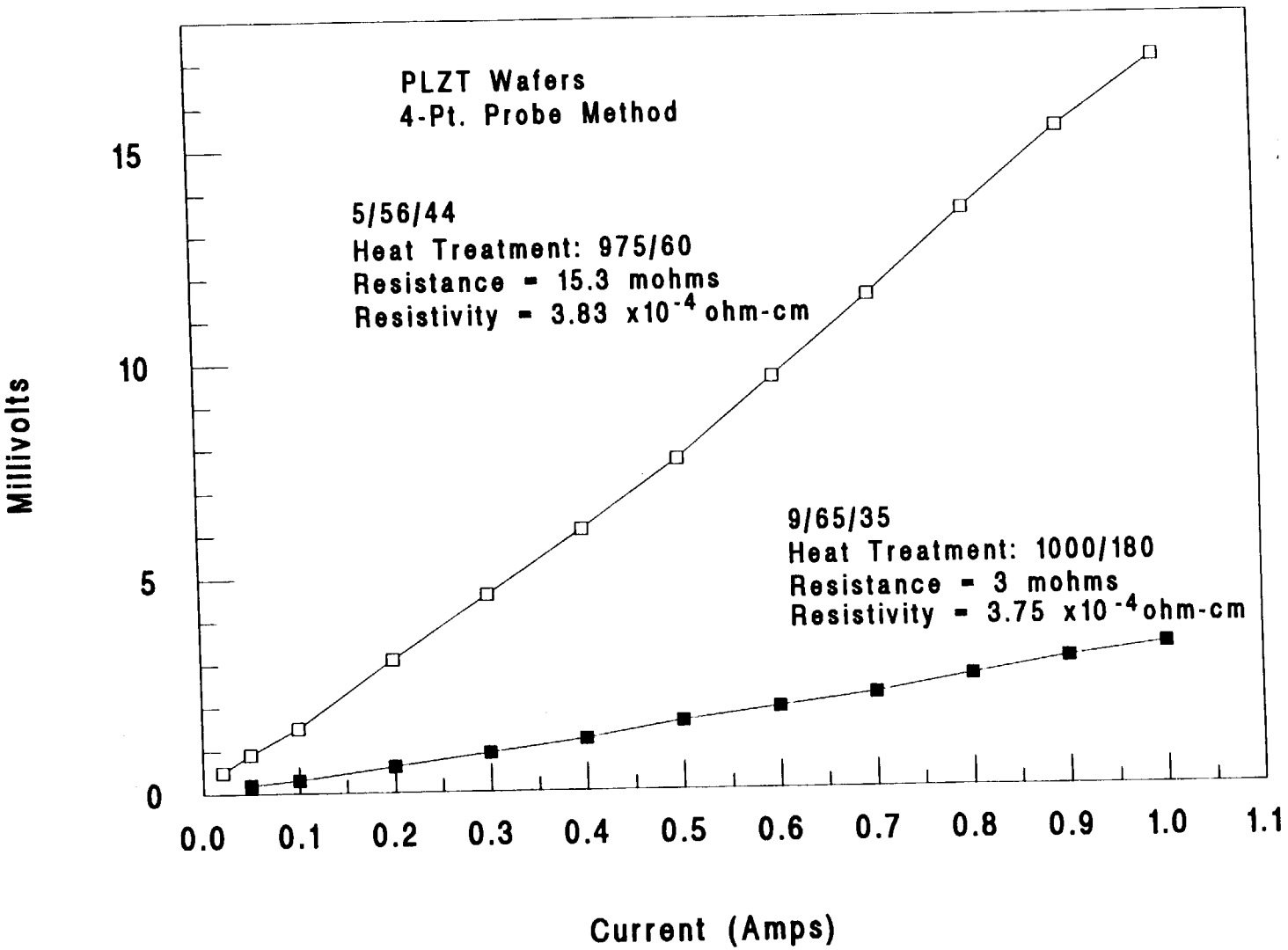

Figure 3. Ohmic Characteristics of Chemically Reduced Layers in Rainbow Wafers

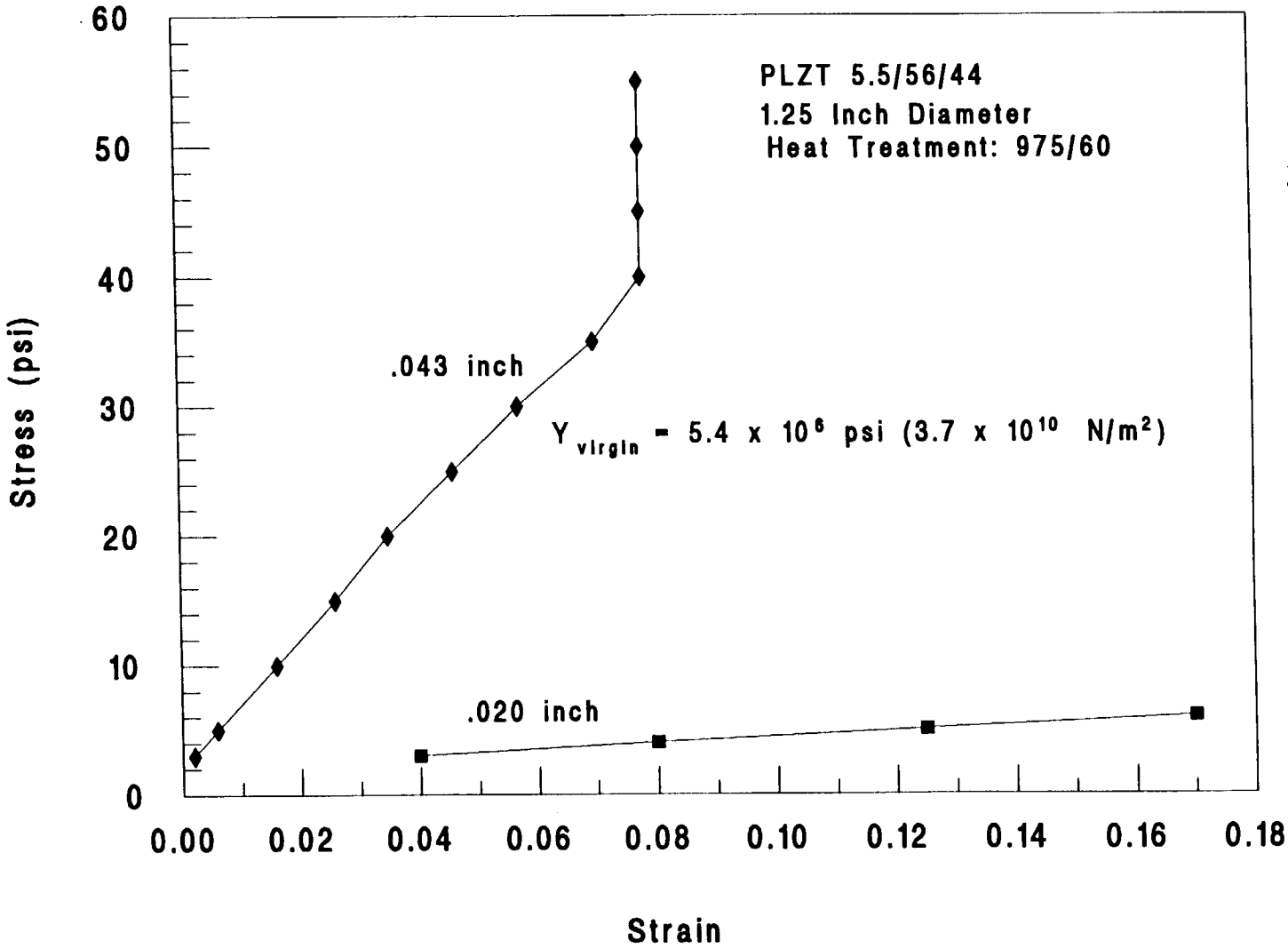

Figure 4. Elastic Modulus Characteristics of PLZT 5.5/56/44 Rainbow Wafers at Indicated Thicknesses

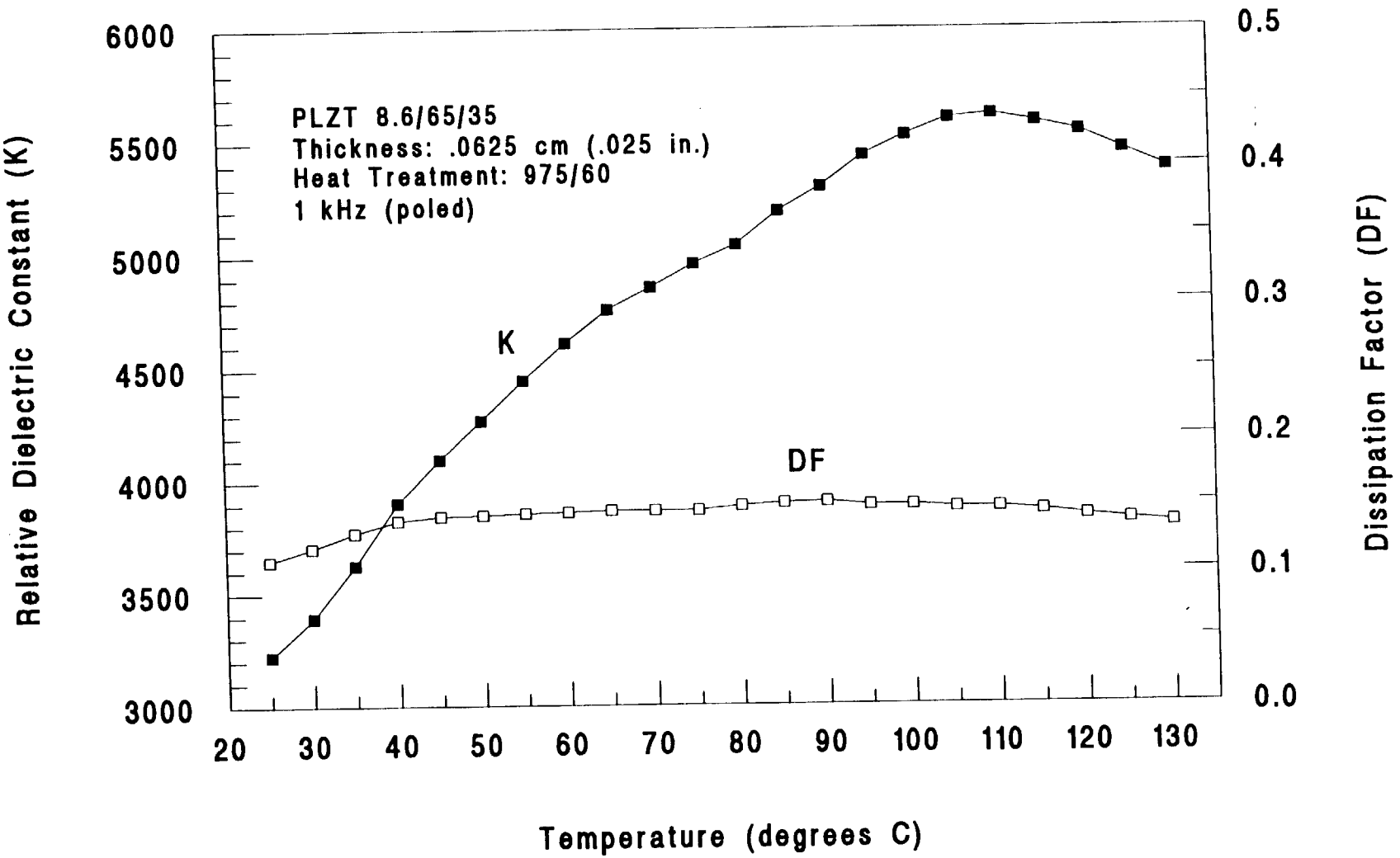

Figure 5. Effect of Temperature on the Dielectric Properties of PLZT 8.6/65/35 Rainbow Wafer

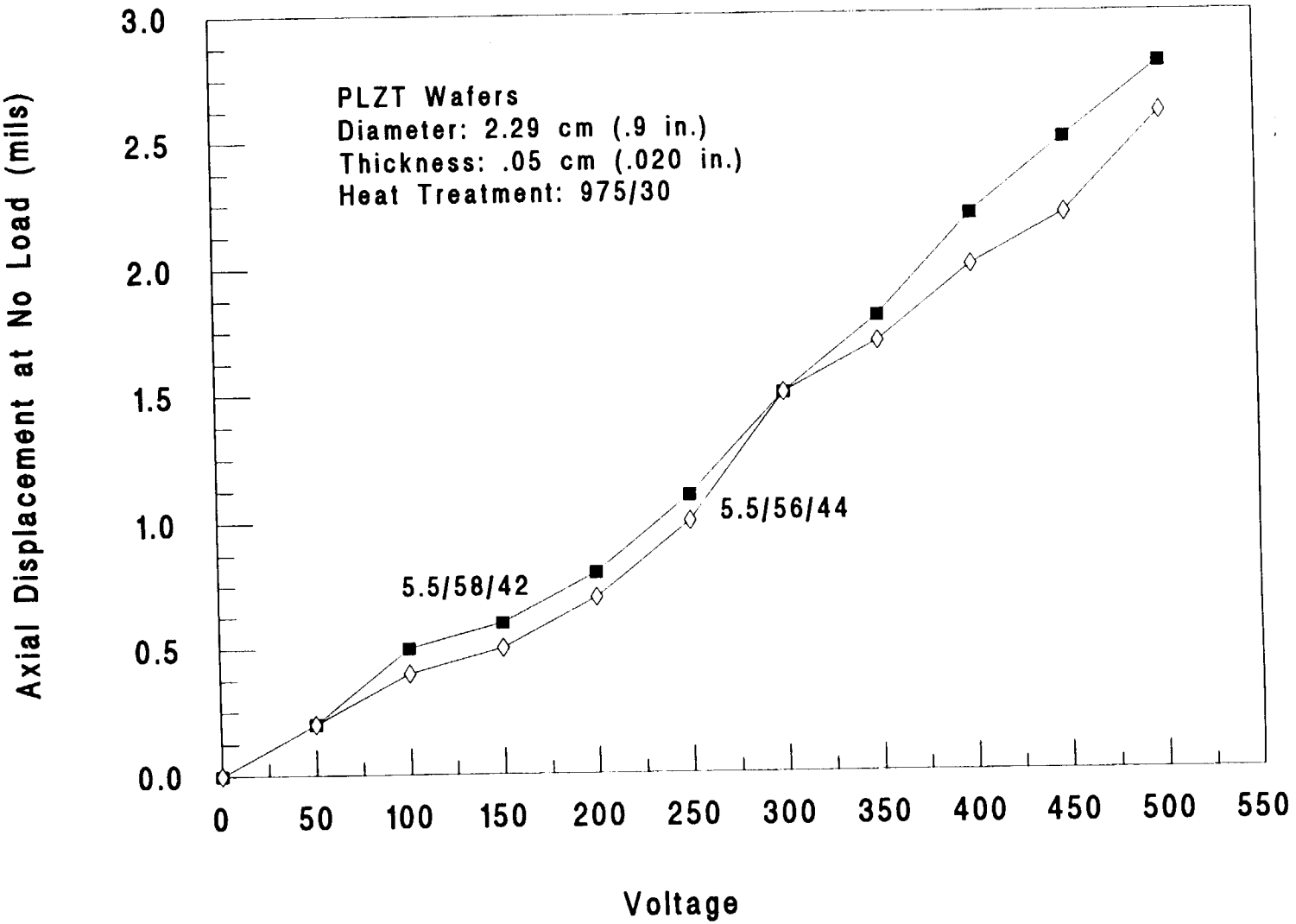

Figure 6. Voltage Dependent Axial Displacement Characteristics of PLZT 5.5/58/42 and 5.5/56/44 Rainbow Wafers

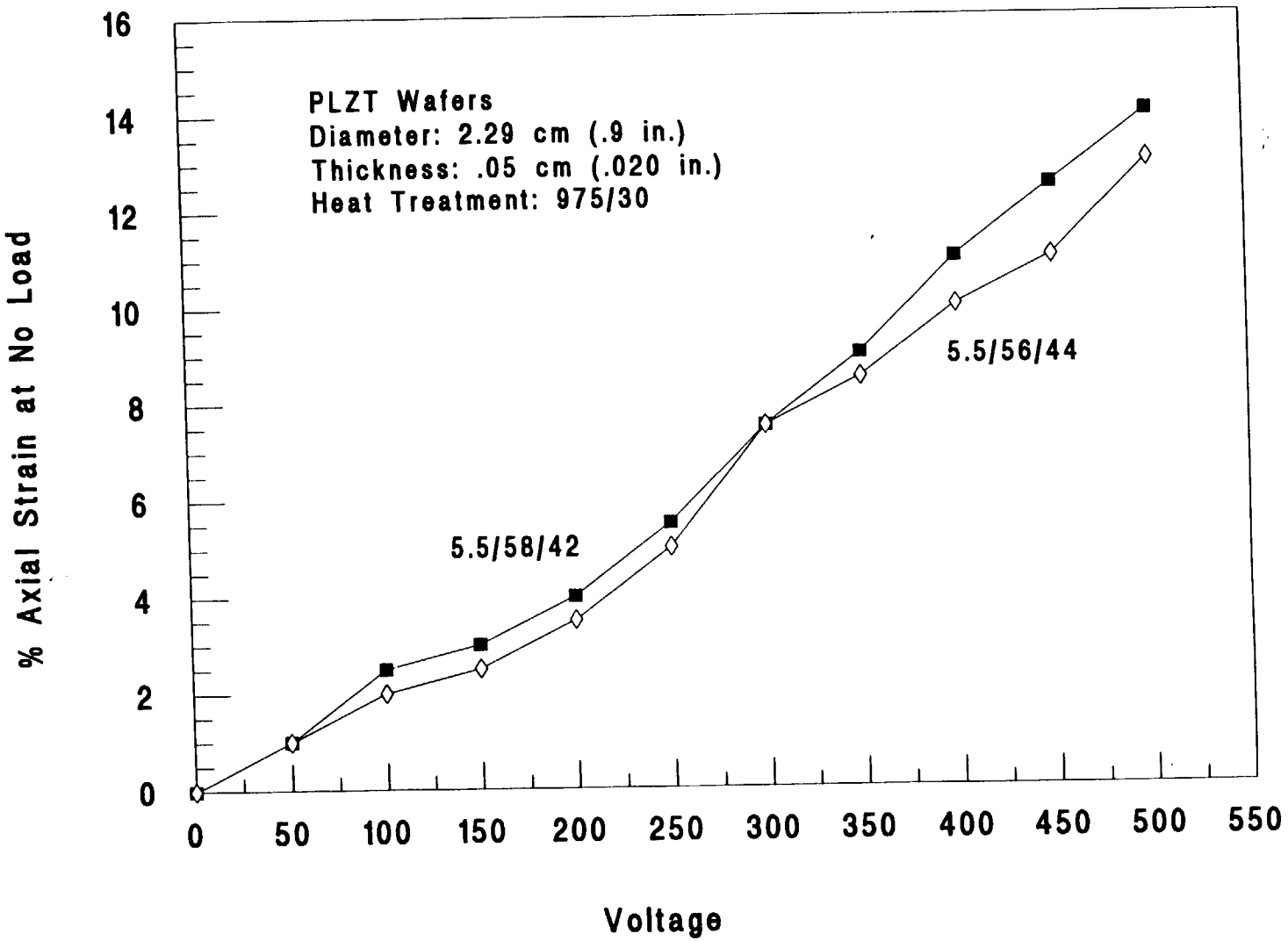

Figure 7. Voltage Dependent Axial Strain Characteristics of PLZT 5.5/58/42 and 5.5/56/44 Rainbow Wafers

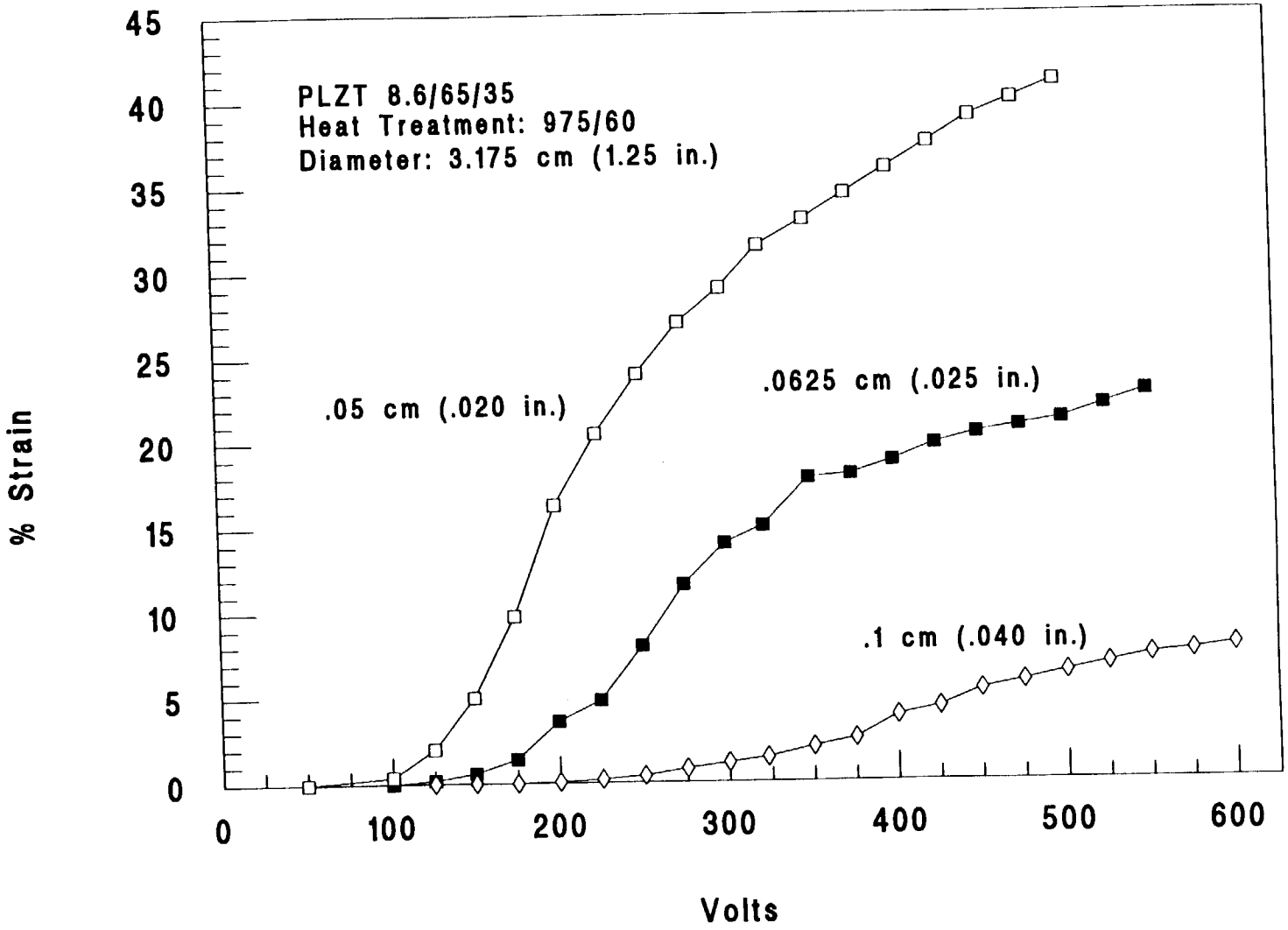

Figure 8. Voltage Dependent Strain Characteristics of PLZT 8.6/65/35 Rainbow Wafers

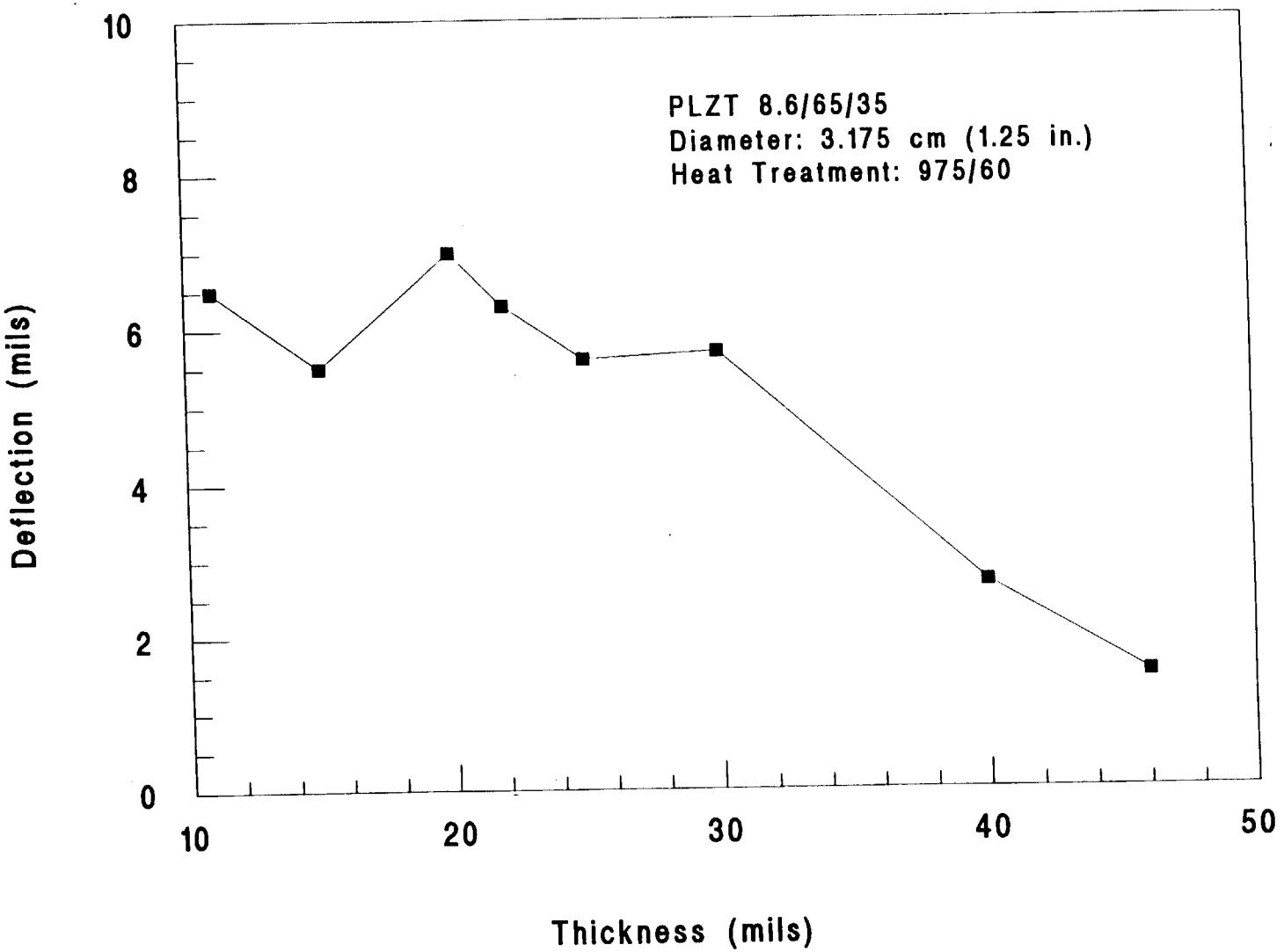

Figure 9. Effect of Thickness on Total Deflection of PLZT 8.6/65/35 Rainbow Wafer

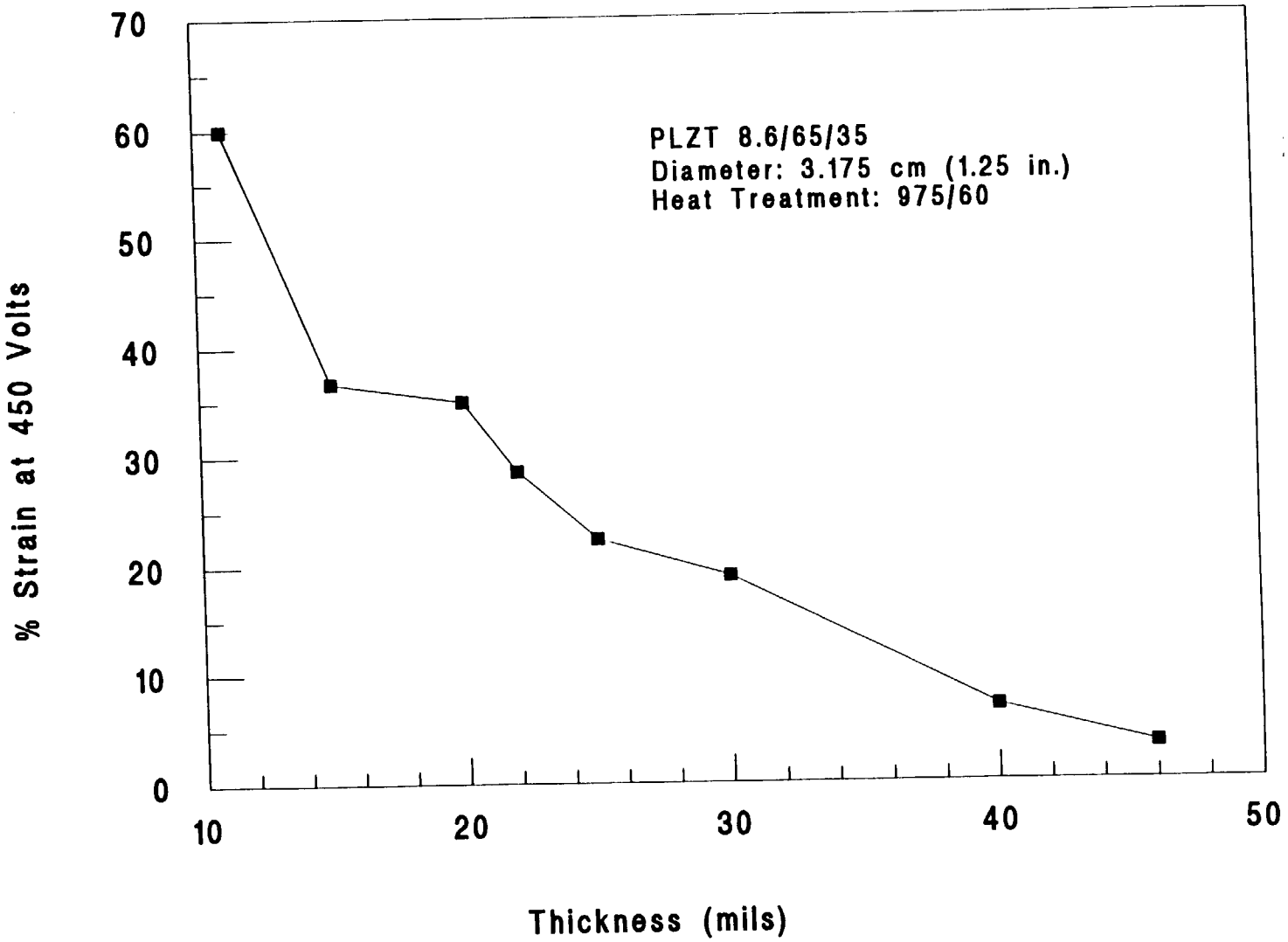

Figure 10. Effect of Thickness on Strain Characteristics of PLZT 8.6/65/35 Rainbow Wafers

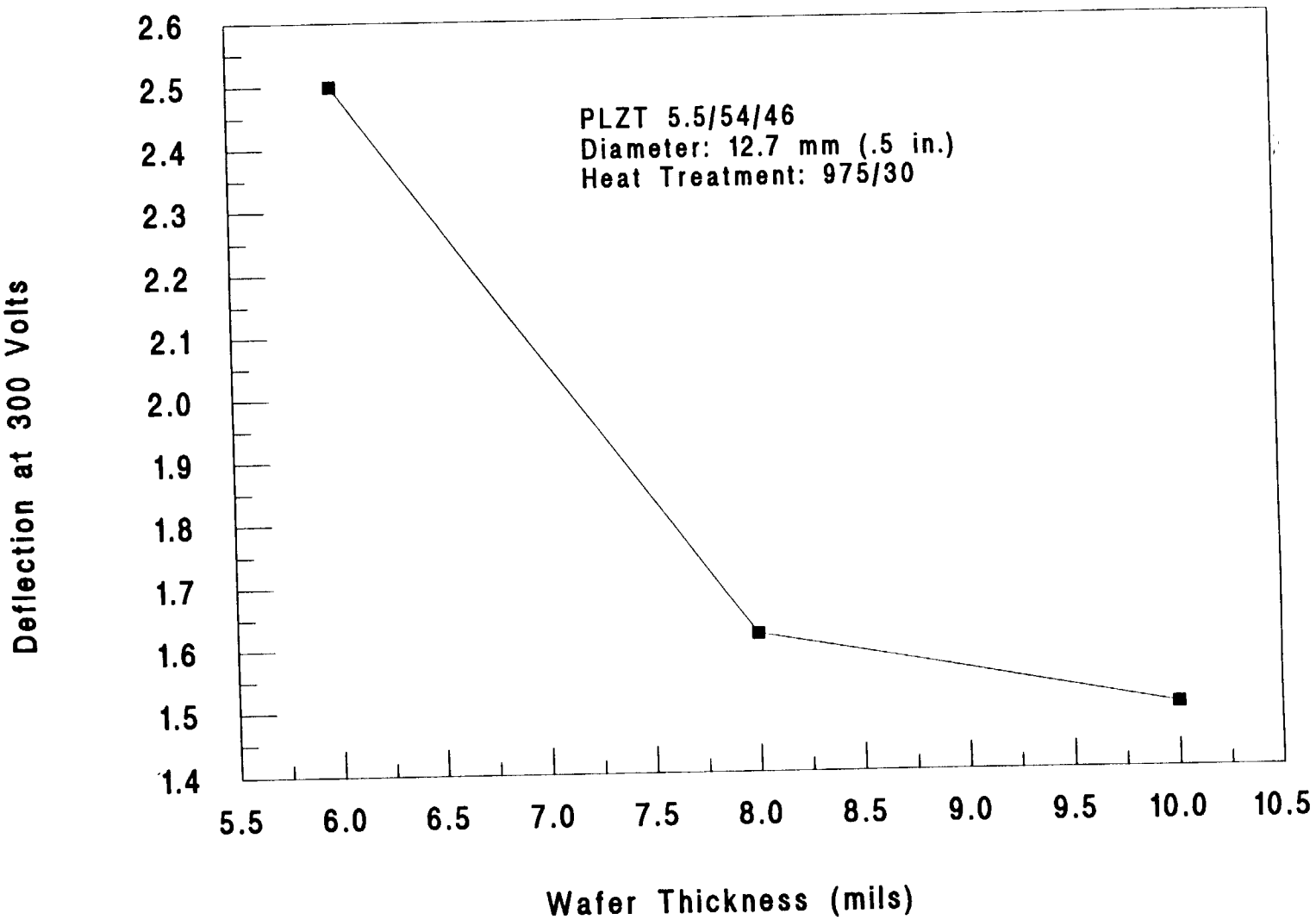

Figure 11. Deflection of PLZT Rainbow Wafers as a Function of Wafer Thickness

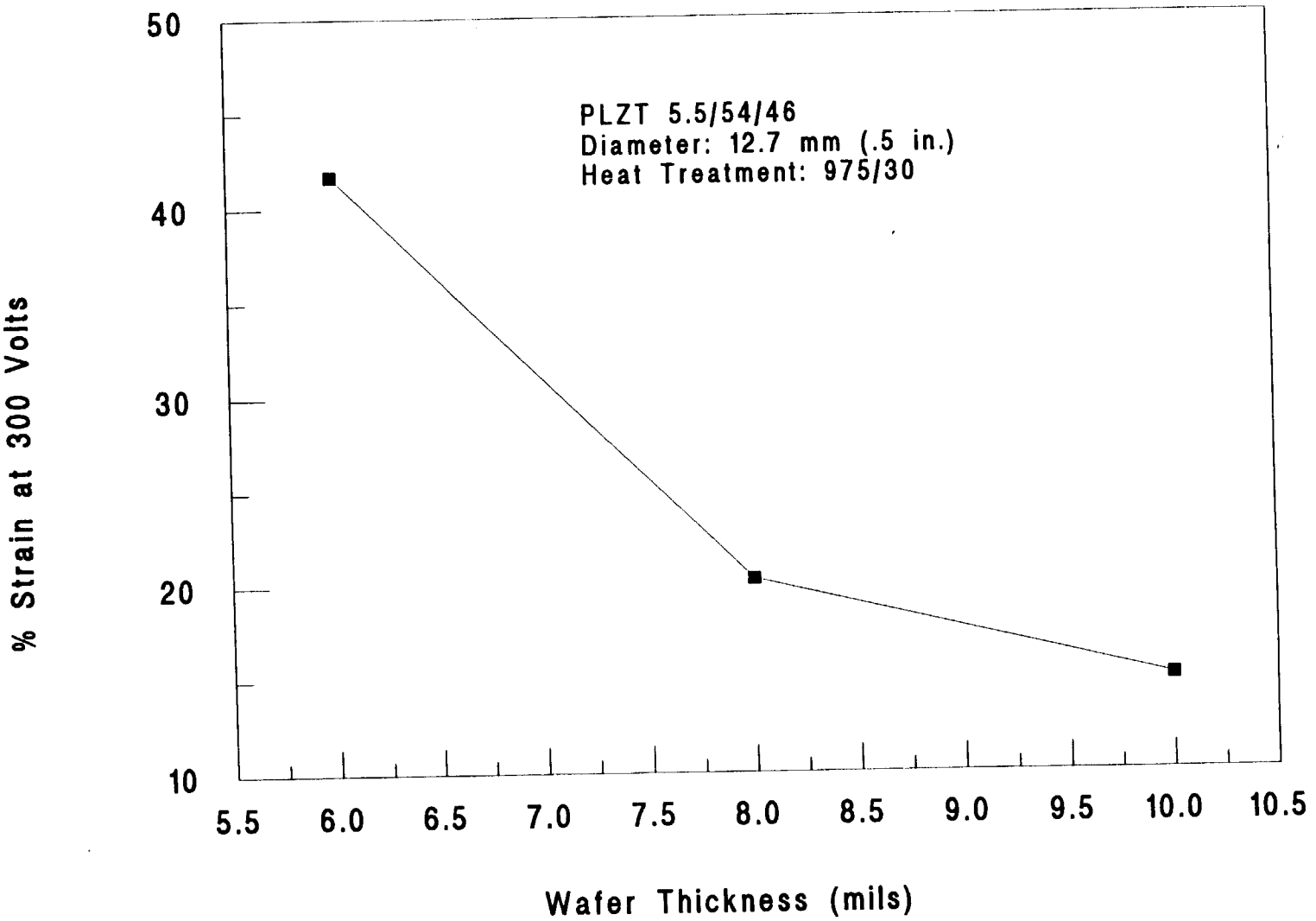

Figure 12. Strain Characteristics of PLZT Rainbow Wafers as a Function of Thickness

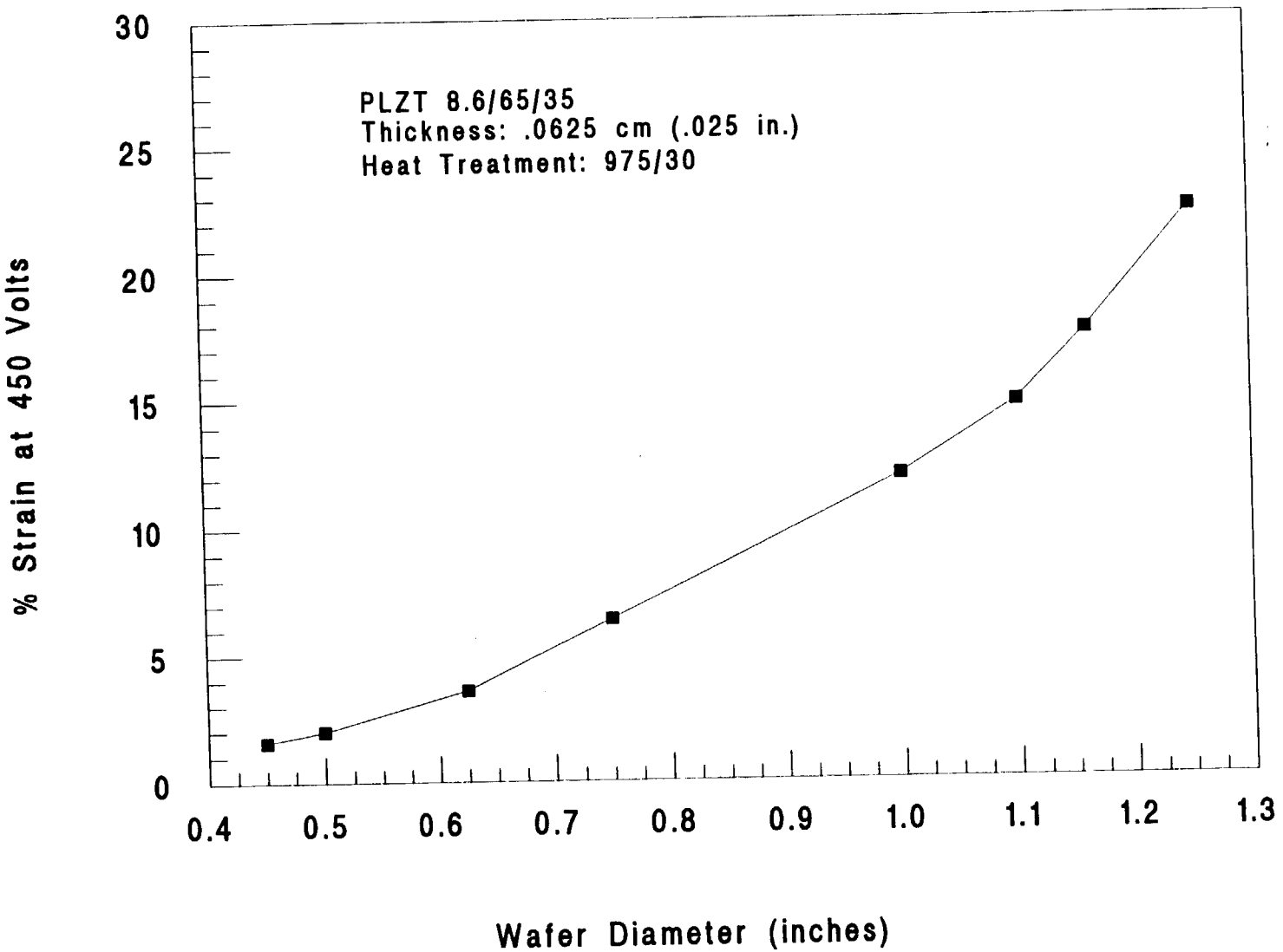

Figure 13. Strain Characteristics of PLZT Rainbow Wafers as a Function of Wafer Diameter

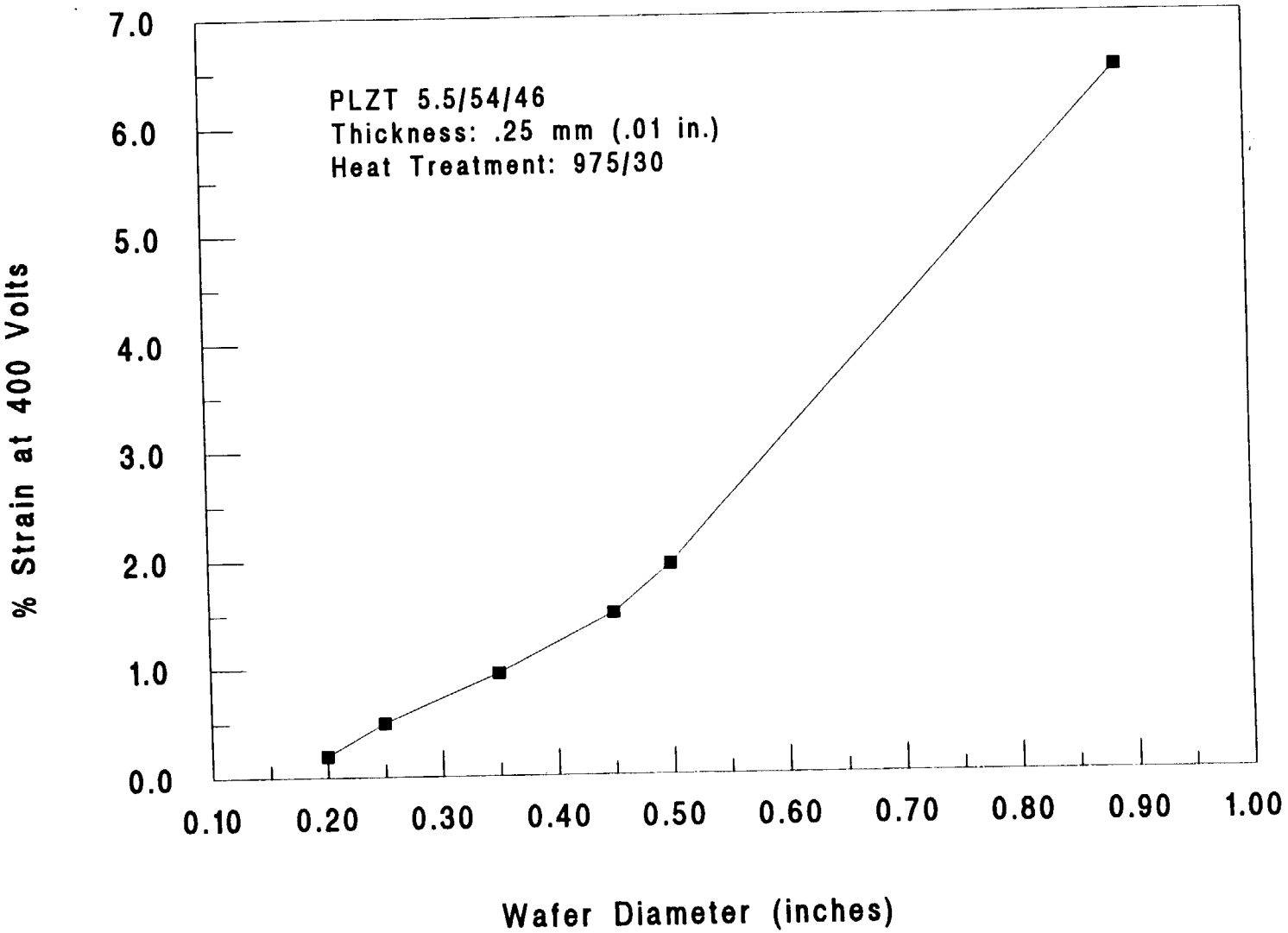

Figure 14. Strain Characteristics of PLZT Rainbow Wafers as a Function of Diameter

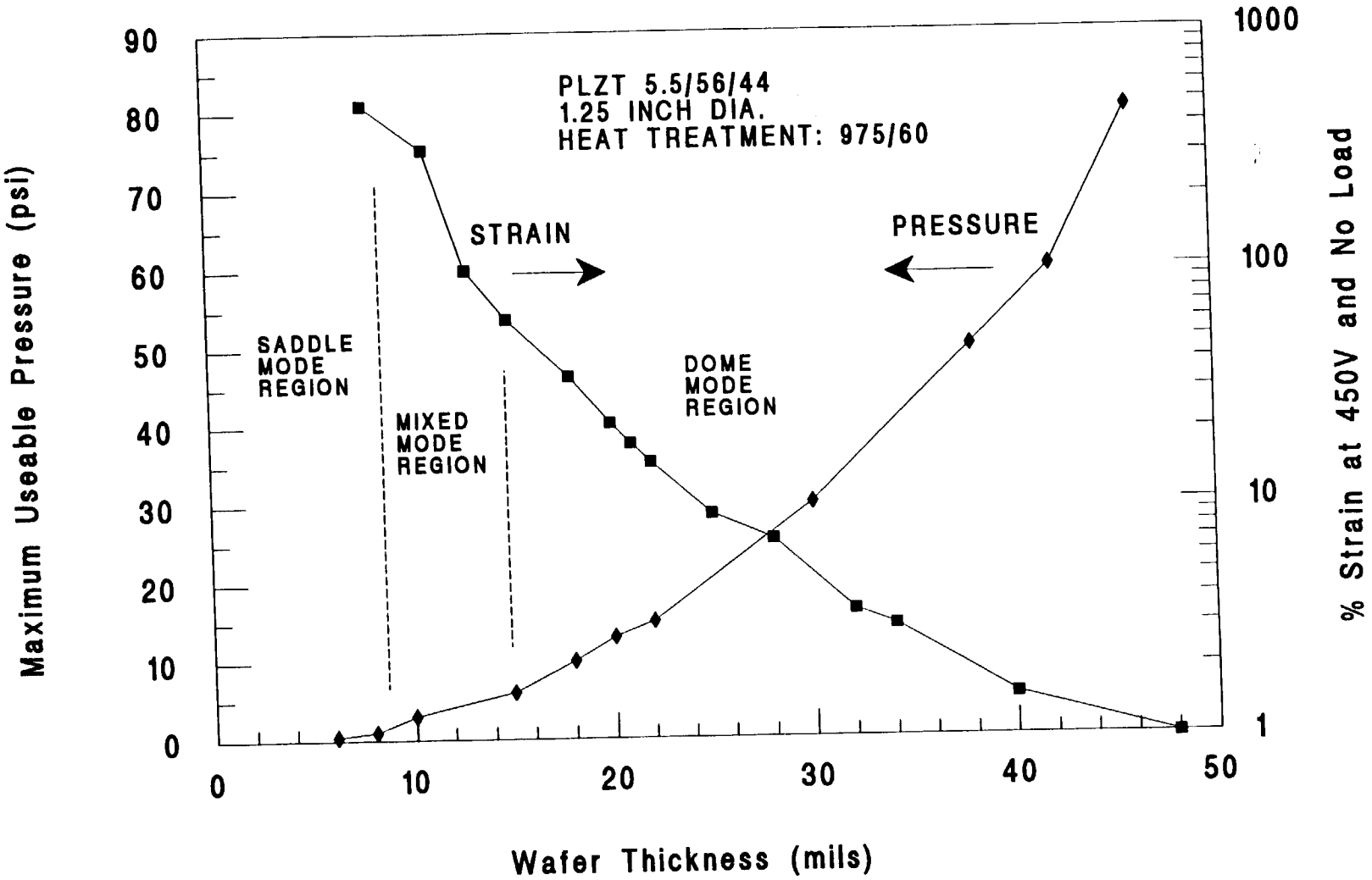

Figure 15. Pressure and Strain Characteristics of PLZT Rainbow Wafers

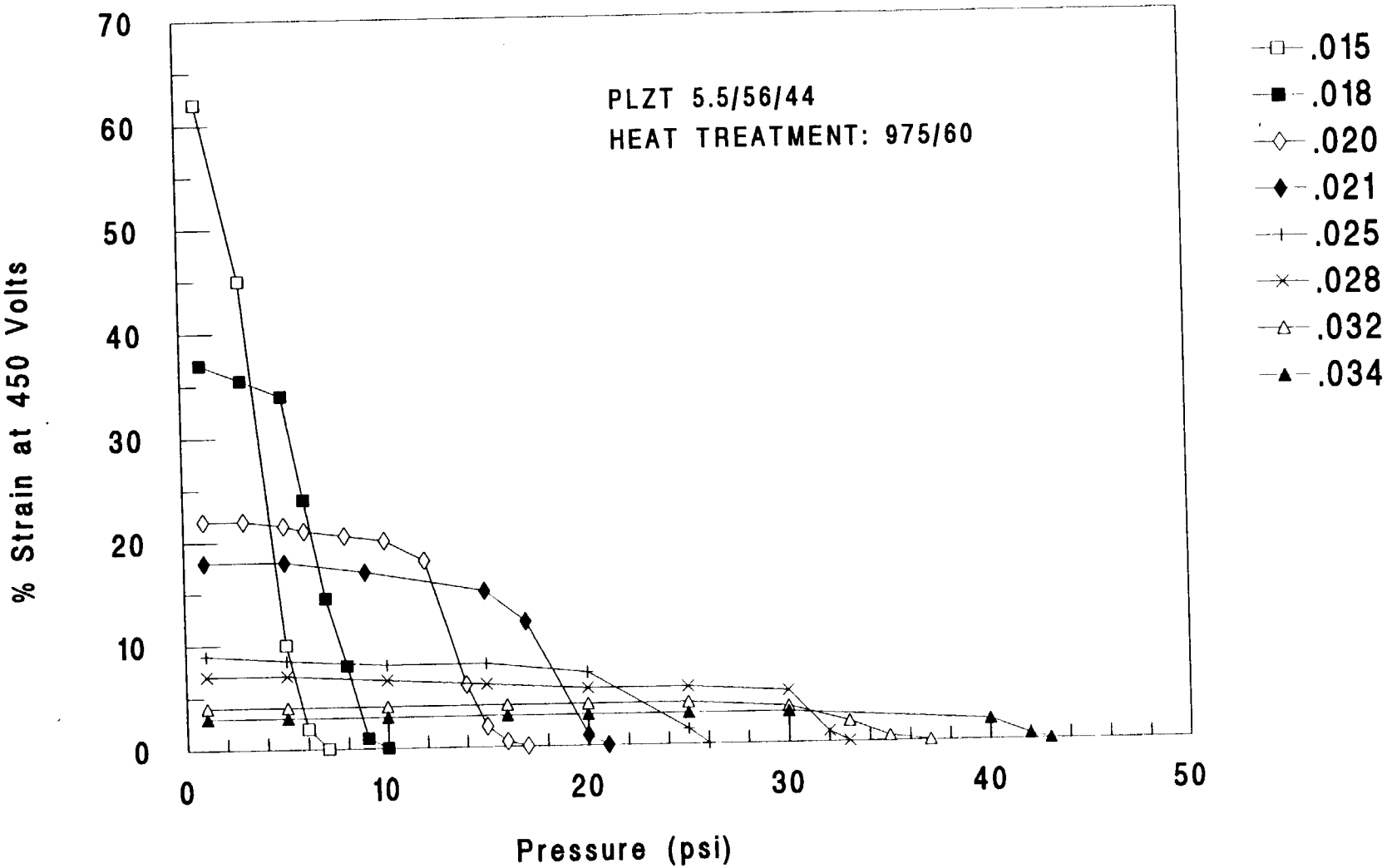

Figure 16. EFfect of Pressure on Strain in PLZT Wafers of Varying Thickness

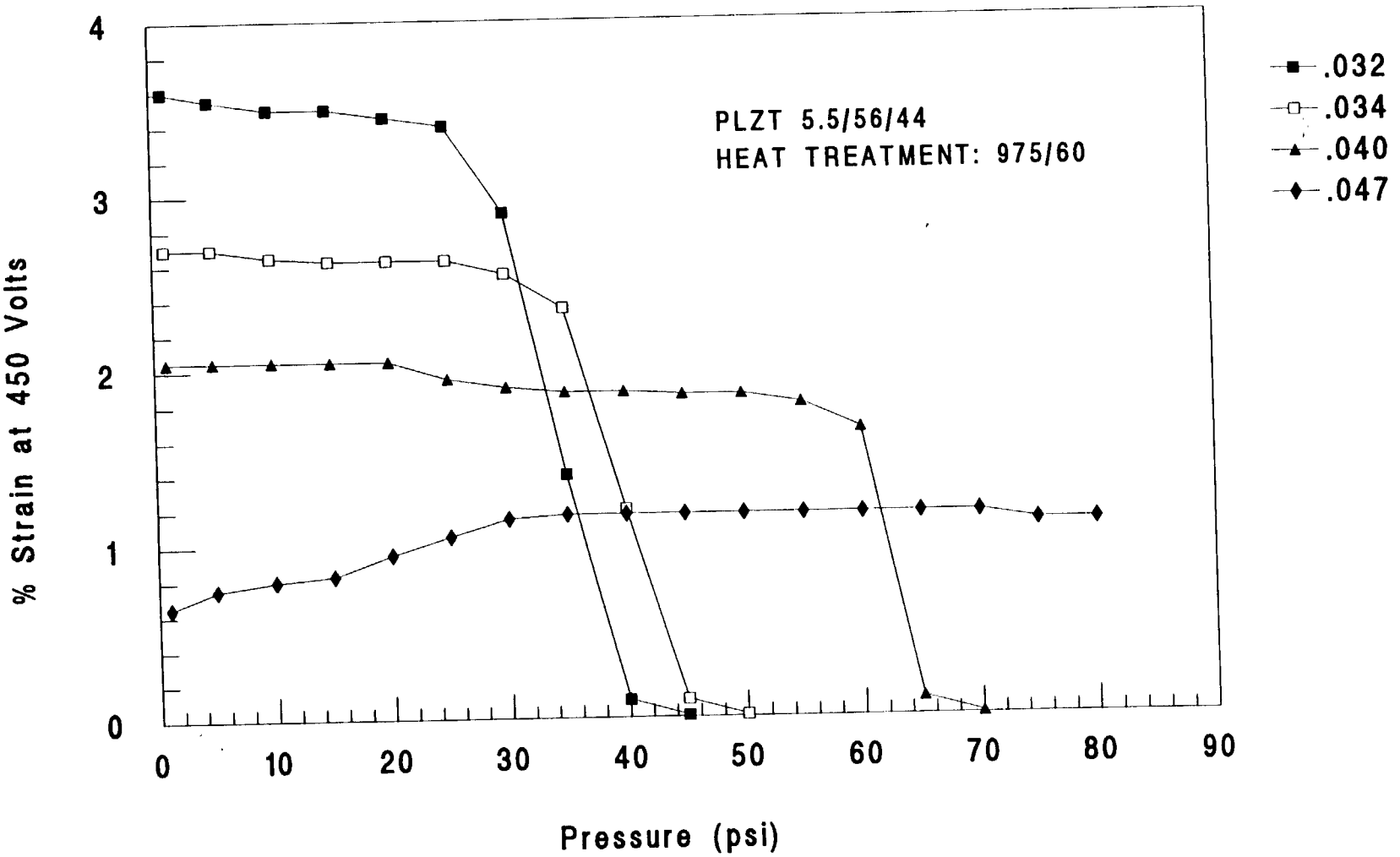

Figure 17. Effect of Pressure on Strain in PLZT Wafers of Varying Thickness

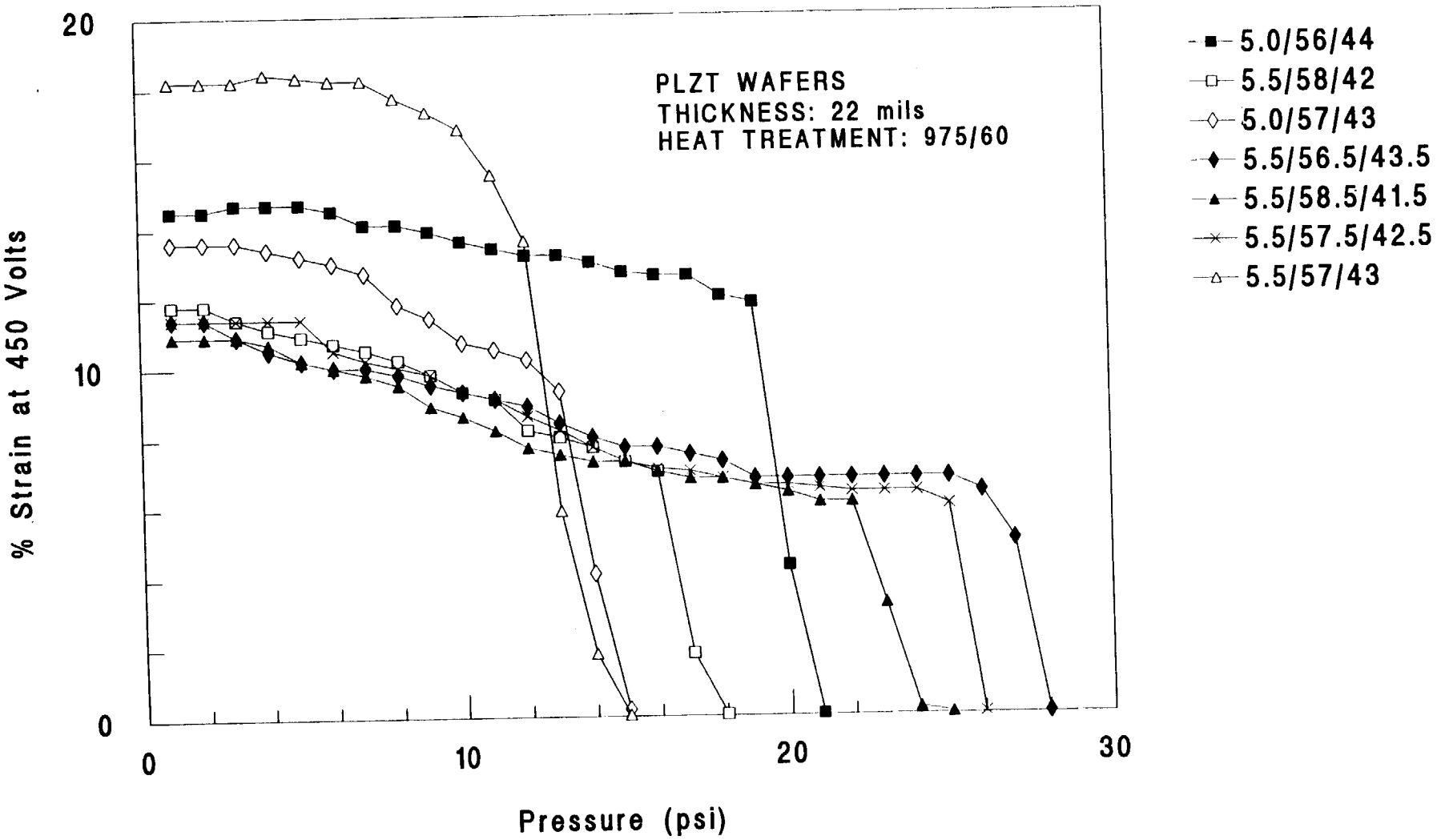

Figure 18. Effect of Pressure on Strain in the PLZT Rainbow Wafers

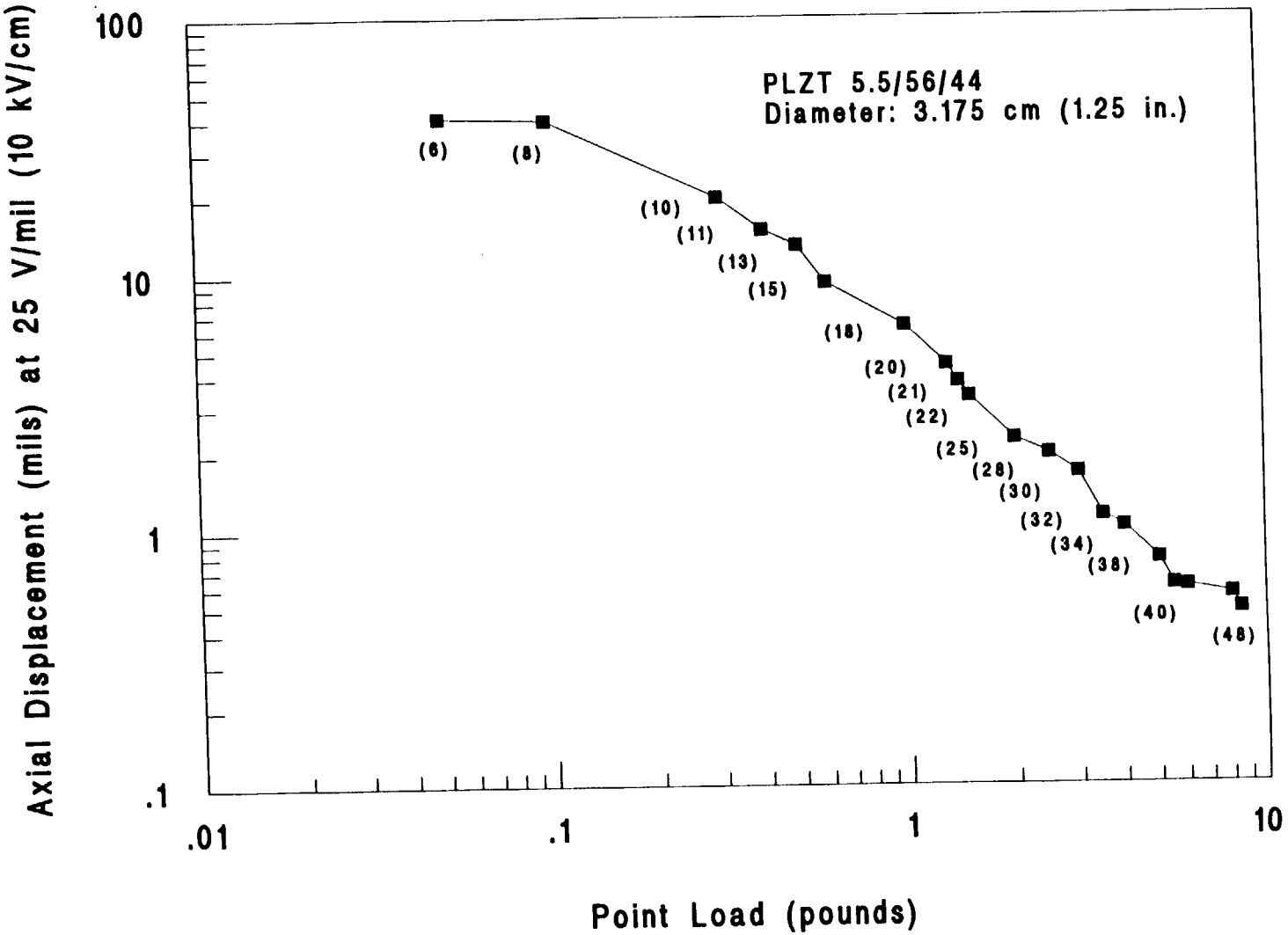

Figure 19. The Trade-Off of Displacement vs. Load for PLZT Rainbow Wafers of Varying Thicknesses (in parentheses)

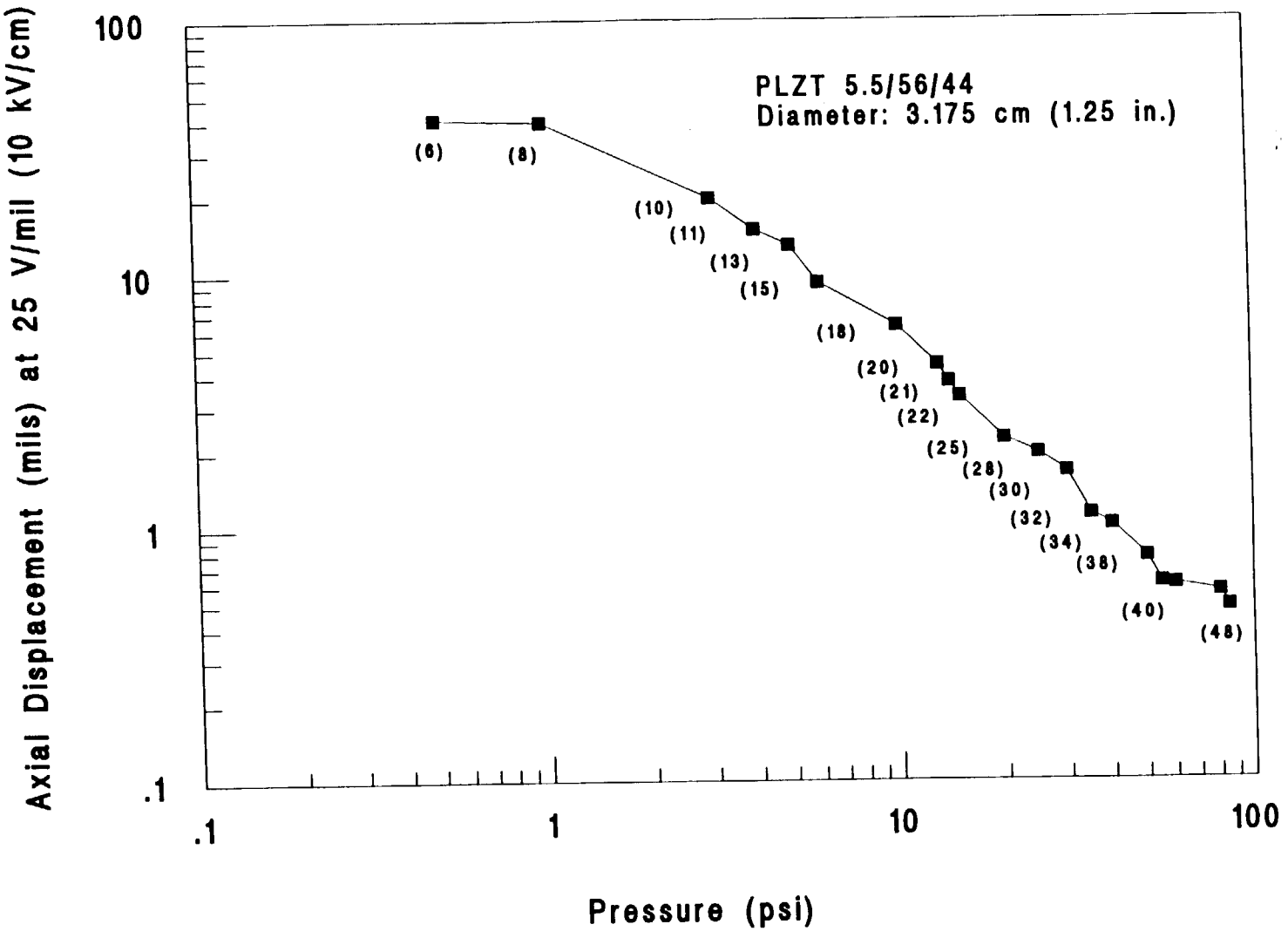

Figure 20. The Trade-Off of Displacement vs. Pressure for PLZT Rainbow Wafers of Varying Thicknesses (in parentheses)

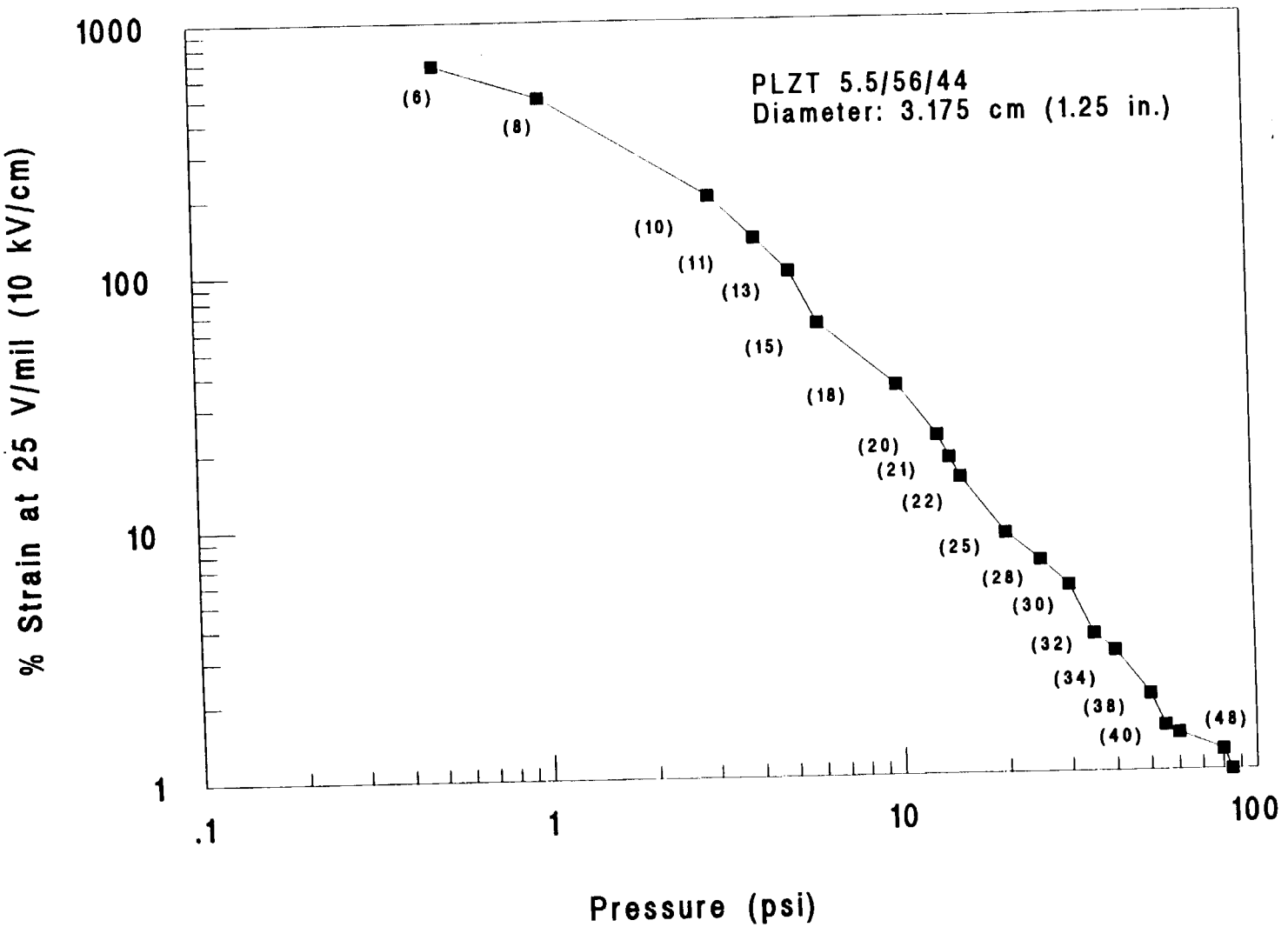

Figure 21. The Trade-Off of Strain vs. Pressure for PLZT Rainbow Wafers of Varying Thicknesses (in parentheses)

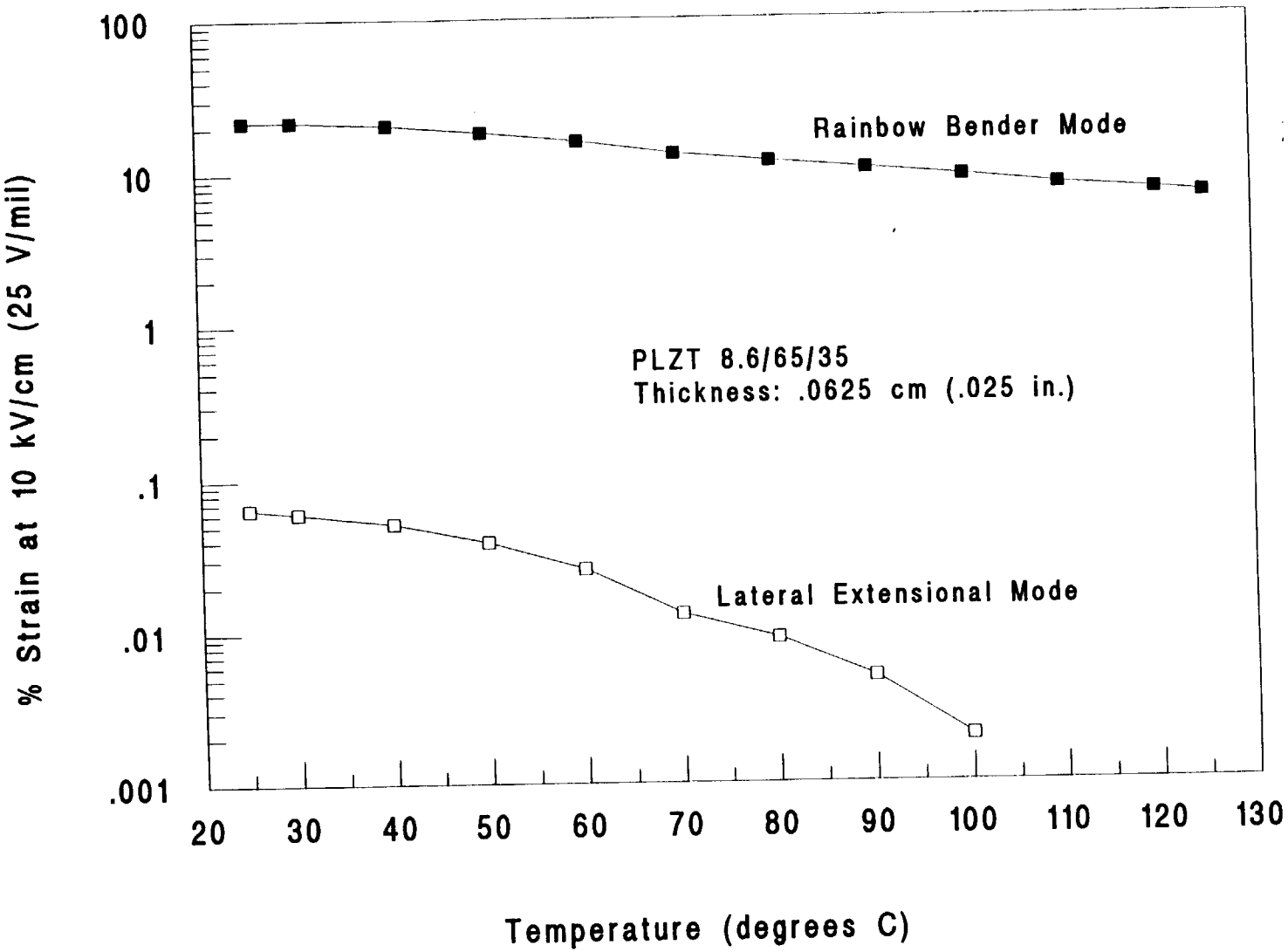

Figure 22. Temperature Dependence of Electrostrictive Lateral and Rainbow Strains in PLZT 8.6/65/35 Ceramics

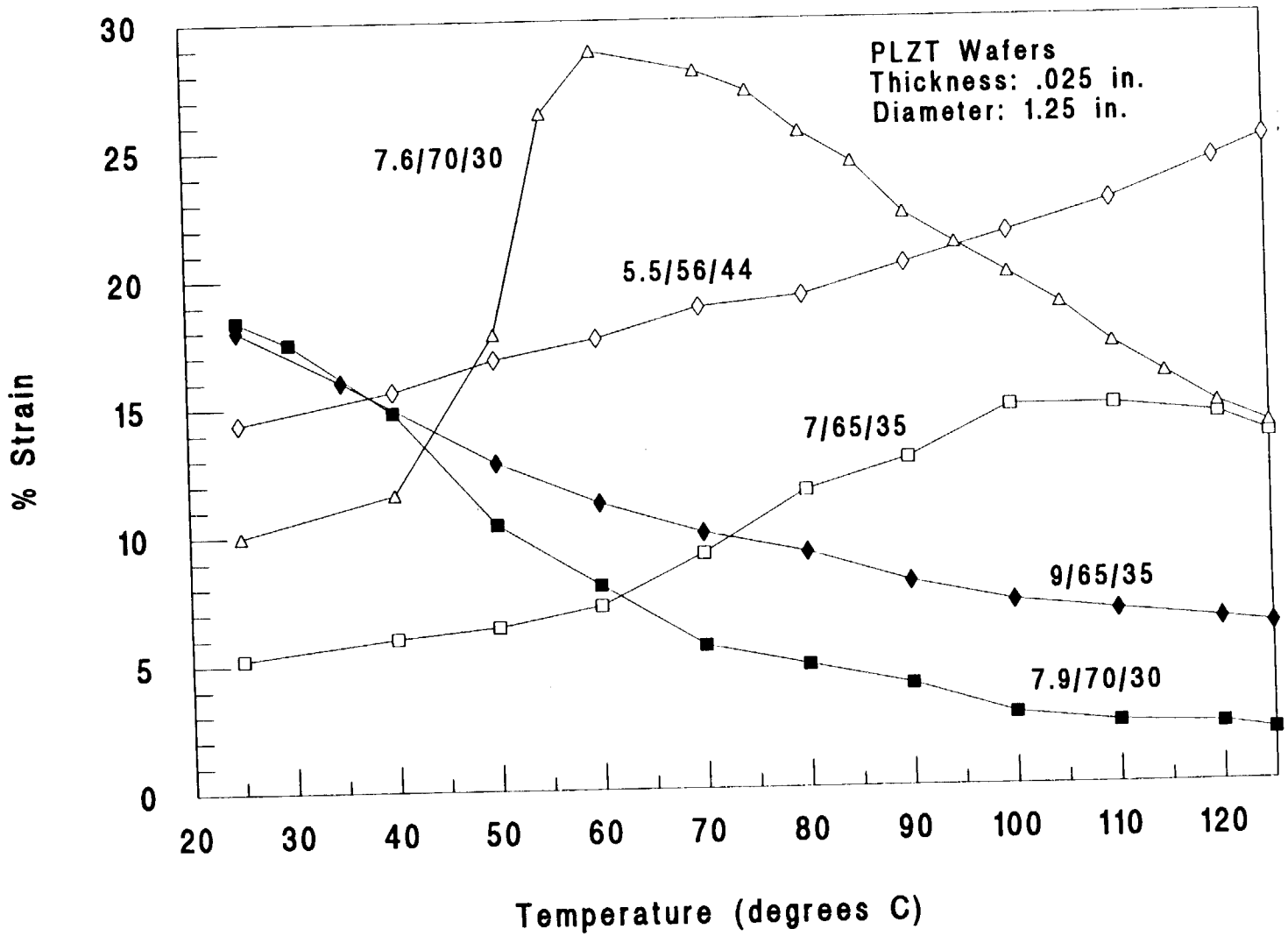

Figure 23. Temperature Dependent Strain Characteristics of PLZT Rainbow Wafers

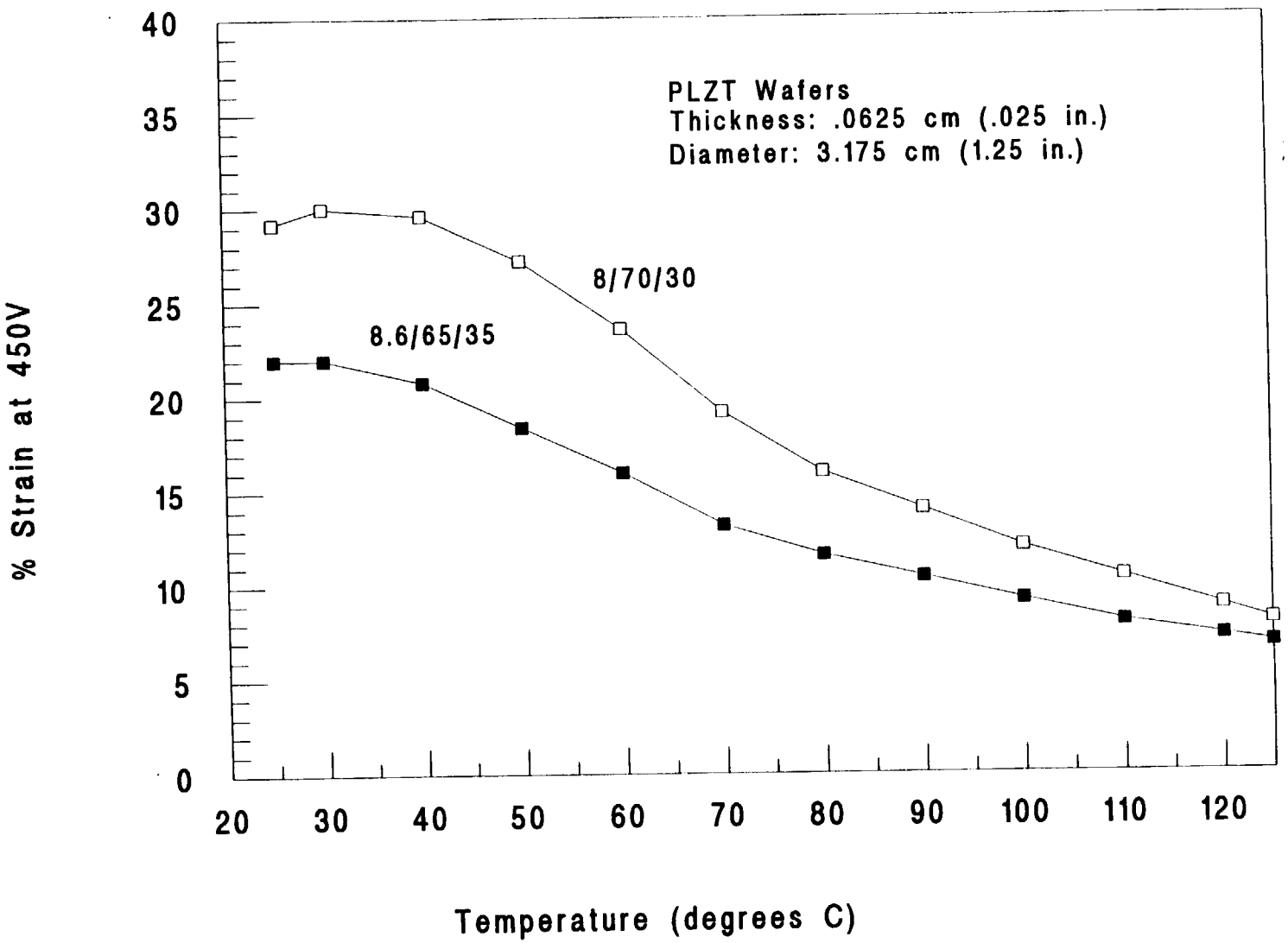

Figure 24. Strain Characteristics of Temperature Compensated PLZT Rainbow Wafers

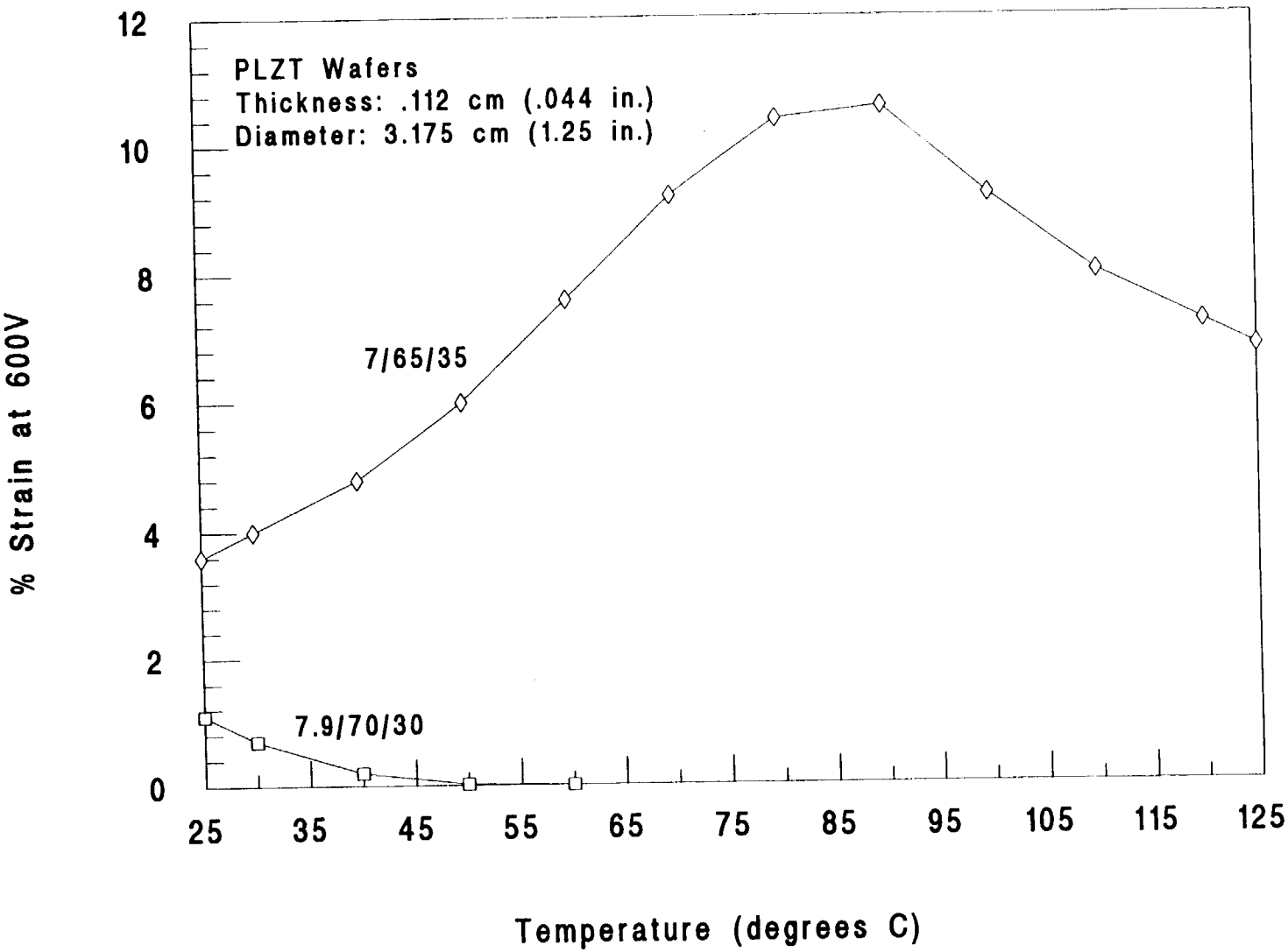

Figure 25. Strain Characteristics of Temperature Compensated PLZt Rainbow Wafers

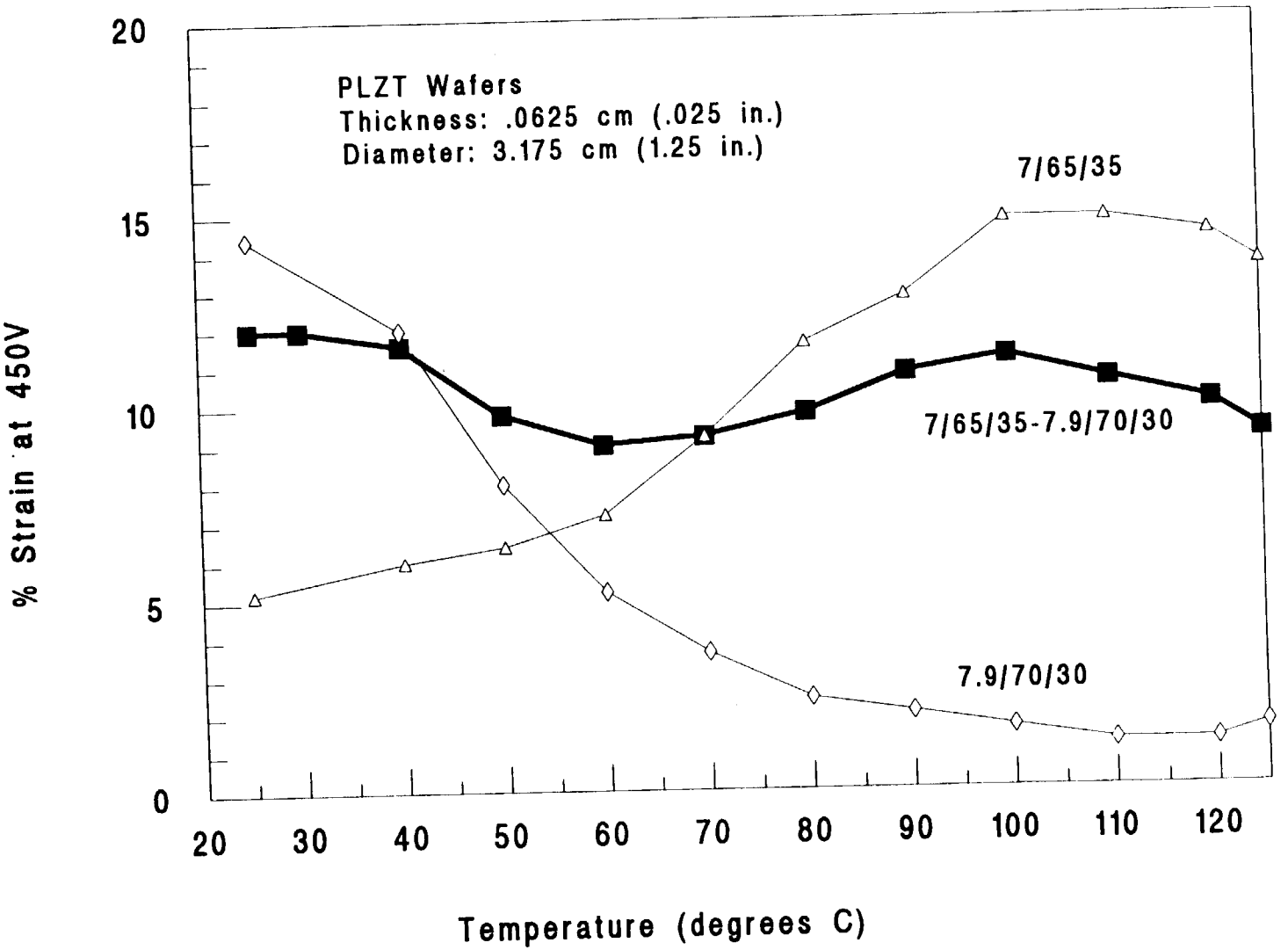

Figure 26. Strain Characteristics of Temperature Compensated PLZT Rainbow Wafers

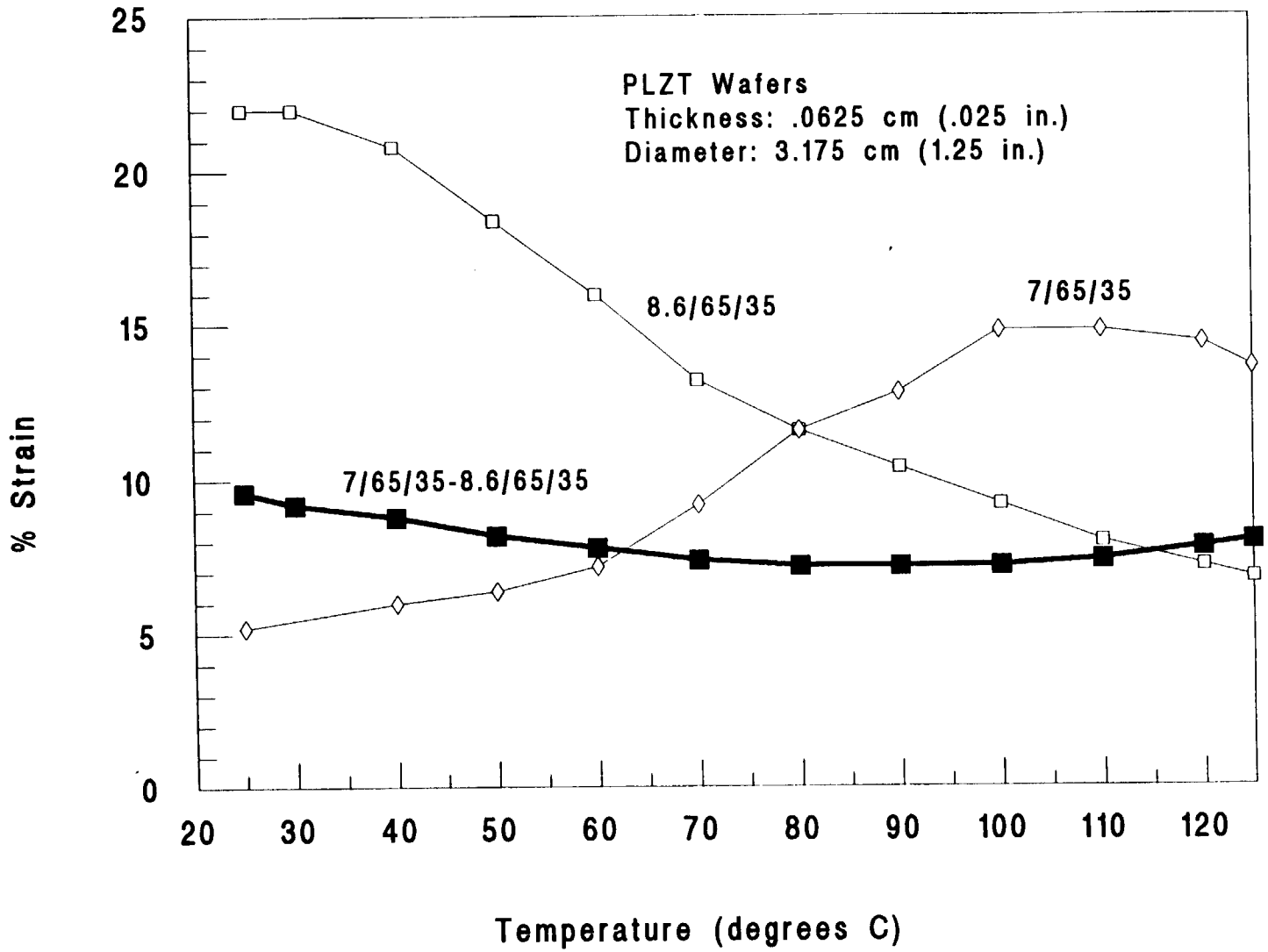

Figure 27. Strain Characteristics of Temperature Compensated PLZT Rainbow Wafers

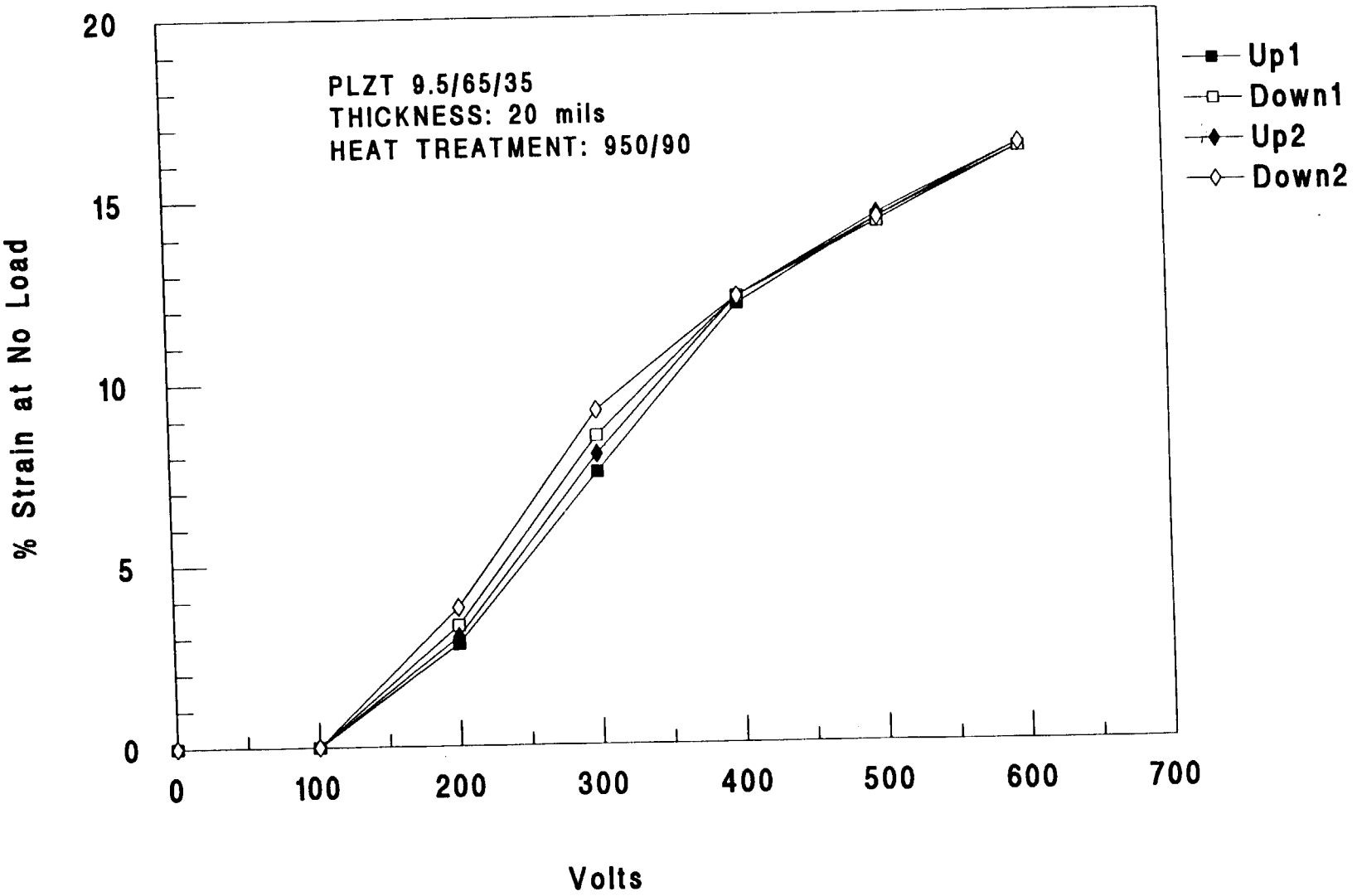

Figure 28. Voltage Dependent Strain and Hysteresis Characteristics of PLZT Rainbow Wafers

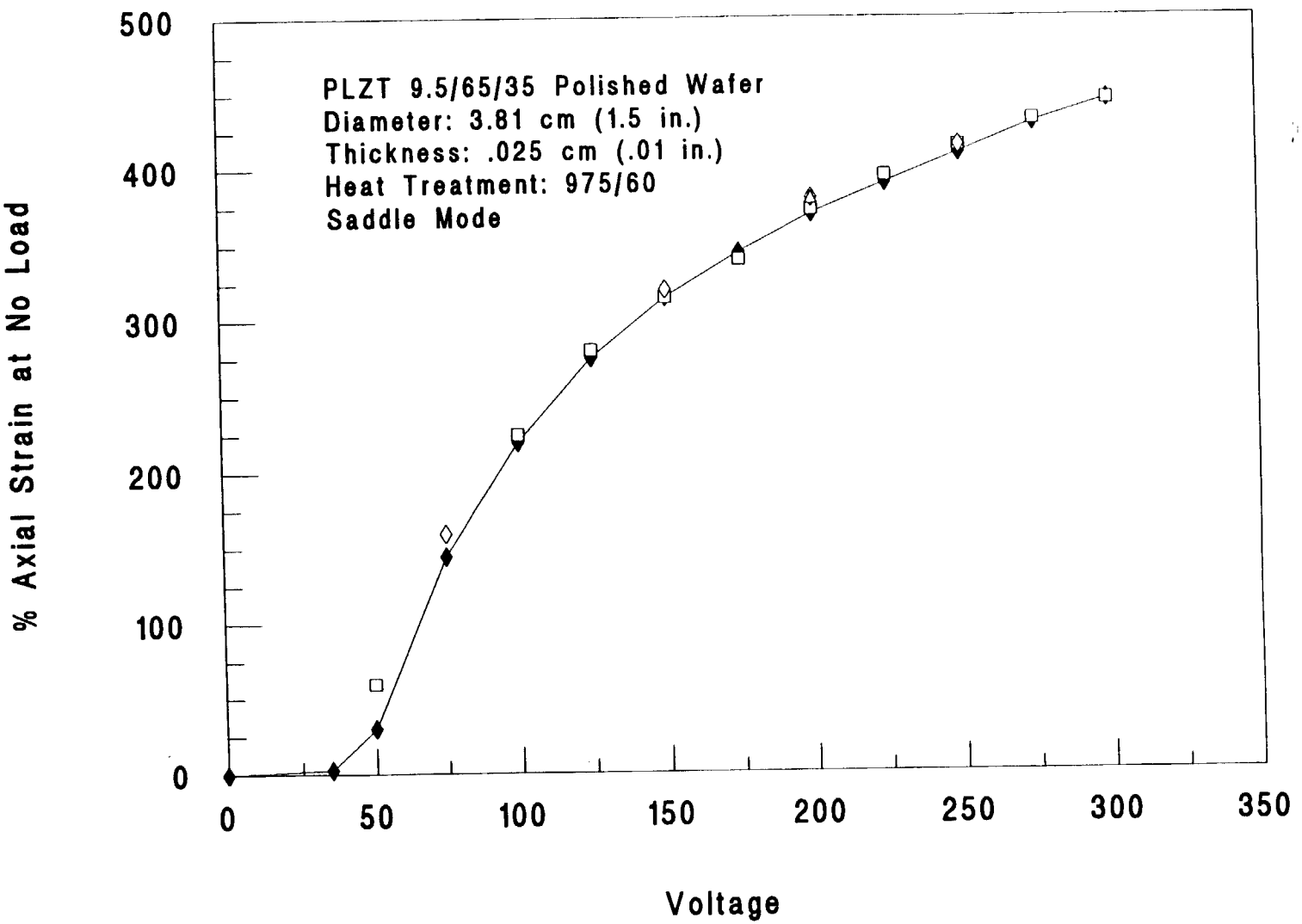

Figure 29. Voltage Dependent % Axial Strain Hysteresis Characteristics of PLZT 9.5/65/35 Polished Rainbow Wafers (open symbols are randomly selected voltages)

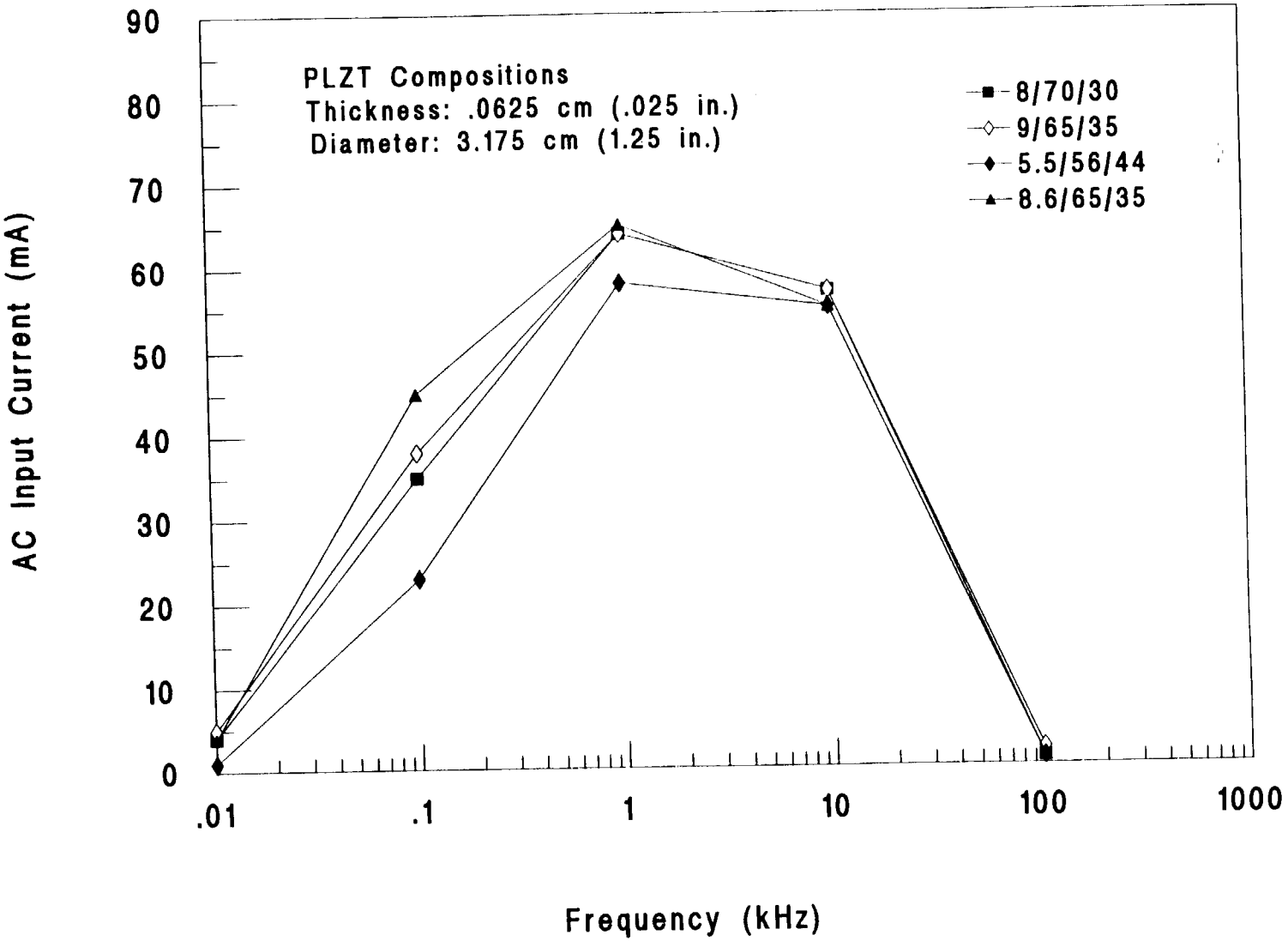

Figure 30. Effect of Operating Frequency on AC Input Current

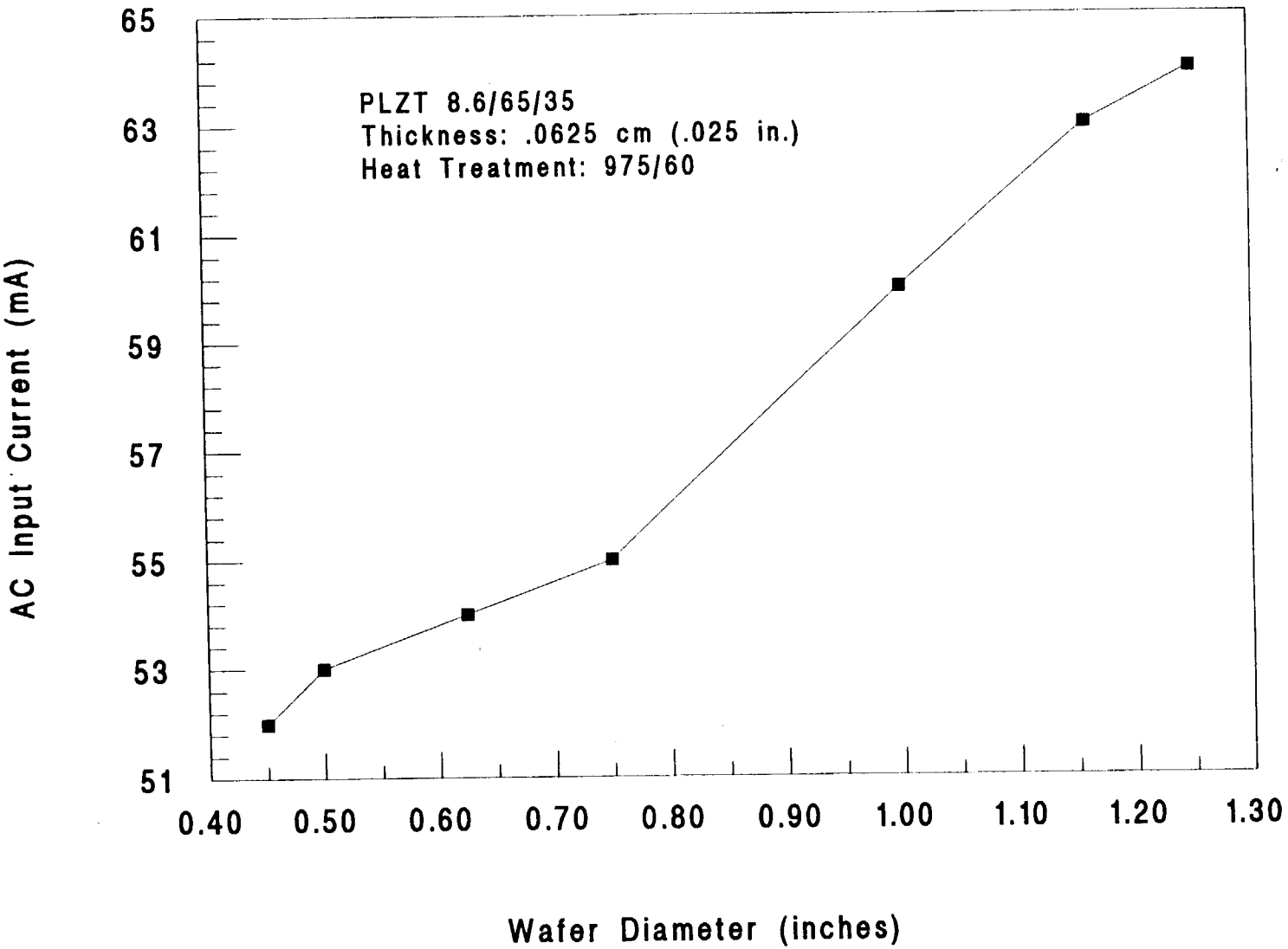

Figure 31. Effect of Wafer Diameter on AC Input Current